Study and applications of hybrid organic/ inorganic semiconductor quantum dots in thin films

Hung-Ju Lin

National Central University, Taiwan
Department of Optics and Photonics
College of Science

Study and applications of hybrid organic/ inorganic semiconductor quantum dots in thin films

Hung-Ju LIN

Dissertation submitted for the Doctor of Philosophy degrees

at the National Central University, Taiwan
in *Science*
and
at the Aix-Marseille University, France
in *Physics and Materials Science*

Defended on: December the 12th, 2013

Dissertation committee:

M. Cheng- Chung Lee	Professor, National Central University	Advisor
M. François Flory	Professor, Aix-Marseille University	Advisor
M. Sheng- Hui Chen	Professor, National Central University	Co-advisor
M. Judikaël Le Rouzo	Assistant Professor, Aix-Marseille University	Co-advisor
M. Shiuh Chao	Professor, National Tsing Hua University	Reviewer
M. Yi-Jun Jen	Professor, National Taipei University of Technology	Reviewer

Aix-Marseille University, France
Equipe Optoélectronique et Photovoltaïque, Institut Matériaux Microélectronique Nanosciences de Provence
ED352 — Ph.D. School in Physics and Materials Science

Abstract

Semiconductor quantum dots have attracted a lot of attention for their potential application in many fields such as optoelectronics and biology.

In this study, we investigated the optical properties of hybrid nanocomposited thin films made of PMMA polymer containing different concentrations of core-shell CdSe/ZnS quantum dots. Both the absorption and luminescence spectra can be well explained by taking into account quantum mechanisms. From the luminescence spectral evidence of the coupling effect between quantum dots has been observed. With a pump laser emitting at 514 nm the luminescence spectrum centered at 560 nm strongly changes with time.

In addition, it is necessary to control the luminescent light spatial distribution where the application is concerned. Therefore we proposed structural films with a bi-periodic grating by nanoimprint technique using an engraved silicon mold. The characterizations of the imprinted structure show good quality. We also showed, by a numerical calculation, that the local field is resonant in the periodic structure and that the emission diagram can be controlled in the far field.

Résumé

Semiconductor nanocrystals or quantum dots Les nanocristaux de semi-conducteurs, ou boites quantiques, trouvent leur application dans de nombreux domaines. Pendant cette thèse nous avons étudié les propriétés optiques de couches minces nanocomposites de polymère PMMA contenant différentes concentrations de boites quantiques CdSe/ZnS. Les spectres d'absorption et de luminescence peuvent être expliqués par la mécanique quantique. A partir des spectres de luminescence mesurés nous montrons clairement l'effet du couplage entre les boites quantiques. Sous l'effet d'un faisceau pompe à 514nm le spectre de luminescence centré à 560nm évolue fortement au cours du temps. Nous montrons que ces couches luminescentes qui convertissent ainsi les fréquences optiques peuvent permettre d'augmenter l'efficacité de cellules solaires. Par ailleurs, pour bénéficier au mieux du fort rendement de photoluminescence, il est nécessaire de contrôler la répartition spatiale de la lumière émise. Pour contrôler cette répartition une nanostructure bi périodique a été réalisée dans des couches de PMMA contenant les boites quantiques par nano-impression, en utilisant un moule en silicium gravé. La caractérisation de la structure réalisée met en évidence la qualité de la méthode utilisée. On montre également, par la théorie, à la fois que le champ local est résonant dans la structure et que la lumière se répartie en champ lointain dans les directions de diffraction contrôlées par la période du réseau.

Acknowledgement

Foremost, I would like to express my sincere appreciation to my advisor Prof. Cheng-Chung Lee and Prof. François Flory, for their patience, enthusiasm, vast knowledge and their great support throughout my PhD study. I also thank my co-advisor Prof. Sheng-Hui Chen and Assistant Prof. Judikaël Le Rouzo for their valuable advices and kind assistances during the research.

Concerning the dissertation committee, I wish to specially thank the reviewers, Prof. Shiuh Chao and Prof. Yi-Jun Jen, for their detailed review and constructive comments on this work.

Besides, I would like to thank the French Institute in Taipei and the Office of International Affairs in National Central University for offering the financial support in the period of doing research in France.

During this period of two years in France, I wish to thank again to the Prof. François Flory and Assistant Prof. Judikaël Le Rouzo very much. They always guided me to deal with some complex works and gave warm consideration for me. Also I wish to thank all my lab colleagues, for accompanying with me to create lots of our own impressive and precious memories.

On the other hand, I thank all of my friends for making my life so colorful. In addition, I sincerely thank everyone who ever gave me a favor during my study.

Finally and most importantly, I am truly grateful to my family for supporting me to the France and giving me the unstinting source of love. Their love and encouragement are always my motive force to go forward.

Contents

List of figures

List of tables

Chapter 1: Introduction

In recent years, nano-objects have attracted many studies. A nanostructured material can be defined as a system with patterns in the range of 1-100 nm. In fact, different scales of natural materials surrounding us, from atoms and molecules to crystals and bulk components, have their own intrinsic nanostructure. Thanks to tremendous progress in nanotechnologies, optical materials can also be artificially structured at different nanometer-scales [1].

Up till now, nanotechnology has primarily been concerned with the physical, chemical, biological and engineering fields including the realization of artificial structures at the nanometer scale level. Among the multitude of nanomaterials created, nanocrystals (NCs) are one of the key elements whose design and function can be modified, tailoring their fundamentally chemical and physical properties. A particular class of NCs which is quite popular and today represents the most fascinating and potentially revolutionary inorganic semiconductor material, is the family of colloidal quantum dots [2]. In QDs electrons, holes and excitons can be in strong quantum confinement when the dimensions of the material are smaller than the Bohr radius [3]. If excitons are strongly confined, then remarkable and novel optical and electrical properties are obtained.

Quantum dots are also referred to as “nanocrystals” and the colloidal definitions reveal their chemical origin. In fact, chemical synthesis currently represents the most effective way to obtain high quality (in terms of size control, narrow size distribution, good crystalline structure and high optical performances) nano-objects on the gram scale [2]. Thus, they can be handled as ordinary chemical substances and implemented in many fields such as in

opto-electronic devices (lasers, light emitting diodes or solar cells) [4, 5], as well as in biological applications (in vivo imaging or labeled molecular) [6-9].

This dissertation focuses mainly on the characterization of quantum dots and their applications in nanocomposite thin films. This research is based on the cooperation between the Department of Optics and Photonics, National Central University in Taiwan and the OPTO-PV team, Institut Matériaux Microélectronique Nanosciences de Provence (IM2NP), Aix Marseille University in France. The whole work is organized into three principal subjects. The first subject discussed the novel optical behavior of nanocomposited PMMA thin films containing semiconductor quantum dots. The second subject is focused on the control of light propagation by imprinting periodic structures in these hybrid polymer/ QDs thin films. The third subject considers the effects of these ideas and techniques applied to solar cells.

In the chapter on hybrid organic thin films/ quantum dots, we present the characteristics of quantum dots embedded into PMMA thin films. The experiment was performed by means of the proper composition of solutions and the spin coating technique in order to deposit thin films. From their optical properties, strong excitonic features caused by quantum confinement were observed. Particularly in the photoluminescence analysis, a manifestly strong peak with narrow width is obtained and evidence of the coupling effect between quantum dots is also discovered. Moreover, we demonstrate the QDs properties of the down-conversion frequency which can be directly applied to solar cells. Through the external quantum efficiency analysis we show that photons converted from UV to visible light by the QDs are absorbed by solar cells.

Once a strong photoluminescence is obtained, it becomes more attractive and more applicable if the QDs luminescence light can be further controlled in its

spatial distribution. For this purpose, we present our structuring method based on imprint techniques. Thanks to the transition temperature of PMMA, thermally assisted nanoimprints can be applied to transfer the structure from a silicon mold to the hybrid PMMA/QDs layers. After theoretical and experimental analysis, the periodic structure is well defined showing significant 2D-grating properties. By means of electric field simulation, a controllable QDs luminescence into the spatial distribution is demonstrated.

Chapter 2: Nanomaterial evolution and nanoimprint technique

2.1 Development of nanostructured materials

For nanostructured materials, especially nanocrystals, we now provide a brief overview of the main studies regarding them carried out until now. Thus the section is organized from nanostructures existing in nature, artificial nanostructured materials and the new generation. The main focus in our study is on nanocrystal materials, because of early developments which have lead to a lot of useful applications. Furthermore the new generation nanocrystals of a core-shell type are also considered and compared with single core nanocrystals.

When changing over from bulk to nanocrystal semiconductors both the electronic and optical properties are affected. In Figure 2.1.1, the density of states is varied from a bulk to a 0D (dot) semiconductor with a change from continuous to discrete energy states induced by confinement effects [3]. The 1D and 0D structures are analogous to quantum wires and quantum dots [2, 3].

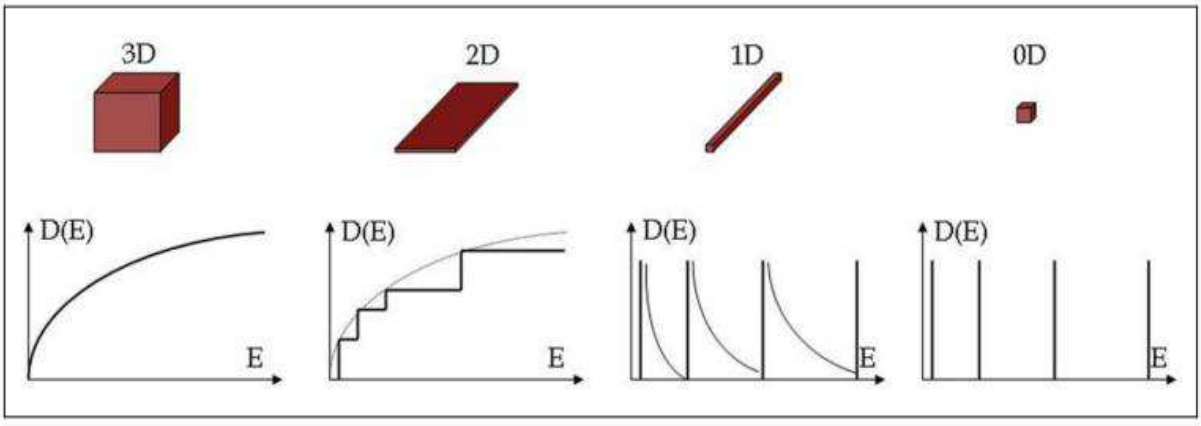

Figure 2.1.1: The "Density of States" (DOS) function evolves from a bulk (3D solid) to a 2D, 1D and 0D system with varying degrees of confinement. [2, 3]

2.1.1 Nanostructures in nature:

Nanotechnology has been quickly developing during these last few decades. However, we are already actually surrounded by many amazing nano-materials in nature. The most typical one is the “lotus” noted for its water-repellent and self-cleaning surfaces. Figures 2.1.2 (a) and (b) who a lotus leaf surface covered by micrometer-sized papillae decorated with nanometer branch-like protrusions [10]. The roughness of papillae reduces the area of contact between the surface and a liquid drop. This ideal structure has inspired scientists to “imitate” it for fabricating artificial self-cleaning surfaces as in Figure 2.1.2 (d) and (e) [10].

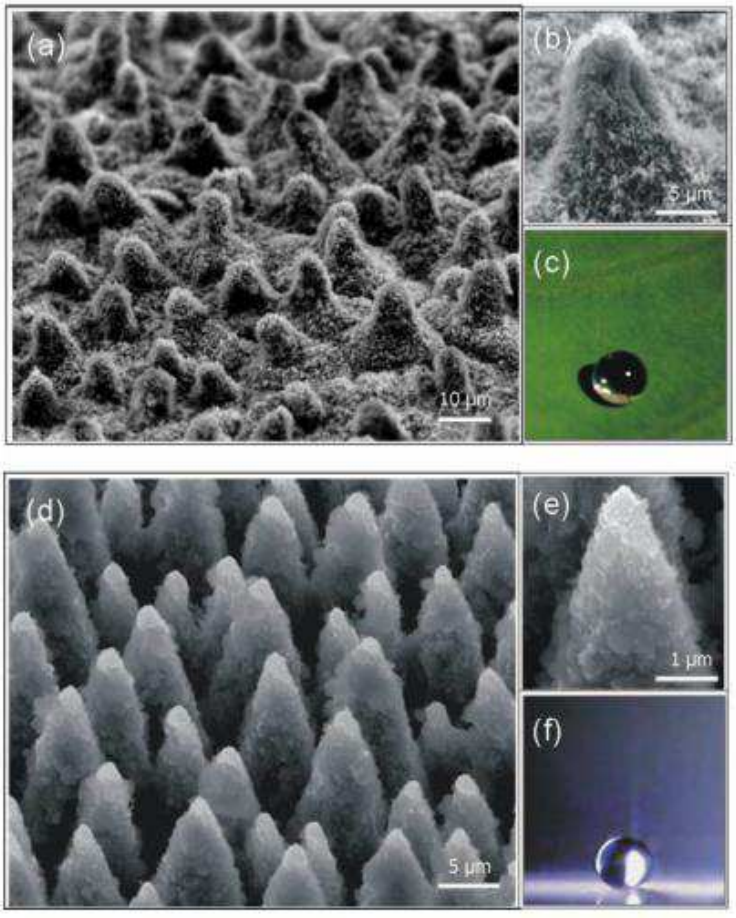

Figure 2.1.2: (a) SEM image of the surface of a lotus leaf and (b) a higher magnification with hierarchical structures clearly resolved. (c) A water drop on the surface of the lotus leaf attains a nearly spherical shape. (d) SEM image of the artificial laser- structured silanized silicon surface and (e) a higher magnification showing the dual length-scale roughness. (f) A water drop on the structured surface. [10]

It is however not only plants like the lotus, but also many insects and animals have their own nanostructure, for example beetles, sea mouse and butterflies [11]. Due to genetic evolution, their structures which are built up in the nano-sized range are naturally created by their molecular precursors. Another example is our own body, comprised of a systematic composition of many nanostructured materials such as the structure of DNA, a nanostructure existing within the nucleus of a cell which stores information on evolution.

As shown in Figure 2.1.3 (a) and (b), the natural structure of butterfly wings is quite interesting. Most of the butterflies of the Papilio species present a common bulk and surface structure. The upper membrane is constituted of a multilayered air/chitin film [12]. An important property of the super hydrophobic surface of butterfly wings is found with a contact angle of about 160° [12] which is close to that of the lotus. In addition, the natural structure of butterfly wings can be replicated as can be seen in Figure 2.1.3 (c) and (d).

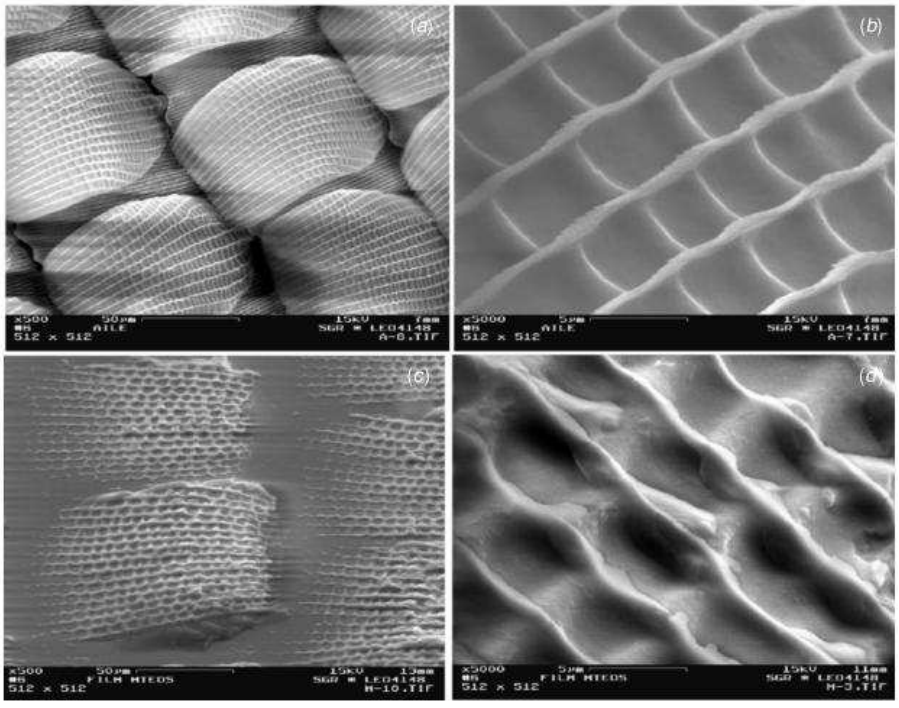

Figure 2.1.3: SEM images of the butterfly wing (a) and (b), the replicated surface (c) and (d). Angle of view: 45°.The scale bar corresponds to 50 µm on (a),(c) and to 5 µm on (b),(d). [12]

2.1.2 Artificially nanostructured materials: semiconductor quantum dots

At the beginning of the 80s, a novel size effect induced by nanocrystals of very small size was discovered by A.L. Ekimov *et al.* [13]. In this paper, the exciton absorption spectrum of CuCl crystals grown in a dielectric matrix has been studied. The crystal size could be controlled from several tens of angstroms to hundreds of angstroms. With size variations, an absorption shift (of up to 0.1 eV) could be attributed to a quantum size effect [13]. In 1988, M.A. Reed et al. investigated the electronic transport through a three-dimensionally confined semiconductor quantum structure [14]. They showed that the fine structure observed in resonant tunneling through the dot corresponds to a discrete density of states of a zero-dimensional system. This zero-dimensional system was also named for the first time as "quantum dots" [14].

General synthesis and processing of monodispersed nanocrystals [15]**:**

In the general synthesis of monodispersed nanocrystals, classic studies by La Mer *et al.* have shown that the production of monodisperse colloids requires a temporally discrete nucleation event followed by slower controlled growth on the existing nuclei as shown in Figure 2.1.4 [16]. It is necessary to raise the precursor concentration above the nucleation threshold via rapid addition of reagents to the reaction vessel. The result of a short nucleation burst can partially relieve the super-saturation. If the consumption of feedstock by the growing colloidal NCs is not exceeded by the rate of precursor addition to the solution, no new nuclei is formed. Because the growth of any type of NC is similar to all others, the initial size distribution is mainly determined by the time over which the nuclei are formed and begin to grow. Monodispersed NCs with diameters with standard deviations of $\sigma \leq 5\%$ can be made in this way.

Figure 2.1.5 shows high resolution TEM observations of the size and shape of CdSe NCs. This image indicates a nearly spherical shape with a size of around 3.9 nm that was clearly produced. [15, 17].

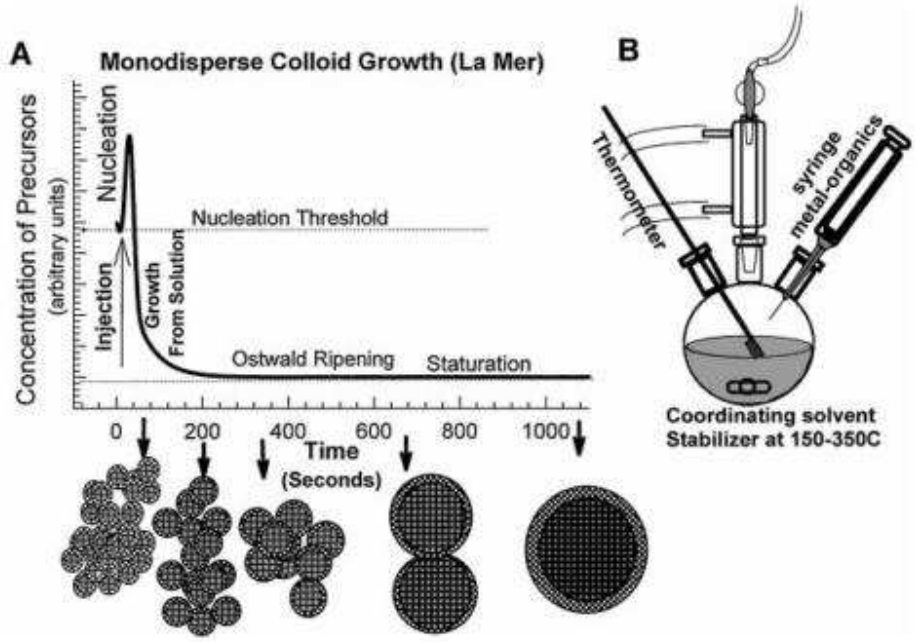

Figure 2.1.4: (A) Depiction of the stages of nucleation and growth for the preparation of monodispersed NCs in the framework of the La Mer model. As NCs grow with time, a size series of NCs may be isolated by periodically removing aliquots from the reaction vessel. (B) Representation of the simple synthetic apparatus employed in the preparation of monodisperse NC samples. [15, 16]

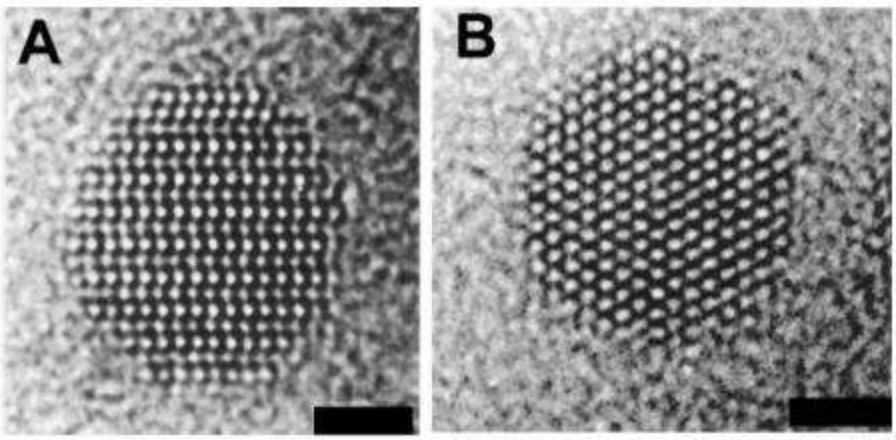

Figure 2.1.5: Collection of high resolution TEM images for typical NC materials such as (A) <100>-oriented CdSe (scale bar =15 Å), (B) <001>-oriented CdSe (scale bar =15 Å). [15, 17]

General energy bandgap blue shift with size:

Many types of semiconductor NCs (or QDs) have been developed during the few decades including CdSe, CdS, CdTe and PbS compounds [18, 19]. Their energy bandgaps are very different, making possibly numerous applications.

One of the most attractive characteristics of these semiconductor QDs is the size-dependent band gap which was caused by quantum confinement effect [3] which can be theoretically understood by solving the Schrödinger equation, for example, a simple case of electrons in 1-dimension [20]. Via this confinement effect, the essential bulk energy bandgap can be significantly shifted to a higher photon energy (blue-shift phenomenon) with its decreasing size [21]. As shown in Figure 2.1.6, both CdSe and PbS nanocrystals revealed a blue-shifted absorption spectra with reduced size. The same shift is also obtained on the luminescent spectrum, as shown in Figure 2.1.7.

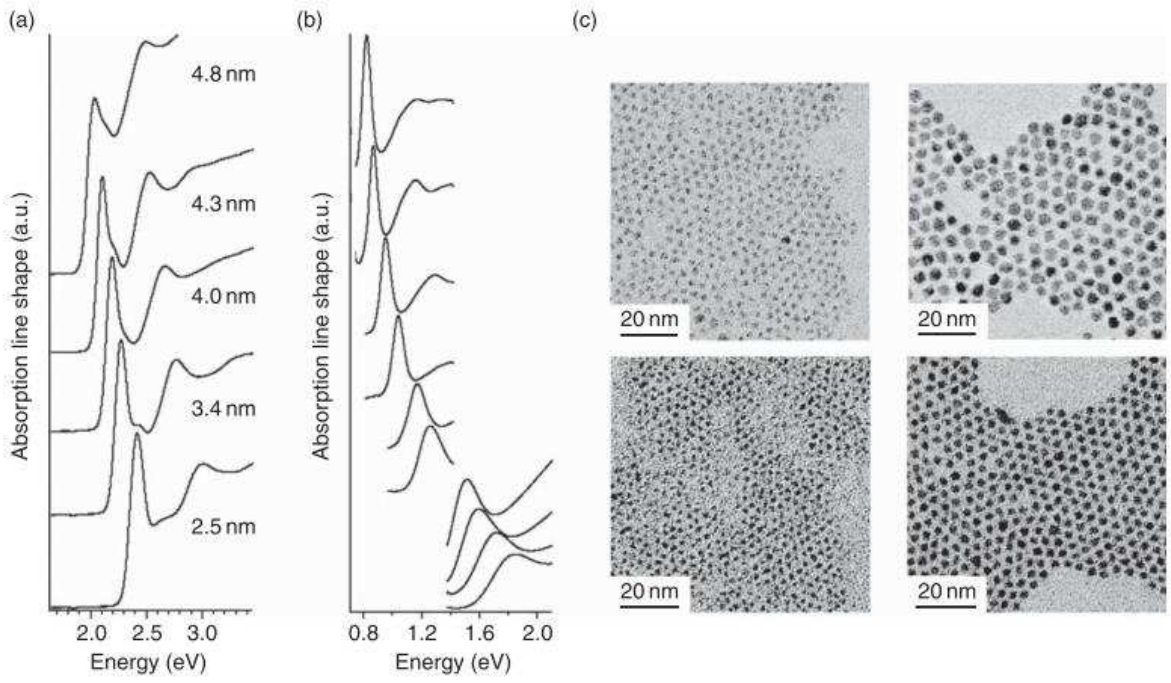

Figure 2.1.6: (a) Size tuning of CdSe nanocrystal absorption spectra spanning the visible spectral region. (b) Size tuning of PbS nanocrystal absorption spectra spanning the near-infrared (NIR) spectral region. (c) Transmission electron microscope (TEM) images of different PbS nanocrystal samples with average sizes ranging from 2.3 to 5.5 nm. [18, 19]

A red-shift can be observed between the absorption and emission of QDs. Some possible explanations are illustrated in Figure 2.1.8 [22]. This figure reveals different possibilities linked to the electronic energy transition due to the splitting of the discrete energy levels caused by quantum confinement in the semiconductor nanoparticles [3].

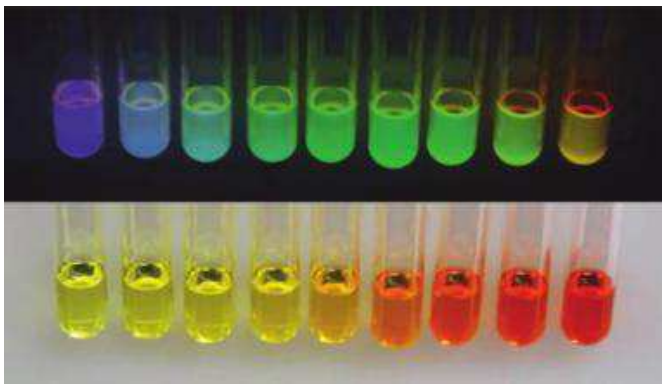

Figure 2.1.7: Colloidal suspensions of CdSe quantum dots of increasing size from left (approximately 1.8 nm diameter) to right (approximately 4.0 nm in diameter). Bottom: Samples viewed in ambient light vary in color from green–yellow to orange–red. Top: The same samples viewed under long-wave ultraviolet illumination vary in color from blue to yellow. [22]

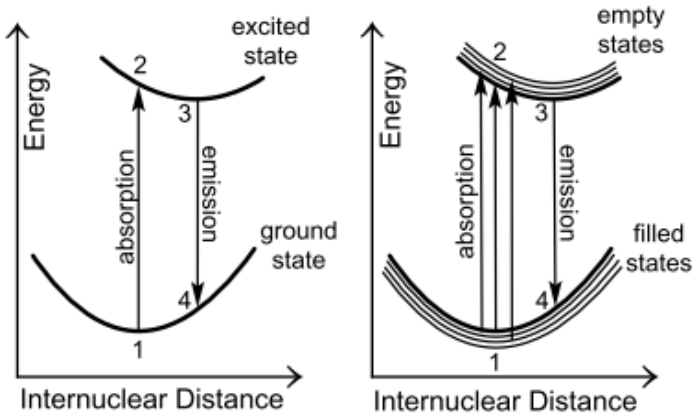

Figure 2.1.8: Relationship between absorption and emission energies for discrete molecules (left) and for semiconductor nanoparticles (right). When a photon is absorbed thereby exciting an electron from the ground state (1) to an excited state (2) the bond order decreases and the atoms relax to a longer internuclear distance (3) before the emission of a photon (4) and relaxation to the ground state (1). In semiconductor nanoparticles the process is the same (steps 1–4) but there are more possibilities for the energy of the electron under excitation from a photon to match an electronic energy transition. [22]

2.1.3 New generation of semiconductor quantum dots:

One of the primary aims in modern materials is the design of new nanomaterials that exhibit novel properties to be utilized in various applications. With similar aims, colloidal techniques have the potential for developing elegant extensions of the synthetic NCs. These novel NCs involve the fabrication of hybrid NCs in which domains made from different materials can be assembled together in a single nano-object. These nanostructures would merge the properties of the individual materials, with new properties being likely to arise from their combination. In the synthesis of NCs made of more than one material, the formation of a large interface between the two materials is also frequently observed when the lattice constants of the two components do not differ significantly from each other [23].

Semiconductor core and core-shell quantum dots:

Generally the semiconductor quantum dots exhibit high luminescence emissions. This high efficiency of light emission is largely due to the strong overlap between the electron and hole wave functions in the confined quantum structure, whereas the exciton in bulk semiconductors is not confined in space and can rapidly dissociate, increasing the probability of nonradiative relaxation events associated with crystalline defects and charge carrier traps on the crystal surfaces [24]. However, there still exists a major source of nonradiative decay from the surface trap states, represented by unsaturated bonds on the surface [25]. Thus, it is important to have another type, namely core–shell nanocrystals, for passivating and further enhancing the luminescence from the core particles. Normally the CdSe core with a low bandgap can be covered by a wider bandgap material of ZnS as can be seen in Figure 2.1.9.

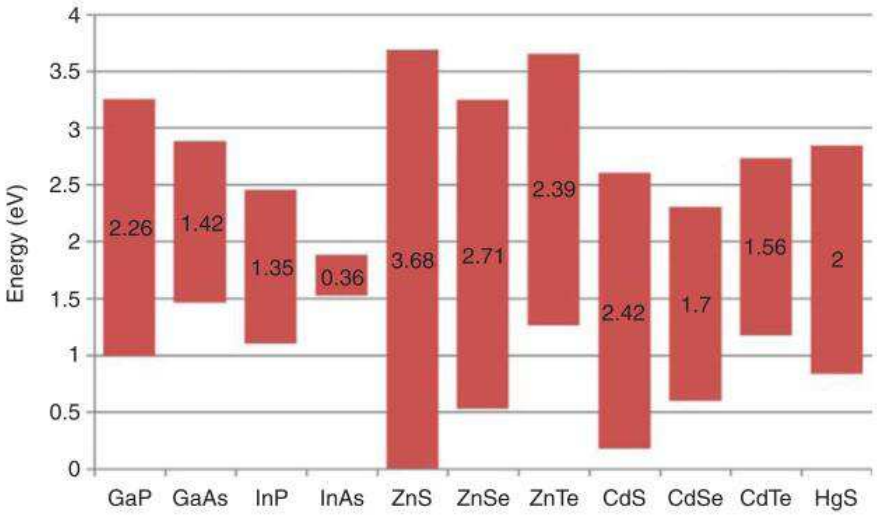

Figure 2.1.9: The band gaps and their relative alignment for selected semiconductor materials with the band offsets. The numbers in the bars indicate the width of the bulk band gap in electron volt. [26]

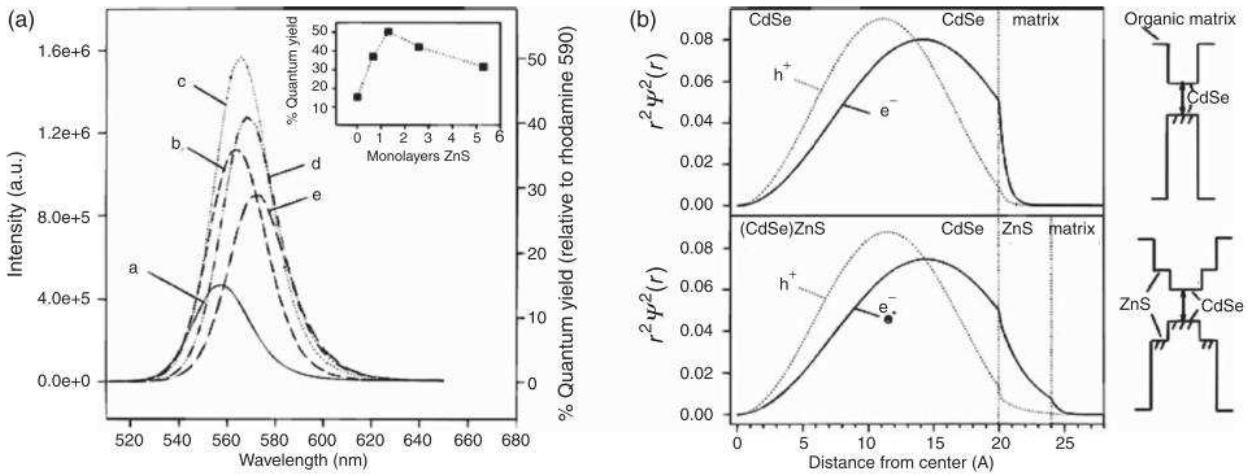

Figure 2.1.10: (a) Fluorescence spectra of one type of CdSe nanocrystals overcoated with shells of ZnS of different thicknesses. The CdSe cores have a diameter of 4.2 ± 10% nm and the shells have a thickness of (a) 0, (b) 0.65, (c) 1.3, (d) 2.6, and (e) 5.3 monolayers of ZnS. In addition to the variations of the quantum yield (see inset), one can also observe a red shift and a broadening of the spectra with an increasing shell thickness. (b) Radial probability density of the electron and the hole for the lowest energy states for CdSe cores and CdSe/ZnS core–shells. Due to the lower step in the potential at the surface of the CdSe section in the case core–shell nanocrystals, the probability density in the ZnS section is increased when compared to the respective volume in the case of the bare CdSe cores. This leads to an efficient increase of the confinement volume and thus to a slight red shift of the optical properties. [27, 28]

In Figure 2.1.10, the area under the wave function of both the electron and the hole in the matrix surrounding the nanocrystal is decreased in the case of the core–shell nanocrystals, and thus the probability of finding excitons in this area is also diminished. Therefore, the probability of an interaction between the excitons and the host matrix is reduced as well [28].

Type I and type II semiconductor core-shell quantum dots:

The core-shell Type 1 QDs are described. The band edges of the core material are localized in the band gap of the shell material. CdSe/ZnS is a typical case for Type I. Moreover, in 2003, Bawendi and co-workers proposed a new type of core-shell semiconductor heterostructure for which the conduction and valence bands of the core and shell material are staggered, resulting in the segregation of electrons and holes between the core and shell materials [29].

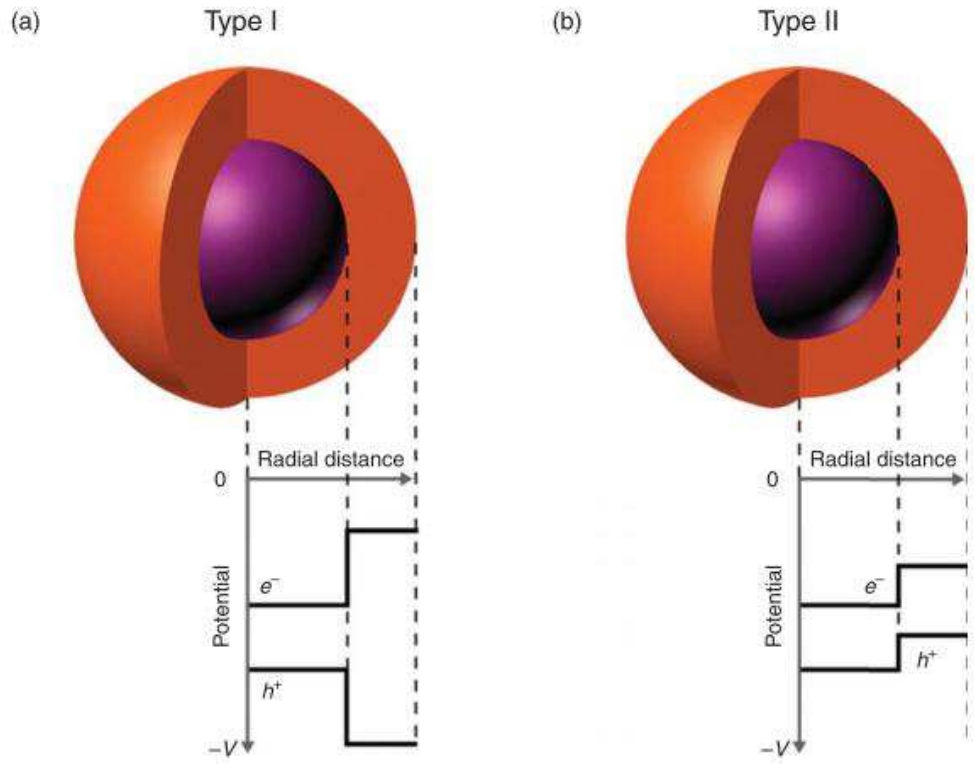

Figure 2.1.11: Alignment of the conduction and valence band edges for two types of hetero-structures. (a) Type I has a straddling configuration, whereas type II (b) is staggered. [30]

The goal in the formation of type II heterostructures is to generate a considerable red shift in the optical properties [28]. As can be seen in Figure 2.1.11, the type II heterostructures can induce electrons to be mostly confined in the core material and cause holes to be mostly confined to the shell material, for example, CdSe/ZnTe core-shell QDs [29]. Thus the localized electrons/holes in different sections can obtain a longer exciton lifetime via reduced overlaps [28].

Semiconductor nanorods and other unique shapes:

Other unique structures were studied by Milliron DJ, Hughes SM, et al. Figure 2.1.12 shows inorganically coupled colloidal QDs and rods which can be connected epitaxially at branched and linear junctions within single NCs [31].

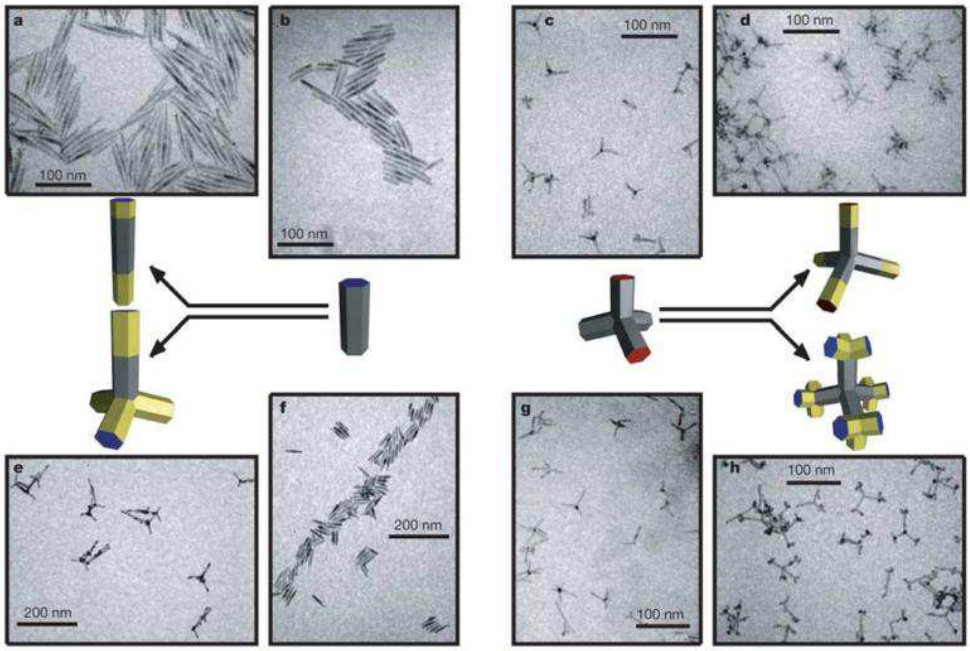

Figure 2.1.12: Nanocrystal heterostructures. Extended rods (a) were formed by first growing CdS nanorods (b), and then adding CdSe extensions to each end. Branched rods (e) result from nucleation of CdTe on either end of CdSe nanorods (f). A CdTe zinc-blende region at one end creates the branch point. CdSe tetrapods (c, g) comprise a zinc-blende core and four wurtzite arms. Extending each arm linearly with CdTe yields extended tetrapods (d). Branched tetrapods (h) result from nucleation of CdTe zinc-blende branch points on the end of each arm. The model sequences illustrate the growth processes. In each case, the first generation is shown in gray and the second in yellow, while red and blue parts indicate the unique crystal faces of the wurtzite structure. [31]

2.2 Development of nanocomposite thin films

Regarding the nanocomposite thin films, they can be treated as films composed of different distinct phases where a characteristic length scale is in the order of a few nanometers. Generally two distinct phases are mostly defined in nanocomposite thin films. Due to the unique nanostructures, these artificial new materials are expected to display optical properties totally different from bulk composites ones. Several types of nanocomposite thin films have been considered in many applications such as multilayered thin films and granular nanocrystal thin films. Conventionally the optical properties of the former type of film gained considerable attention and there are only a few studies on the latter type [32]. For the former type, the multilayers are composed of two or more different materials with different refractive indices. Many types of spectrum filters can be obtained such as high/low pass filters and narrow-band pass filters, anti-reflection (AR) coating, and thermal mirrors for improving the optical system and optoelectronic device. For example, there are already many applications which use AR coating in displays and solar cells.

With more and more developments and improvements in nanotechnology, the granular nanocrystal thin films can achieve more and more sophisticated compositions, for example, dielectric/granular metal, dielectric/embedded semiconductor crystals, polymer/ embedded semiconductor crystals, and so on. Different composite thin films belong to their own function. Take granular metal films as an example. They are composed of a thin film ceramic matrix embedded with metal granules of diameters as small as a few nanometers, and exhibit novel behavior in terms of their hardness and apparent elastic behavior [32].

2.2.1 Dielectric material contains nanocrystals:

In many types of nanocrystals/dielectric nanocomposite layers, the silica-based nanocomposites are considered one of the potential systems for quantum confinement in semiconductive nanocrystallites in order to have better control of their shape and properties [33]. These embedded compositions can be considered as metal or semiconductor nanocrystals.

Metal nanocrystals/dielectric nanocomposites: their optical properties have attracted numerous studies because of the unique electronic properties and surface-enhanced spectroscopic applications compared to the bulk material [34, 35]. Many studies have been reported the effect of reducing metal particle size on the optical process in these films. When such a metal–dielectric nanocomposite is excited by light, photons are coupled to the metal–dielectric interface, causing an induced charged density oscillation and showing a strong absorption maximum, called the surface plasmon resonance [36]. The resonance frequency is influenced by several factors, e.g., the size and shape of the nanoparticles and also their surrounding environment [37]. In [36], silver particles embedded in the silica nanocomposite thin films were prepared by high pressure DC sputtering technique. These increase in substrate temperature easily causing a variation in the size and shape of the nanoparticles. Films containing a distribution of particle sizes and shapes lead to an inhomogeneously broadened and asymmetrical surface plasmon resonance in the optical absorption spectra. They found that the size and shape distribution of metal nanoparticles has a profound effect on the optical absorbance spectra.

Semiconductor nanocrystals/dielectric nanocomposites: the wide bandgap material ZnO has attracted much research attention due to its desirable physical properties. ZnO has a large exciton binding energy (around 60 meV) at room

temperature [38] which can provide efficient excitonic emission at room temperature. Because ZnO emits a broad luminescence emission in the green–yellow region, this property renders it as a potential material for blue- or white-light emitting devices [39]. There are many methods for making an emitting ZnO/SiO_2 nanocomposite thin film, such as the sol–gel [38], molecular capping [40] and also the sputtering method which can be employed [39]. Figure 2.1.1 clearly shows crystallized ZnO NCs embedded in a silica matrix [33].

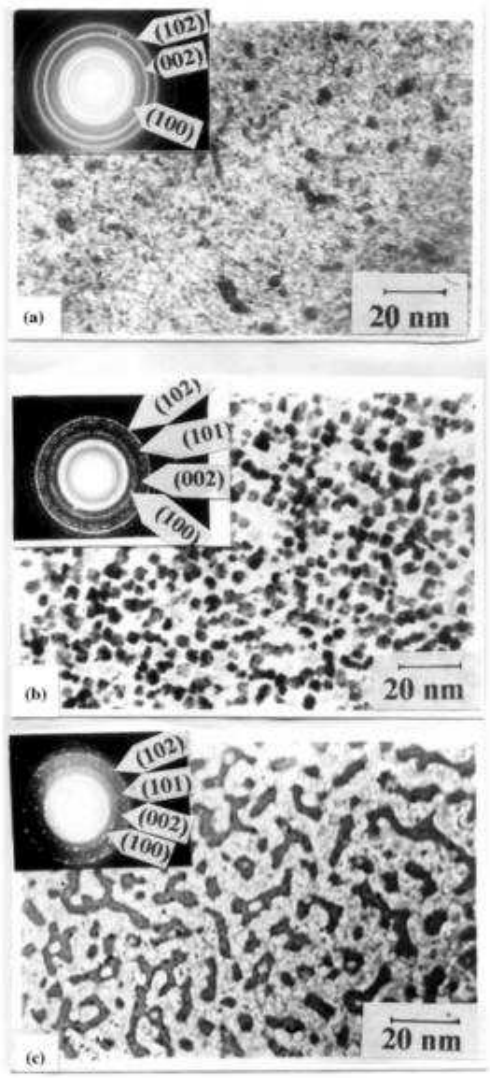

Figure 2.2.1: TEM micrographs and electron diffraction patterns of three representative ZnO/SiO_2 nanocomposite films annealed in air for 10 min at (a) 573, (b) 673 and (c) 773 K. [33]

2.2.2 Organic polymer containing inorganic nanocrystals:

Organic polymer/inorganic hybrid materials are promising candidates that have attracted considerable attention due to their variable physical and chemical properties for materials including nanoparticles [41]. Incorporating inorganic nanoparticles into a polymer matrix is most straightforward and common method for fabricating such hybrid materials. There have been several publications on hybrid materials with their enhanced electrical, mechanical and optical properties.

To obtain tunable electrical properties with nanocomposite material, it can be achieved through hybrid polymer/metal particles. In [41], silver is incorporated into polytetrafluoroethylene (PTFE). They found that near the percolation threshold an expected sharp change in the resistivity from 10^{7} Ω (polymer-like material) to 10^{-3} Ω for a metal-like material, when increasing the silver content in the polymer. In this case, a significant change in resistivity of several orders of magnitude occurs with just a small percentage point change in the metal amount, as clearly shown in Figure 2.2.2.

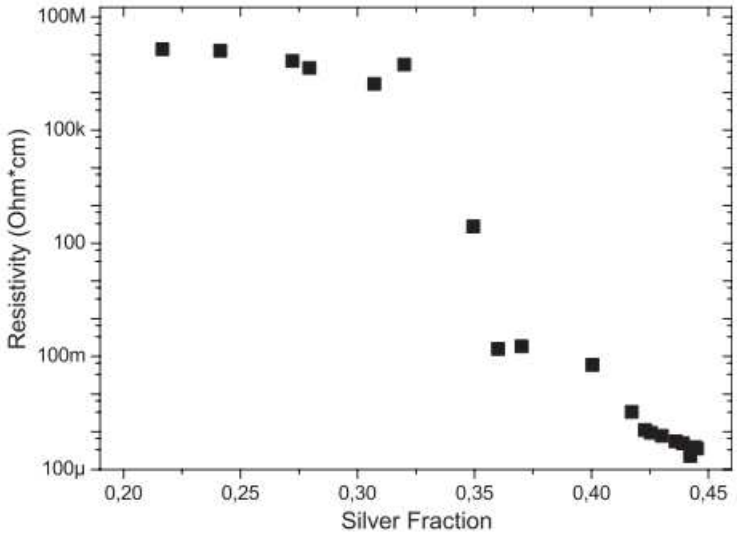

Figure 2.2.2: Change of the electrical resistivity with an increase in filling factor for Ag/PTFE nanocomposite films. [41]

To obtain tunable optical properties with nanocomposite material, inorganic nanoparticles can be embedded in a polymer matrix to form a high refractive index nanocomposite [42]. For example, incorporating PbS nanoparticles into gelatin or poly(ethylene oxide) has been reported [43, 44]. High refractive index nanocomposites have also attracted considerable interest in light emitting diodes (LEDs) encapsulation [45]. The light extraction efficiency will be greatly enhanced due to internal reflection phenomena occurring at the interface between the light emitting semiconductor layer and the resin [42]. On the other hand, titanium oxide (TiO_2, titania) is well-known as an inorganic material having a high refractive index, ~2.45 (anatase) and ~2.70 (rutile) [46]. Thus it can be another potentially promising incorporated material for the polymer matrix to achieve hybrid layers with a high refractive index.

To obtain tunable optical properties in the nanocomposite material such as absorption spectrum and luminescent emission wavelength, the change of nanoparticle size is a direct solution because of the quantum confinement effect. Typical absorption and luminescence spectra of samples with different ZnO QD sizes separately estimated to be 12, 7.4, 6.5, 5.3, 4.2 and 3.5 nm are shown in Figure 2.2.3 [47]. The UV emissions represent the relaxed state of the excitons near the band edge in ZnO QDs [47]. In general, quantum confinement shifts the energy levels by generating a blue shift in the transition energy while decreasing the particle size. Thus with the nanocomposite material, we can not only control the level of spectral blue shifts by tuning the particle size, but we can also modify the spectral intensity from the particle doping ratio. Figure 2.2.4 [4], ZnO-QDs embedded in a transparent epoxy used for the encapsulation of UV light-based white light emitting dioxides (UV-WLED) lamps shows an example of nanocomposite applications.

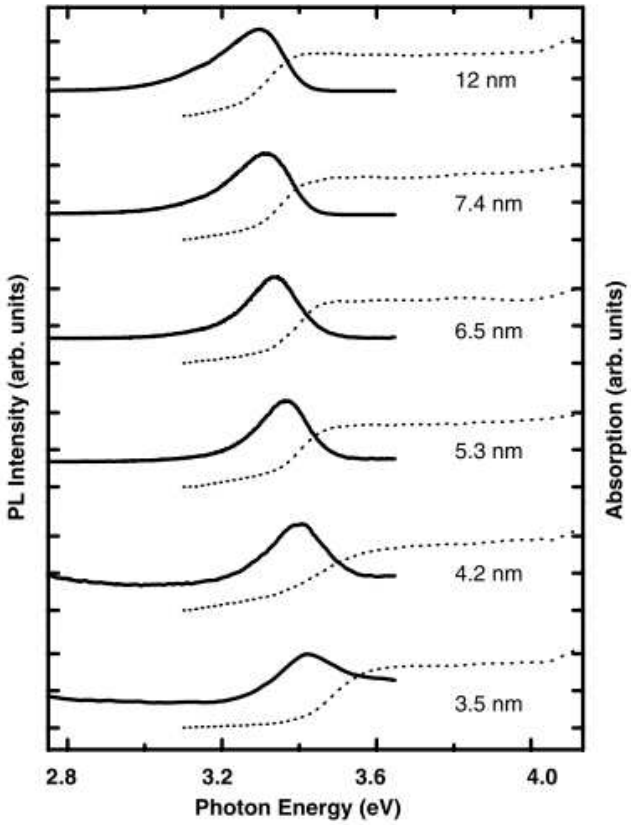

Figure 2.2.3: PL (solid line) and absorption (dashed line) spectra near the band edge of various sized ZnO QDs. [47]

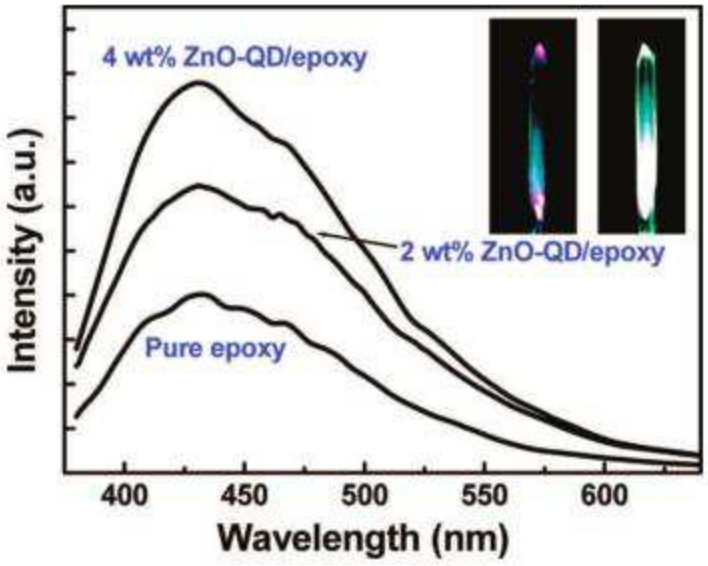

Figure 2.2.4: Fluorescence emission spectra of pure epoxy and ZnO QDs/epoxy nanocomposites excited at 370 nm. The inset shows the photographs of the UV-WLED lamps (370 nm) encapsulated with the pure transparent epoxy (left) and the ZnO QDs/epoxy nanocomposite (right) containing the 4 wt % ZnO QDs content. [4]

2.3 Historic development of nanoimprint lithography

Nanoimprint lithography (NIL) is a novel method to fabricate micron to nanometer scale patterns with high-throughput and low-cost [48]. Originally the NIL technique was developed due to the high cost and limited resolution of optical lithography [49]. Scanning electron beam lithography can reach 10 nm resolutions. However, mass production of sub-50 nm structures seems economically impractical due to inherent low throughput in a serial processing tool [50, 51]. X-ray lithography can have a high throughput with demonstrated 50 nm resolutions, but the cost of X-ray lithography is much higher [52]. For the above reasons, the nanoimprint lithography technique was first proposed by Stephen Y. Chou and his students in 1995 to provide researchers with the means they needed to have a high resolution patterning technique with a structural size below 0.1 μm [51].

The term NIL initially referred to a hot embossing lithography (HEL) process, and was also used as a synonym for thermal nanoimprint lithography [51]. However, it now has an extended meaning which includes not only the two fundamental types (Thermal NIL and UV-based nanoimprint lithography, UV-NIL), but also many different variations subsequently developed, such as the roll imprint process, laser-assisted direct imprint, reverse imprint, etc [49]. The former two general methods will be discussed in detail in the following sections.

In the applicable fields the NIL technique can create resist patterns, imprint functional device structures and even on large-areas from micron to nanometer scale. Thus, this leads to a wide range of applications in biotechnology [53], electronics (LED, OLED, flexible display), photonics, data storage (Hard Disk Drive) and so on [49, 54]. NIL has great potential for commercial prospects and its use is growing rapidly in many application fields throughout our life.

2.3.1 Thermal nanoimprint lithography:

In this section, we discuss the mechanisms of thermal NIL and give examples of the requirements for commonly used plastic materials. In the mechanism of thermal NIL, it is important to make sure that the temperature of the material increases to around the glass transition temperature (T_g), so that the polymer reaches a typical viscoelastic behavior. In these states, the polymer becomes soft enough to be imprinted. When the temperature keeps rising above the melting temperature (T_m), the polymer turns into a viscous liquid and the polymer starts to flow [55]. Normally the temperature of thermal NIL is operated between T_g and T_m with a proper casting high pressure. There are two requirements for the thermal NIL process that can be met simultaneously via increasing the temperature above the T_g of the polymer, so that both Young's modulus and the viscosity will drop by several orders of magnitude compared to their respective values at room temperature (Young's modulus for glassy polymers just below T_g is approximately constant over a wide range of polymers, at ~3×10^9 Pa) [54].

Of the thermal plastic polymers, polymethylmethacrylate (PMMA) can be a good candidate. There are several reasons were chosen for imprinting. First, the PMMA polymer does not adhere well to the SiO_2/Si mold due to its hydrophobic surface. Thus it can provide good mold releasing properties which are an essential factor for fabricating all nano-scale features. Second, the shrinkage of the PMMA polymer is less than 0.5% when encountering large changes in heating temperature and casting pressure [51]. This means that the transferred patterns can be stably maintained with little deformation process. An example is shown in Figure 2.3.1 presenting 10 μm circles replicated in a PMMA layer via the NIL technique, revealing the clear transfer of patterns with a specific depth of ~400 nm.

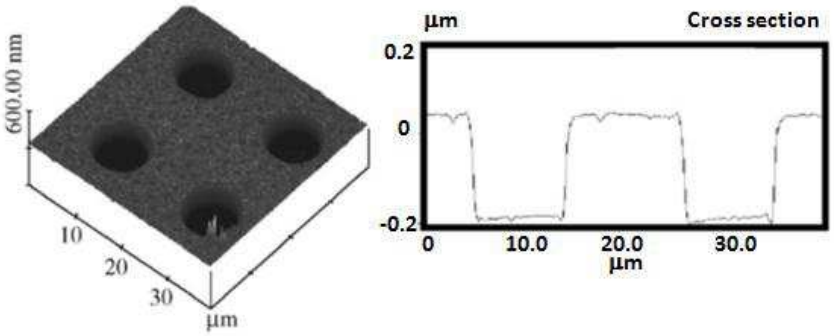

Figure 2.3.1: AFM images of 10 µm circles replicated in a PMMA layer by the NIL technique with an imprint force of 1000 N. [56]

The formation of a silicon mold can be accessed by another etching technique like electron beam lithography. The mold can be comprised of gratings or periodic cylinders that are quite characteristic of the transfer performance. Mold engineering has been improved to meet more and more imprinting requirements. Up to now, the mold can be of any desired morphology, where the focused ion beam (FIB) technique is used to directly "carve out" the desired mold features. Thus it is even possible to achieve 3D or gray-scale patterns that are generally very difficult to fabricate, or would sometimes involve multiple steps including other lithographic techniques to obtain. An example of such a structure fabricated by FIB is shown in Figure 2.3.2. FIB may find many uses in NIL-related applications with more complicated molds in the future [54].

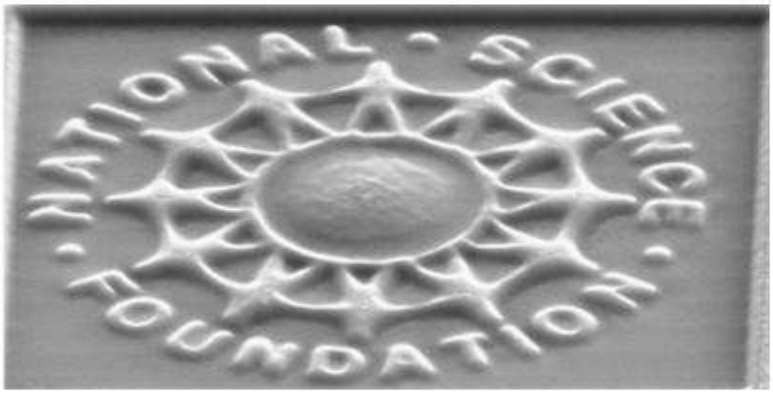

Figure 2.3.2: Mold fabricated by using FIB (a gray-scale pattern of the NSF logo).

2.3.2 UV-curable nanoimprint lithography:

Since 1995, nanoimprint lithography using the hot embossing technique (or thermal NIL) has attracted much attention as an alternative method comparing to conventional lithography. Another promising approach for UV-curable NIL was established as an alternative to the thermal NIL and has now become another common method just as important as the standard thermal NIL.

The UV-curable technique was first proposed by Haisma et al. in 1996 [57]. The thermal NIL process requires high temperatures and heavy pressures for the nanoimprinting of thermoplastic materials. These could limit the throughput for mass production via NIL techniques. On the other hand, the thermal expansion mismatch between the mold and the substrate often presents an obstacle for pattern overlay over large substrates. An alternative is to use liquid precursors that can be cured by UV light at ambient temperatures. For such materials, the low Young modulus and low viscosity requirements are naturally satisfied. The low viscosity of the monomer fluid makes the imprinting process is less sensitive to the effects of pattern density reported for NIL [54]. There are two main polymer classes, which could be considered for the curing system: acrylates (free-radical polymerization) and epoxy compounds (cationic polymerization). The former shows higher polymerization reactivity and faster curing rates than epoxy systems [58]. The curing reaction initiated by UV light is shown in Figure 2.3.3.

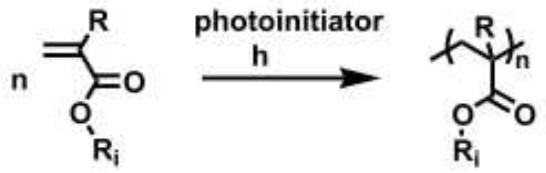

Figure 2.3.3: Free-radical polymerisation of (meth)acrylates initiated by UV exposure (acrylates R=H, methacrylates R=CH_3, R_i various functional groups). [58]

The process for UV-curable NIL is similar to thermal NIL techniques as shown in Figure 2.3.4. The difference is that a UV-transparent mold is pressed into a liquid resist layer and then hardened by exposure to UV-light at room temperature. The defined patterns in the resist can then be transferred into the underlying substrate via etching, much like the exposed and developed resist layers in conventional lithographic technologies [59] . Compared to thermal NIL, a low imprinting pressure is still needed for UV-curable NIL, which must be sufficient to initiate lateral resist flow into the mold cavities. In addition the casting pressure should be large enough to compress the air inside the cavity or to dissolve it. If the environmental air pressure before the mold to sample contact is lowered, the amount of air trapped inside the cavities is reduced significantly and therefore the pressure required to initiate the lateral resist flow is minimized [60].

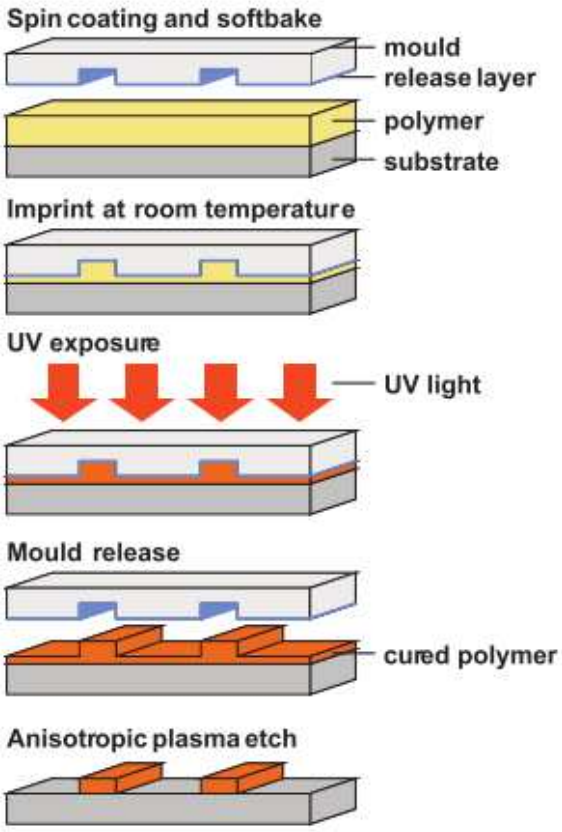

Figure 2.3.4: Illustration of the process of UV-curable NIL. [58]

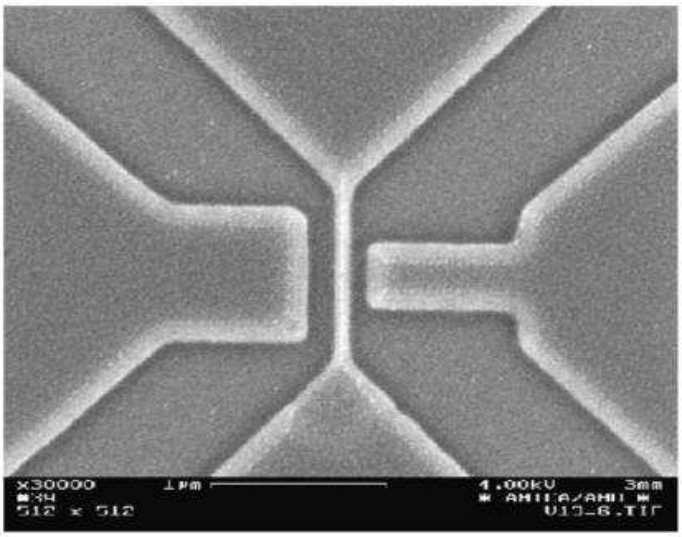

Figure 2.3.5: SEM micrograph of a printed narrow channel transistor with a width of 80 nm and depth of 200 nm, transferred into silicon via UV-curable NIL. [59]

2.3.3 New material developments:

The rapid growth of NIL in recent years has led to the use of more and more new materials as a nanoimprint resist for further development. In NIL, there can be a reduction in precision caused by distortion of the imprinted structure or stamp features due to the thermal cycle of heating followed by cooling. To overcome these problems photo-curable monomers are used for polymerization during the imprint process. However, this procedure generally utilizes transparent quartz stamps that require a complicated fabrication process and thus this becomes more expensive than the usual silicon stamps [61]. Therefore a transparent and low-cost material in the UV range is required for photo-curable methods. Several types of polymer systems have been investigated, for example, one of the promising materials is a thermally curable Polydimethylsiloxane (PDMS)-based liquid resist that can be imprinted with high precision, UV-transparency and is very quickly for thermally crosslinked [54]. Until now, PDMS has been used in many nano-lithography techniques, which are also referred as ‘soft lithography’ [62, 63].

A combined UV-curable NIL technique, the Soft UV-Nanoimprint technique, featuring transparent flexible molds and low viscosity UV-curable resist has been developed, which enables the definition of high aspect nanostructures on the wafer scale. PDMS is then used as a standard mold material due to its favorable properties such as flexibility and UV-transparency [64].

On the other hand, the polymer, PDMS, has a much lower surface energy [65] compared to the vast majority of resists used for thermal NIL methods such as PMMA and polystyrene (PS). Thus this polymer can also directly replicate any structure and even organic morphology like the lotus [12] because of its low surface energy, flexibility and good chemical stability.

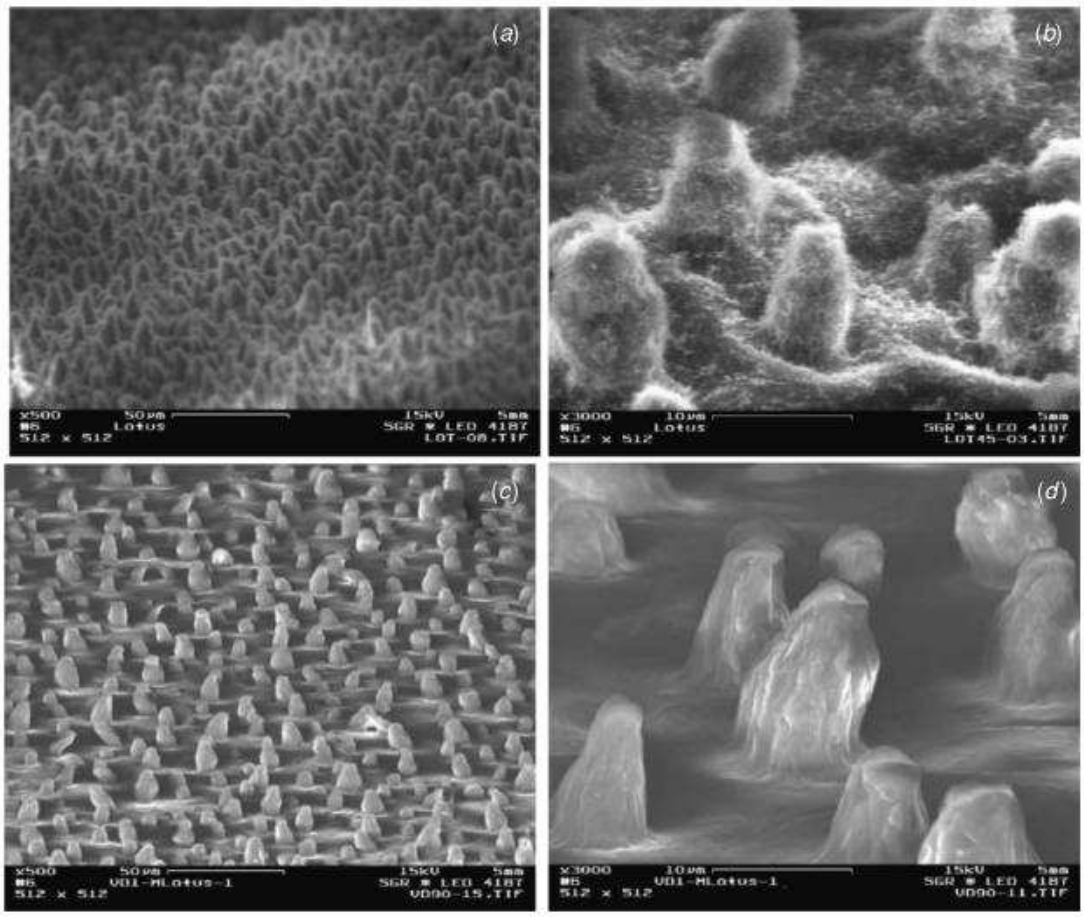

Figure 2.3.6: SEM images of a natural lotus leaf (a) and (b) and the replicated surface (c) and (d). Angle of view: 75° except for (b) 45°. The scale bar correspond to 50 µm on (a), (c) and to 10 µm on (b), (d). [12]

Chapter 3: Experimental framework and methods

3.1 Experimental framework

The important exitonic features in quantum dots motivated us to study the quantum dots experimentally and to investigate their optical properties. An easy method to study quantum dots experimentally is to disperse them in a solvent. However, this liquid state is not convenient for application when compared to thin films and devices. Therefore, we proposed embedding the QDs into polymer thin films, such as PMMA, making hybrid layers of PMMA/QDs. The choice of PMMA is made because of its transparency in the near UV and visible range making it a potential candidate for the hosting matrix. Thanks to the highly luminescent properties of these QDs, we then demonstrated this hybrid layer/QDs can be applied to solar cells.

After obtaining the optical properties of hybrid thin films/QDs, we structured these hybrid thin films/QDs into periodic structures in order to further control the spatial distribution of the highly luminescence light of QDs. The structured hybrid thin films were fabricated by the thermal nanoimprint method due to the softened PMMA polymer above the transition temperature. After the optimized nanoimprint, the transferred structural characterization of hybrid thin films and their simulated optical field distributions were performed.

To summarize, the framework can be divided into several principle directions as follows. In these parts, the analysis methods, such as the size determination technique, determination of periodic properties and optical field calculation, are separately represented.

<Part I> Hybrid Polymer Thin Films with Quantum Dots

In the first part, the purpose is to focus on characterizing the intrinsic optical properties of CdSe/ZnS QDs by embedding them into PMMA polymer thin films. Different characterization techniques are used. The major types of analysis performed are as follows:

(1) The absorption spectrum: deduced from spectrophotometer results;

(2) Excited luminescence spectrum: by photoluminescence measurement;

(3) Luminescent intensity variation: by time-resolution photoluminescence;

(4) Observation of QDs size and distribution: by TEM measurement.

<Part II> Nanostructured Hybrid Polymer Films with Quantum Dots

(1) The transition temperature (T_g) ➔ The heating variation with fixed pressure;

(2) Morphology and periodic properties ➔ Chromatic confocal measurement;

(3) Optical field prediction ➔ Finite-difference time-domain simulation;

(4) Diffraction pattern induced by nanostructure ➔ He-Cd c.w. laser;

(5) Excited luminescence spectrum ➔ Photoluminescence measurement.

A flow chart of the major parts of the experiment is then shown in Figure 3.1.1.

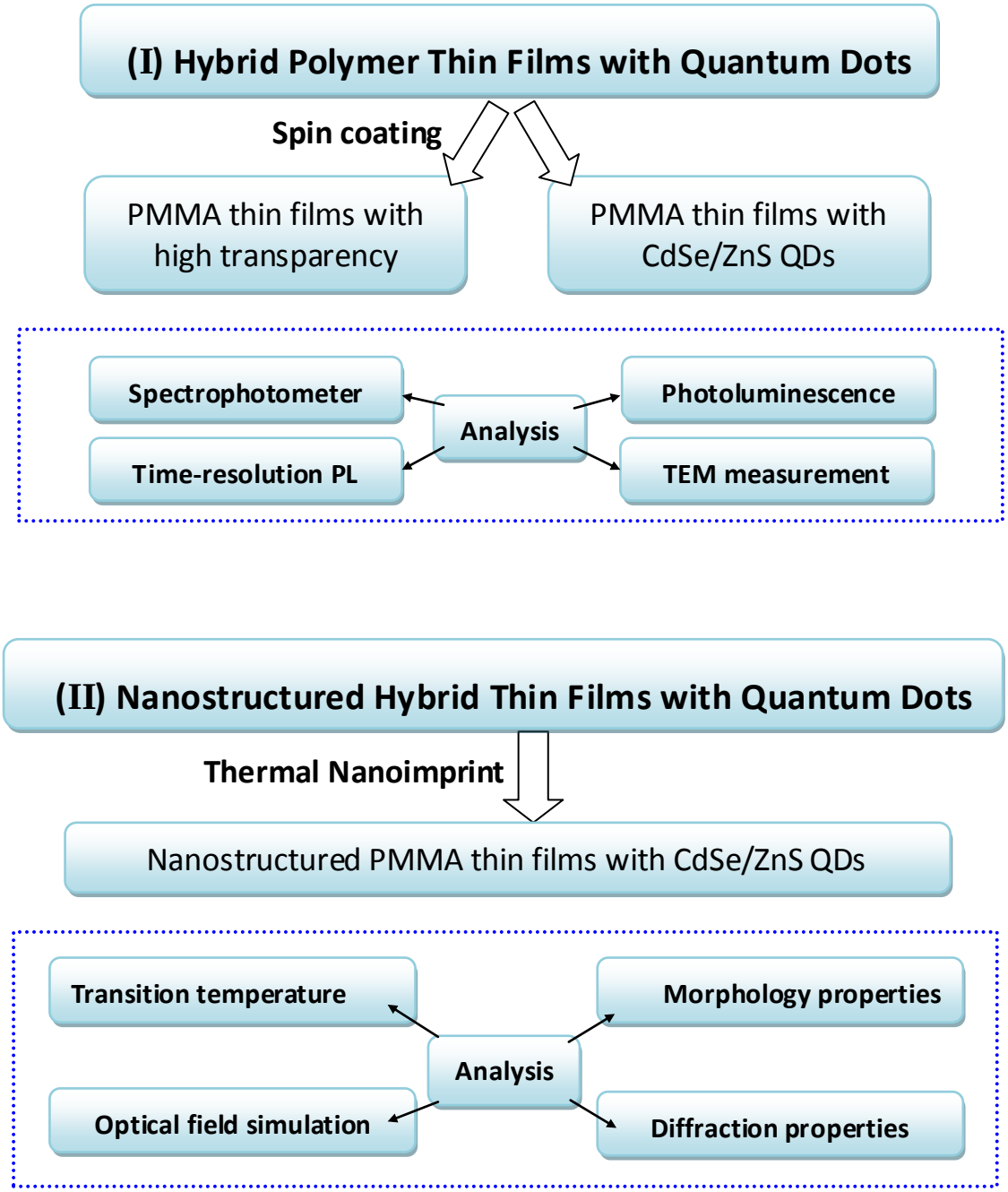

Figure 3.1.1: Flow chart of the experiment.

3.2 Spin coating method – Hybrid Thin Films/ QDs

Spin coating is a widespread practice in modern science and engineering, where it is used to deposit uniform coatings of particulate matter on a flat surface [66]. It is a fast and easy way to fabricate cheap and homogeneous thin layers. Therefore we applied this method to coat our hybrid thin films with QDs. By extracting an excess amount of solvent from the as-prepared polymer solution contained QDs, it is then casted onto the substrate that is then rotated at high angular speed. The residual fluid is therefore forced out of the film by centrifugal force and a solid film is formed. The spin coating method also has many other applications such as use in microelectronics to coat a photoresist on silicon wafers for the lateral process of lithographic patterning [67, 68].

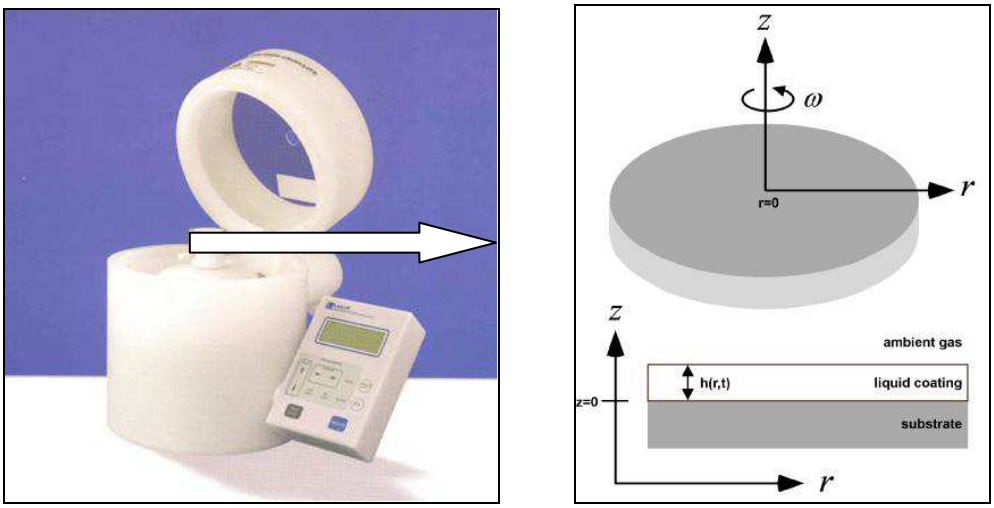

Figure 3.2.1: Illustration of spin coating (Laurell Technologies Corporation) and description of the related mechanism of spin coating. [66]

Figure 3.2.1 shows an illustration of the spin coater (Laurell Technologies Corporation) utilized in the experiments. The coating process is illustrated in detail on the right hand side of this figure. The rotating plane is horizontal so there is no radial gravitational component and the liquid layer is so thin that

differences in gravitational potential normal to the surface is negligible [66]. To further simplify the problem, one or more additional approximations could be made: that the rotating plane be infinite; that the liquid layer be radically symmetrical, and so on [66]. Some theoretical analyses of spin coating based on the principles of hydrodynamics have been investigated because of the systematic physics and mathematical complexity [69-71]. Concerning the final film thickness, there are several important factors which shall be considered:

(1)Viscosity and concentration of the solution

(2)Rotational speed and time

However, the disadvantage of this spin coating method is that the proper solvent is limited. Taking the quantum dots we used as an example, they are soluble in toluene, hexane and chloroform but not in ethanol or acetone. Therefore, the solubility characteristics of the QDs in the chosen solvent should be well-known before the spin coating.

3.2.1 Rotational speed and time:

For most of the resin materials, the coated thicknesses are inversely proportional to the spin speed and spin time. The spin starts, as the solution covered the substrate. We find sometimes there are problems as listed in Figure 3.2.2. (1) The layer is too thin. This might be caused by too fast a spin speed or too long a spin time. (2) The surface of the substrate reveals some uncoated areas. The possible reason might come from insufficient dispensing quantity of the solution or inhomogeneous dispense. (3) The coated thin films have some visible air bubbles inside the films. This might be due to residual air in the dropper which was not yet squeezed out.

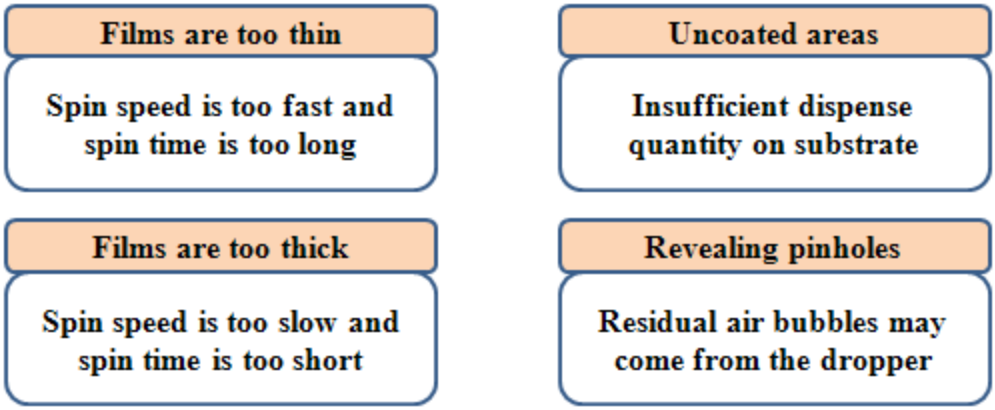

Figure 3.2.2: Problems and related reasons encountered during spin coating process.

3.2.2 Viscosity and concentration of the solution:

The viscosity and concentration of the solution will influence the coated film thickness. As shown in Figure 3.2.3 a larger viscosity or concentration brings out a thicker film and vice versa.

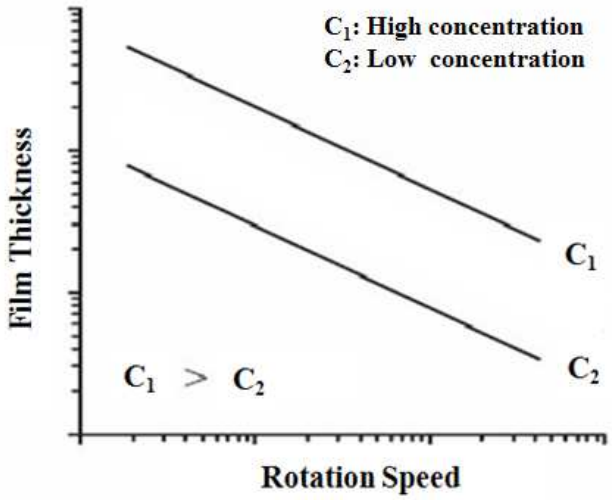

Figure 3.2.3: Variation of film thickness against rotational speed with solution concentration.

3.3 Measurement methods

3.3.1 Spectrophotometer- transmission and reflection measurement:

We used a HITACHI U4100 commercial spectrometer to measure the spectrum of the deposited samples. The spectrometer was equipped with light sources of a halogens tungsten filament lamp (W1 lamp) and a deuterium lamp (D2 lamp) the range of wavelengths from 190 nm to 3500 nm. The spectrometer combined an integrated sphere to eliminate the noise in measurement.

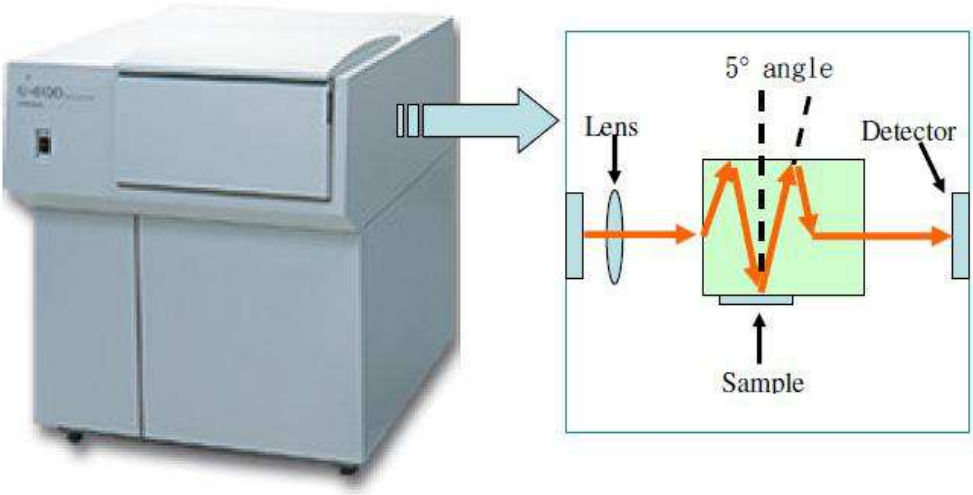

Figure 3.3.1: U-4100 Spectrophotometer.

3.3.2 Photoluminescence measurement:

Concerning the photoluminescence (PL) measurement, it is a contactless, nondestructive method to obtain the electronic structure of materials. The PL applied phenomenon involving absorption of high energy photons and then subsequent emission of light from material itself under the term luminescence.

Radiative transition:

There are several possibilities for returning to the ground state. The observed emission from a luminescent center is a process of returning to the ground state radiatively. The luminescence quantum efficiency is defined as the number of photons emitted divided by the number of photons absorbed, and in most cases is equal to the ratio of the measured lifetime to the radiation lifetime of a given level. The processes competing with luminescence are radiation transfers to another ion and nonradiation transfers such as multiphonon relaxation and energy transfer between different ions or ions of a similar nature [72].

Figure 3.3.2 shows the configuration coordinate diagram in a broad band emission. Assumptions are made of an offset between the parabolas of the ground state and the excited state [72]. Upon excitation, the electron could be excited in a broad optical band with higher photon energy than material energy bandgap and brought in a high vibrational level during the excited state. The center thereafter relaxes to the lowest vibration level of the excited state and gives up the excess energy to the surroundings. This relaxation usually occurs nonradiatively. From the lowest vibration level of the excited state, the electron returns to the ground state by means of photon emission [72]. Therefore, the difference in energy between the maximum of the excitation band and that of the emission band is found. This difference is called the Stokes shift [73] where the red-shifted energy generally occurs.

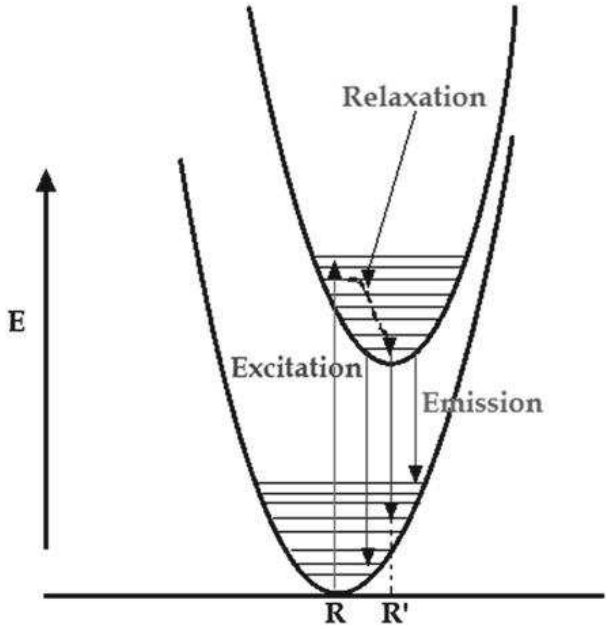

Figure 3.3.2: Configuration coordinate diagram for a broad band emission. An assumption is made on an offset between the parabolas of the ground state and excited state. [72]

Non-radiative transition:

The energy absorbed by the luminescent materials which is not emitted as radiation is dissipated to the surrounding crystal lattice. The relaxed-excitation state may reach the crossing of the parabolas if the temperature is high enough [72] in which case, it is possible for electrons to return to the ground state in a non-radiative manner. The energy is released as heat to the lattice during the process [74]. The non-radiative processes competing with luminescence causes energy transfer to the local vibrations of atoms, which are usually called phonons in solids. Generally, non-radiative transitions mainly come from materials through indirect energy bandgap with the assistance of phonons.

3.3.3 Spectroscopic ellipsometry [75, 76]:

In our research, spectroscopic ellipsometry (Sopra GES-5) was used to measure the optical constants and thickness of thin films. When light is reflected from an isotropic dielectric surface, the ratio of reflective coefficients r_s and r_p of S-polarization and P-polarization is measured

$$r_s = |r_s| e^{i\delta_s} \tag{3.3.1}$$

$$r_p = |r_p| e^{i\delta_p} \tag{3.3.2}$$

where $|r_s|$ and $|r_p|$ are the amplitudes of the reflection coefficients, and δ_s and δ_p are the phases of the reflection coefficients. Then the ellipsometric function (ρ) and the ellipsometric angles ψ and Δ are defined:

$$\rho = \frac{r_p}{r_s} = \frac{|r_p| e^{i\delta_p}}{|r_s| e^{i\delta_s}} = \frac{|r_p|}{|r_s|} e^{i(\delta_p - \delta_s)} = \tan\psi \times e^{i\Delta} \tag{3.3.3}$$

By fitting the values of ψ and Δ with the Fresnel equation and Snell's law, the optical constant and physical thickness of thin films can be derived.

3.3.4 Transmission and scanning electron microscopy:

Electron microscope (EM) is an imaging technique based on the interaction of electrons with matter. Therefore, it can help us to obtain different information such as:

a) Crystalline structure, **b) Microstructure** and

c) Chemical element compositions and bonding analysis.

In many scientific fields, electron microscopes, and especially transmission electron microscopes and scanning electron microscopes form the primary tools for analysis due to their high resolution for determining the morphology and material structure. We will first introduce their principles.

3.3.4(a) Transmission electron microscopy:

The transmission electron microscope (TEM) is capable of imaging at a significantly higher resolution than the optical microscope because of the small de Broglie wavelength of the electrons. This enables us to examine very fine details of the prepared samples even at the atomic scale, which is tens of thousands of times smaller than the smallest resolvable object in a optical microscope [77, 78]. The beam of electrons is transmitted through an ultra-thin specimen, interacting with the specimen as it passes through [77]. An electron image is formed from the interaction of the electrons transmitted through the specimen. In the end, this image information will be magnified and focused onto a fluorescent screen or recorded by a CCD camera [78]. The most important application of TEM is the atomic-resolution real-space imaging of nanoparticles. By forming a nanometer size electron probe, TEM is uniquely able to identify and quantify the chemical and electronic structure of individual nanocrystals [79]. The TEM includes four systems [77, 78]: (1) **emission gun system**: which

uses different emission methods such as thermionic emission by LaB_6 crystal or field emission gun to extract the electrons via strong electric field; (2) **electromagnetic lens system**: this system contains condenser lenses for obtaining high power and small spot electron beams. Objective lenses are applied for focusing electron beams. Intermediate lenses are mainly for determining magnification and projective lens are utilized for projecting the final electron image on a (3) **fluorescent screen or CCD system**; (4) **specimen holder**: used for inserting samples. A basic TEM system is shown in Figure 3.3.3 (a). Figure 3.3.3 (b) gives an example of high resolution TEM images of Pt nanocrystals.

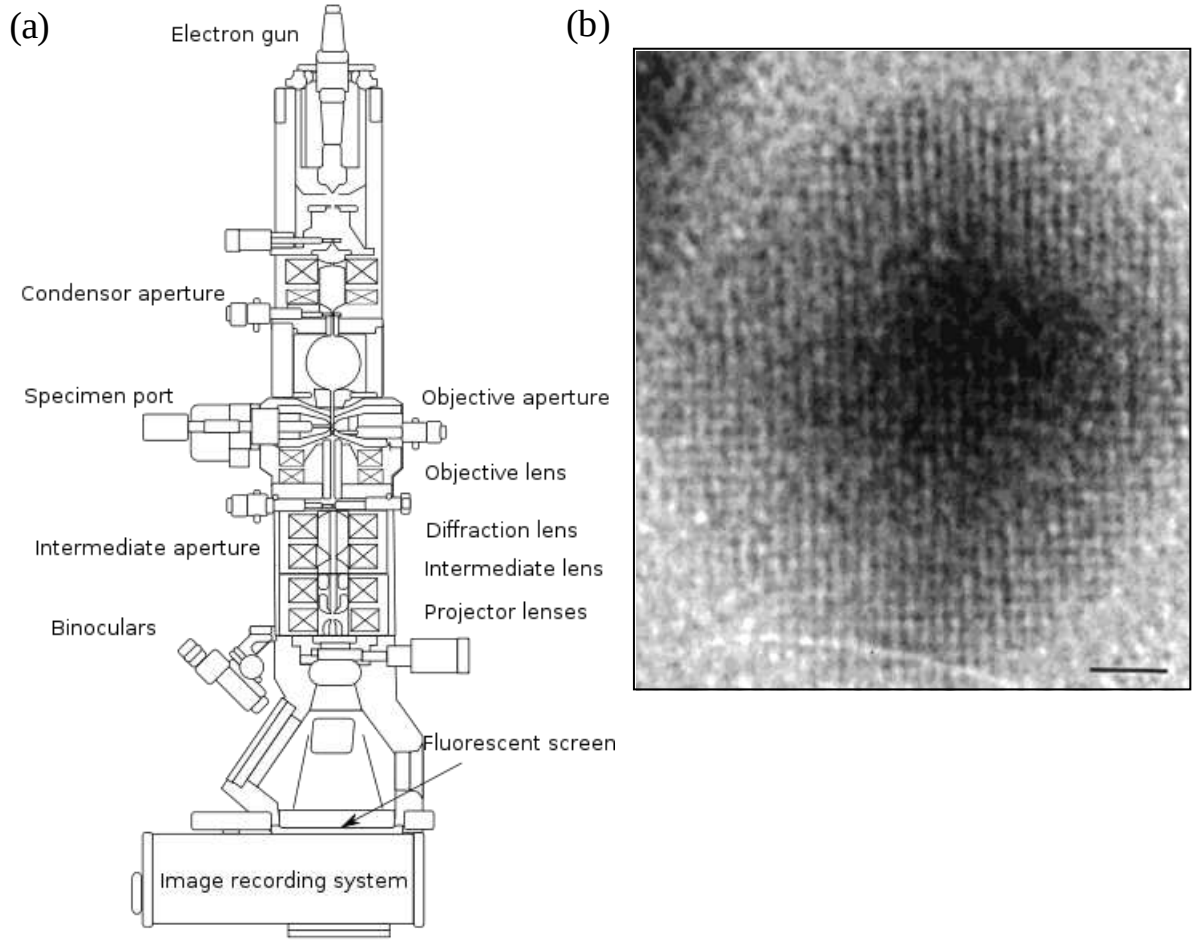

Figure 3.3.3(a) Diagram outlining the internal components of a basic TEM system (image provided by Gringer) (b) High resolution TEM images of Pt nanocrystals. [79]

Taking TEM of JEM-2000 FX II (JEOL) for example, the point image can stand for 0.28 nm and acceleration voltage can be tuned from 80, 100, 120, 160 and 200 kV. Based on the diameter of the electron beam between 1 μm ~ 2 nm, a high degree of magnification can therefore be achieved ranging from 50X to 800,000X.

Limitations of TEM [77, 78]:

There are several shortcomings with TEM measurements such as the sample size needing to be within 3 mm, the ideal thickness for observation is between 50-100 nm due to the limitations of electron penetration, powder samples or unstable samples in vacuum are not suitable, the sample preparation is very hard. Moreover, it takes a very long time to create a suitable sample for examination, and it is a destructive process.

3.3.4(b) Scanning electron microscopy:

The scanning electron microscopy (SEM) [80, 81] contains four principal systems: (1) **Specimen holder**: is a small chamber located by the side of SEM for exchanging the samples into the following high-vacuum surroundings of electron gun and lens system; (2) **electron gun system**: used for providing a stable beam of electrons; (3) **electron lens system**: includes a condenser lens, aperture and an objective lens that magnifies, directs and shapes the electron beam to produce the desired electron beam spot on sample scanning; (4) **electron image detecting system**: the final scanning images are recorded by detectors including solid state detectors and scintillators which detect the electrons with weaker energy like secondary electrons. In general, SEM applies the above focused high-energy electron beam to generate a variety of signals on the surface of solid samples. After the electron-sample interactions, the signal

can be derived for information about the sample including external morphology, structure and even chemical composition.

An example of a field emission scanning electron microscope (FESEM) (JEOL JSM-6700F) can be seen in Figure 3.3.4. This system provides electron acceleration voltages from 0.5 kV ~ 30 kV and image magnification from 25X to 650,000X with possible resolutions of ≅ 1 nm.

Figure 3.3.4: FESEM JEOL - JSM-6700F.

Limitations of SEM:

Samples prepared for SEM measurement should be in a solid state and must fit into the holder for transferring into the microscope chamber. Normally the maximum sample size in horizontal dimensions is limited in the order of a centimeter or even smaller. Also, the sample must be quite stable in a vacuum environment on the order of 10^{-4} ~ 10^{-6} Torr. For example, if it outgases under vacuum, it would be unsuitable for measurement.

3.3.5 Atomic force microscopy:

The atomic force microscopy (AFM) can achieve a high-resolution image through measuring the force between a sharp solid probe and surface within a very short distance. This very short distance, from 2-100 Å probe-sample separation in the near-field of the material surface, is used in the investigation.

The AFM technique is the first instrument capable of directly obtaining 3-D images of solid surfaces with atomic resolution. This concept was first proposed out by G. Binning *et al* [82]. Based on the scanning tunneling microscope which was proposed as a method to measure forces as small as 10^{-18} N, Binning then introduced another new type of microscope capable of investigating surfaces of insulators on an atomic scale which combines the principles of the scanning tunneling microscope and the stylus profile meter [82]. The advantage of this measurement is that it incorporates a probe so that damage of the sample surface can be avoided. Therefore, there are enormous applications [83] such as the roughness of polymeric [84, 85] and ceramic membranes [86]. Examples of AFM images are given in Figure 3.3.5.

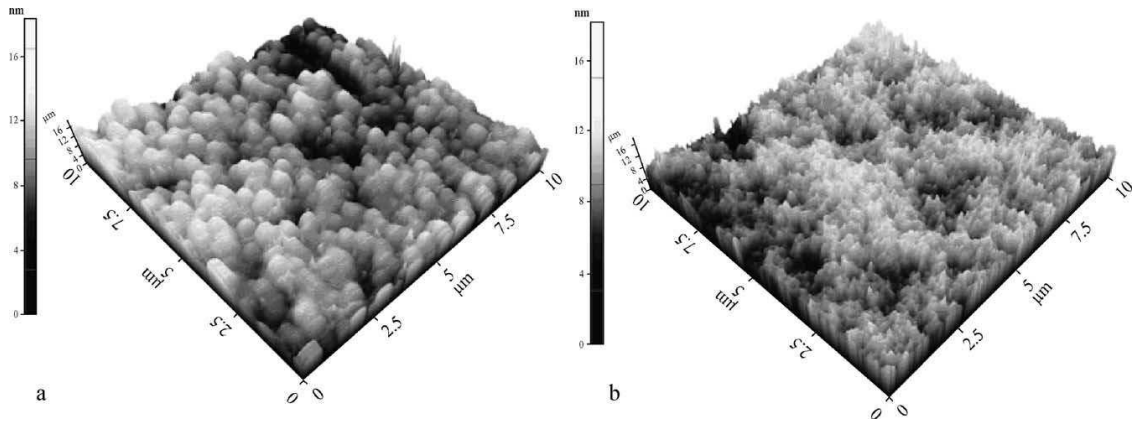

Figure 3.3.5: AFM images of the generated surface on Corning 7740 glass after etching in HF (left figure) and HF/HCl 10:1 (right figure) for different roughness. [87]

There are three AFM techniques: contact mode, noncontact mode, and tapping mode. In contact mode, the tip scans the sample in close contact with the surface.

This means that the interatomic force between the sample and the tip is repulsive, with a typical value of 10^{-7} N [88]. Problems with contact mode are caused by excessive tracking forces applied to the sample by the probe. Therefore, contact mode AFM cannot be applied to soft surfaces, such as polymeric membranes.

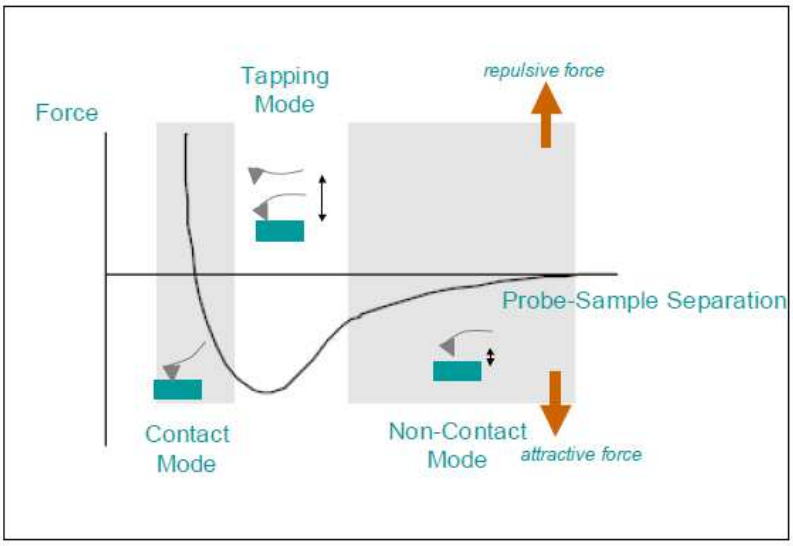

Figure 3.3.6: Plot of force as a function of the probe-sample separation (Robert A. Wilson *et al.*).

Tapping mode AFM allows high-resolution topographic imaging of sample surfaces by alternately bringing the tip into contact with the surface to provide high resolution and then lifting it off the surface to avoid dragging the tip across the surface [88]. Tapping mode imaging is again implemented by oscillating the cantilever assembly at or near the cantilevers resonant frequency using a piezoelectric crystal. The piezo motion causes the cantilever to oscillate with a large amplitude (typically greater than 20 nm) when the tip is not in contact with the surface [88]. The oscillating tip is then moved toward the surface until it begins to gently touch or tap the surface. During scanning, the vertically oscillating tip alternately contacts the surface and lifts off, generally at a frequency of 50,000–500,000 cycles per second [88].

Chapter 4: Hybrid organic thin films/ QDs

4.1 PMMA thin film with CdSe/ZnS QDs

While a semiconductor nanocrystal structure is less than the De Broglie wavelength, the quantum confinement phenomenon of the electrons can make it a promising and novel material with tunable optical properties and luminescence through engineering its size and shape. Cadmium selenide is one of the most widely studied quantum dots materials. CdSe is an inorganic II-IV semiconductor compound. However, the luminescence quantum yield of CdSe QDs is weak due to the presence of defect states on its surface which may give rise to Auger recombination [89]. Therefore, passivation of the surface of QDs with a wider bandgap semiconducting material to form the core-shell quantum dots which confine the exciton within the spherical CdSe core is required to enhance the photoluminescence quantum yield [90]. An illustration of core-shell quantum dots is shown in Figure 4.1.1. Before incorporating these core-shell quantum dots into optoelectronic devices, their optical properties have to be characterized.

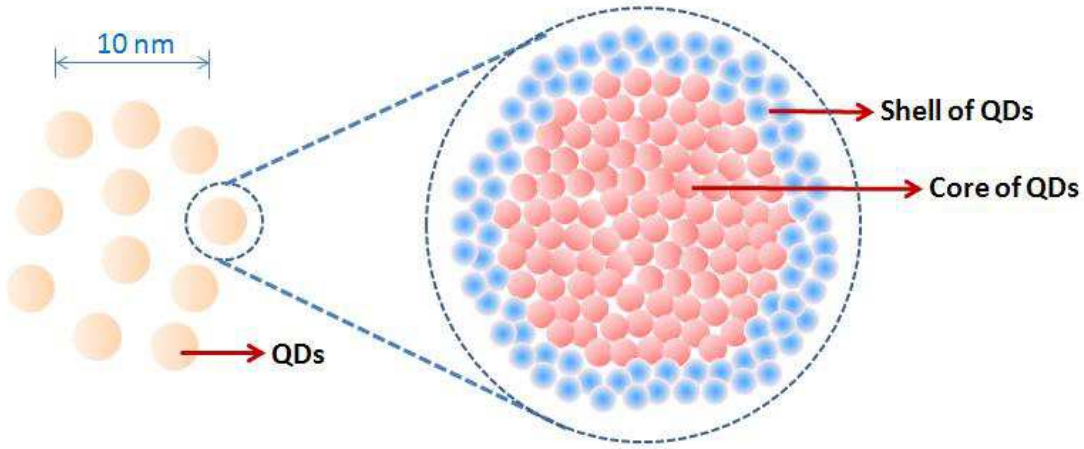

Figure 4.1.1: An illustration of core-shell quantum dots.

Since we understand the importance of obtaining the optical properties of quantum dots to use them in device applications, the question which arises is: how do we measure their intrinsic properties, independently of any solvent of other materials?

In our research, we proposed to incorporate them into a hosting material of PMMA (Polymethylmetacrylate). By controlling the spin rate and weight ratio concentration, we can control the film thickness and quantum dots concentration while forming hybrid thin films. There are different advantages to this approach. The hybrid organic/inorganic thin films are of interest in device applications and embedding QDs could also prevent them from degradation. The following figure reveals that degradation happens when QDs are exposed to "light + oxygen" for a time. Figure 4.1.2 shows an experiment designed to let one bottle (the right uncovered one) stay without any shade for three months. Another bottle with same concentration of QDs was covered in aluminum foil to protect against light exposure.

Figure 4.1.2: The left shaded bottle with QDs reveals the original color but the right uncovered one shows a different blue-shifted color after 3 months of storage.

After taking off the covered aluminum foils on the shaded bottle, we can clearly observe a big difference between them. The left-hand bottle is still the same color. However the right Bottle 2 is revealed to be light green in color, as shown in Figure 4.1.2. A likely reason for this degradation could be caused from the accelerated oxidation when QDs are exposed to light and oxygen at the same time. Thus the oxidation of these dots can change their color towards a blue-shifted hue [91]. In accordance with Wilfried *et al* [91], they presented luminescent measurements of CdSe/ZnS core-shell QDs at different times. A clear blue shift in the emission wavelength of 30 nm could be observed after a few 10s of seconds in ambient air as shown in Figure 4.1.3. In contrast, this shift is not observed for QDs in a nitrogen atmosphere [91].

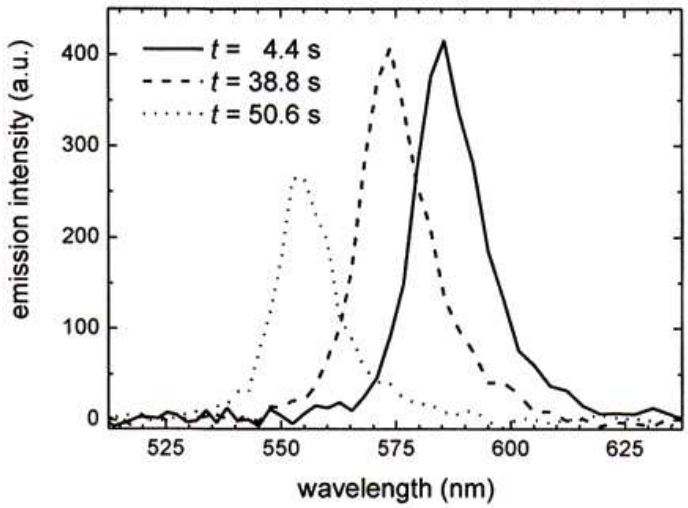

Figure 4.1.3: Emission spectra at different illumination times via a spectrally resolved time trace of CdSe/ZnS QD in ambient air (excitation at 468 nm via Ar-Kr cw laser, power ≅ 20 kW/cm^2, room temperature). [91]

However in their experiment, a very high laser power of 20 kW/cm^2 was applied which therefore amplified the total oxidation process. In our surroundings, the light source only depends on natural solar power which is 100 mW/cm^2 referring to the global solar spectrum [92]. To acquire this solar power,

the testing samples should directly be under the sun to absorb the maximum power. But for possible rainy conditions, the testing samples were preserved near an open window to absorb the surrounding scattered solar light so the power is much weaker than directly under the sun. Therefore, their applied laser power is much more than 2×10^5 times when compared to our surrounding light. So, in our experiments, the bottle with QDs powder is always sealed and shadowed after each time extraction. We study the photoluminescence behavior of QDs embedded in PMMA hosting material. An advantage of this hybrid PMMA/QDs thin film layer is that the QDs luminescent peak stays almost centered at the same wavelength after a few months surrounded by a natural atmosphere and light. Therefore, we deduced that the PMMA can serve the function of "encapsulation" for the QDs.

4.1.1 Introduction of experimental preparation and processes:

In this chapter we discuss the experiment where the PMMA with its molecular weight ≅ 15K (Sigma Chem Corp) was utilized together with different QDs concentration to obtain a possible coupling effect. These core-shell CdSe/ZnS QDs were purchased from Plasma Chem. Their emission peak positions were located at around the wavelength of 560 nm.

We prepared nanocomposite PMMA layers with 4.2 %, 8.3 % and 16.6 % weight ratio percentages (wt %) of CdSe/ZnS QDs. Before making the layers via spin coating, the QDs and PMMA are separately dispersed in a chloroform solvent. To reduce the aggregation of quantum dots, they need to be physically dispersed in the solutions and then mixed with the chloroform solution. After several hours of mechanical stirring by mixed PMMA and QDs, the solution

was shocked in an ultrasonic bath for 15 minutes. Thanks to its good solubility in chloroform, PMMA is a good host material for well-dispersed QDs.

The mixed solution is then spin coated on a silica substrate with a rotating speed of around 2000 rpm to reach a film thickness larger than 1 μm on the substrate. After the spinning process an 80°C heat treatment is required to evaporate the rest of the chloroform solvent. A summary of the above processes is shown in Figure 4.1.4. The spin coating procedure and mechanism can also be visualized by applying centrifugal force to the final evaporation process as shown in the Figure 4.1.5.

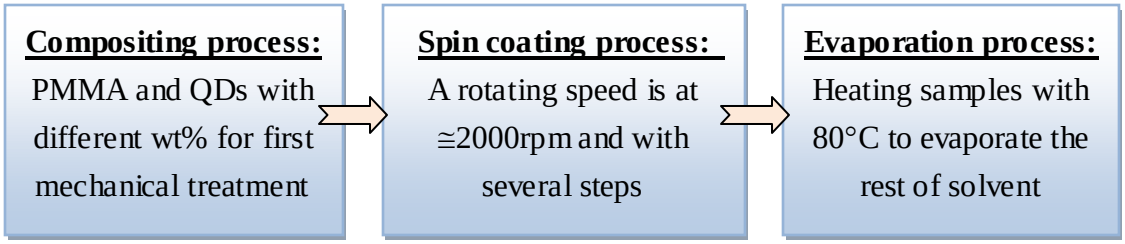

Figure 4.1.4: Flow chart of the hybrid PMMA/QDs films.

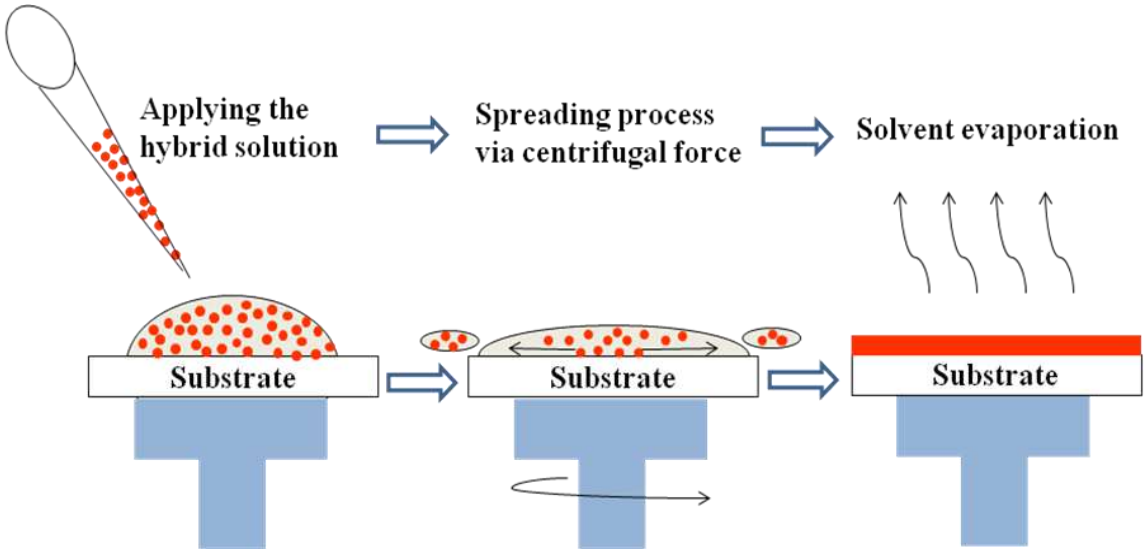

Figure 4.1.5: Illustration of the spin coating process for the fabrication of hybrid PMMA/QDs films.

4.1.2 Electron microscopy measurement:

In order to study the size distribution of QDs in the polymer, the thin films were examined by transmission electron microscopy (TEM). The TEM image obtained is shown in Figure 4.1.6. We can clearly notice that these CdSe/ZnS QDs are well-dispersed. In particular, the atomic image can be observed as patterns of parallel stripes in the right hand side of Figure 4.1.6 (both on the upper and the underside of the figures) due to an incident electron wave emerging from the crystalline part in the material [93]. From these patterns, we can see the distribution and crystallization of these QDs which covered extra passivated ZnS shells around the outward CdSe core. Concerning the several monolayers of ZnS with total thickness of only several angstroms, the global crystallization could be mainly due to the core of QDs. On the other hand, the size of QDs can also be determined approximately at 3 nm in diameter.

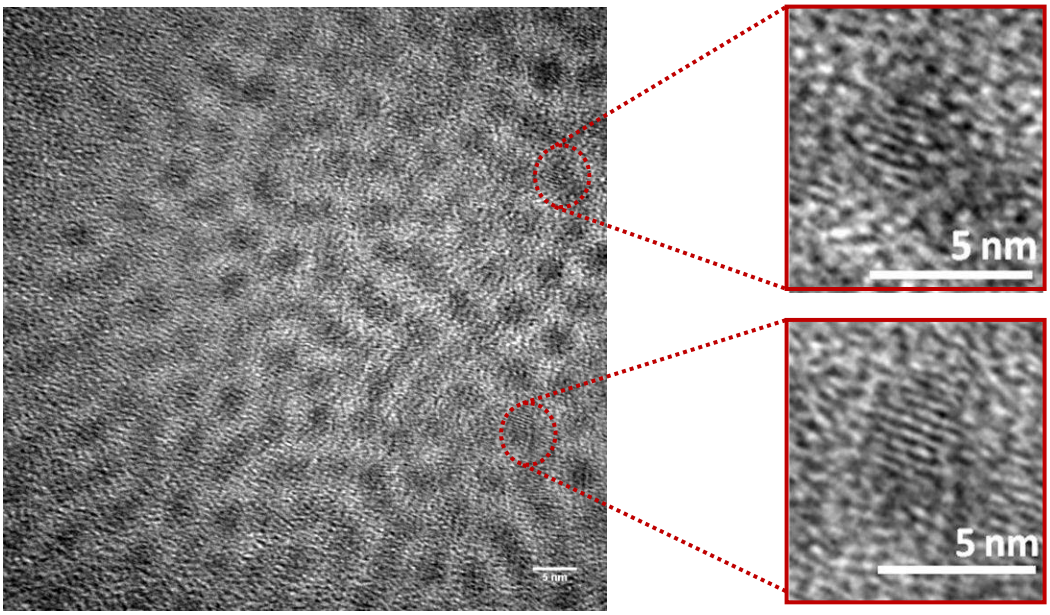

Figure 4.1.6: TEM images of CdSe/ZnS QDs.

4.2 Optical properties of PMMA thin film layers with CdSe/ZnS QDs

4.2.1 Transmission/ reflection and absorption spectrum:

To determine the intrinsic optical properties of QDs, we choose PMMA as the hosting material due to its good transparency in the whole visible spectrum. In this study, PMMA layers containing core-shell CdSe/ZnS QDs with a diameter of 3 nm have been made using the spin coating method. Because of the structure of core-shell QDs, the electrons are easily confined in the structure. Therefore, the strong quantum confinement effect will generate absorption peaks. The experiment is then carefully designed to have samples with different weight ratio percentages (w. r.) of QDs which are of 4.2 %, 8.3 % and 16.6 %. As shown in Figure 4.2.1, transmittance spectrum with different weight ratio percentages were measured by an integral sphere spectrophotometer. It can be seen that the transmittance decreases when the QD weight ratio percentage increases. On the other hand, the transmittance spectrum of 16.6 % QDs reveals interference ripples in the range of 575 nm to 800 nm that are more pronounced than the other two samples.

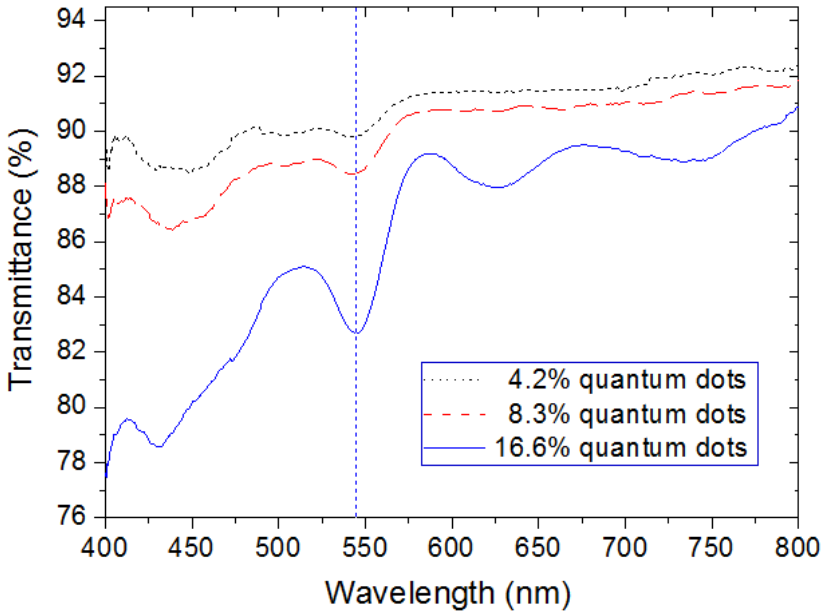

Figure 4.2.1: Transmittance spectrum of CdSe/ZnS QDs for three weight ratio percentages.

The increase in QDs concentration induces an increase of the effective refractive index leading to stronger interference effects. After measuring the transmittance and reflectance spectra, the absorption could be determined as shown in Figure 4.2.2. All samples exhibit the same absorption shape with an absorption peak close to 545 nm. As expected, the absorption increases with the weight ratio percentage. Other absorption peaks at 505 nm and 445 nm appeared when the percentage of QDs increased. They are thought to be induced by exciton transitions between discrete levels in the QDs [90]. As the PMMA has a large bandgap at around 5.6 eV [94], it does not affect the absorption in the near UV and visible spectral range. Using these hybrid thin films we can attribute the optical absorption only from the QDs in the visible spectral range. In addition, the optical properties from the QDs may be influenced by their coupling when raising the QDs concentration.

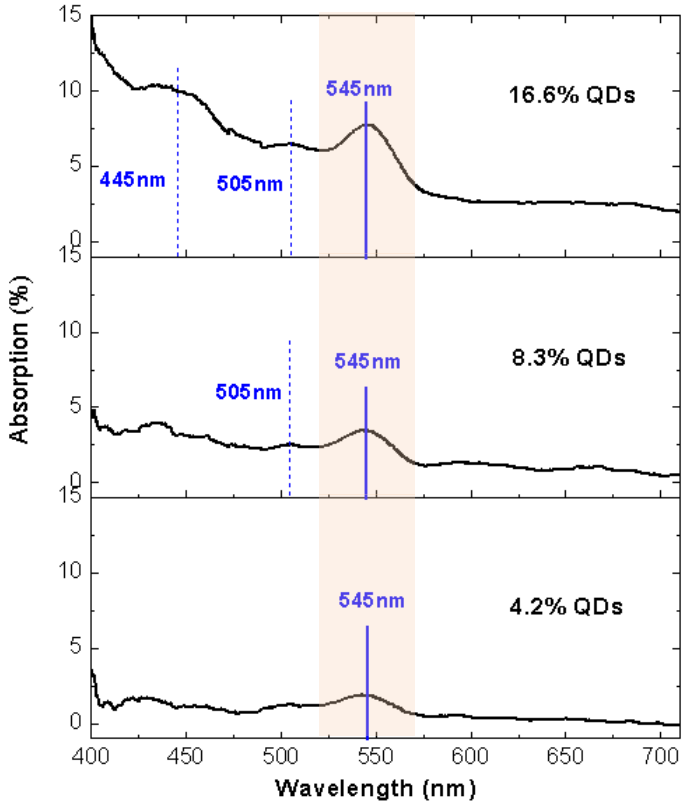

Figure 4.2.2: Absorption spectrum of CdSe/ZnS QDs with weight ratio percentages of 4.2 %, 8.3 % and 16.6 %.

To analyze the first absorption peak of Figure 4.2.2 in detail, we attempted to fit them by Lorentian and Gaussian curves. We found that a Gaussian curve can give a good fit for the absorption peaks, as shown in the figures below. From the fitting curves, the position of the first absorption peak including its maximum and HWHM can be then determined. The results are shown in Table 1.

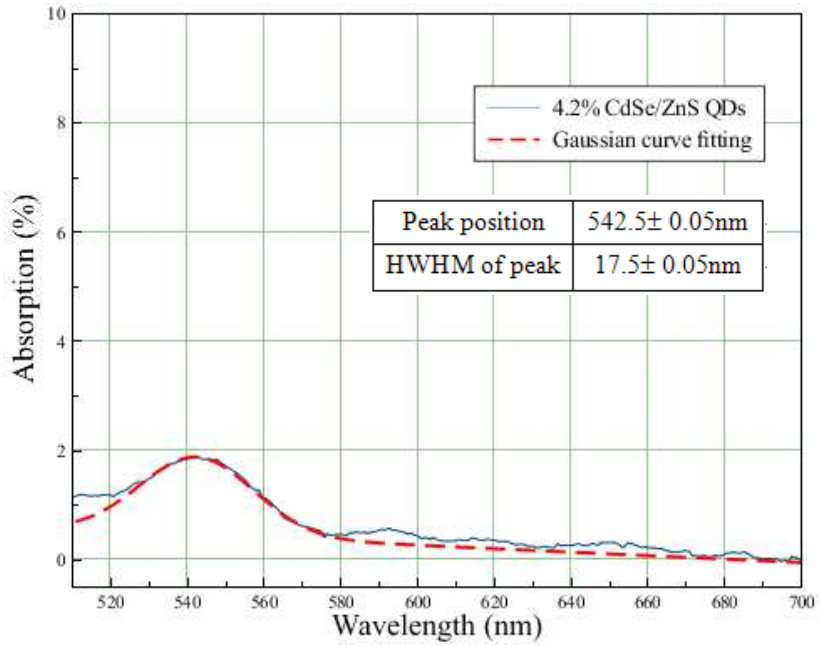

Figure 4.2.3: First absorption peak of 4.2 % CdSe/ZnS QDs fitted by a Gaussian curve.

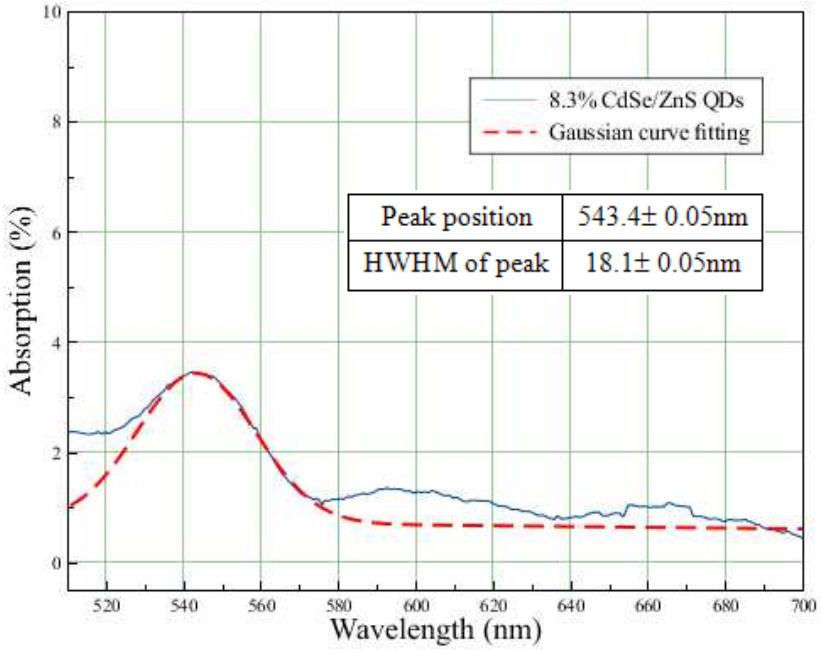

Figure 4.2.4: First absorption peak of 8.3 % CdSe/ZnS QDs fitted by a Gaussian curve.

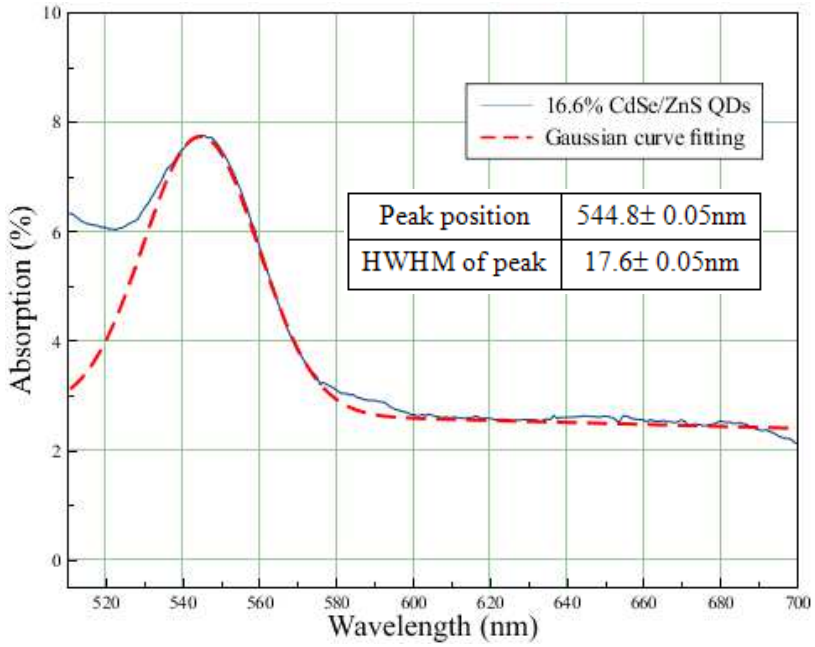

Figure 4.2.5: First absorption peak of 16.6 % CdSe/ZnS QDs fitted by a Gaussian curve.

Comparing the values shown in Table 1, an interesting result can be observed, namely the center wavelength of the first absorption peak shifts to a longer wavelength from 542.5 ±0.05 nm to 544.8 ±0.05 nm. This corresponds to the increasing weight ratio concentration of QDs from w.r. 4.2 % to w.r. 16.6 %. Therefore, the red-shift of the first absorption peak shown in Table 1 could be attributed to QDs coupling when their concentration increases. We will see (in section 4.2.2 and 4.2.3) that the QDs coupling effect can also be verified by a red-shift in the photoluminescence peak.

Table 1. Center wavelengths of first absorption peaks and related Gaussian curve fittings obtained with PMMA layers containing w.r. 4.2%, w.r. 8.3% and w.r. 16.6% QDs.

Samples	Center wavelength (1^{st} absorption peak) (nm)	Gaussian curve Amplitude	Gaussian curve HWHM (nm)
4.2% QDs	542.5± 0.05	1.4± 0.05	17.5± 0.05
8.3% QDs	543.4± 0.05	2.7± 0.05	18.1± 0.05
16.6% QDs	544.8± 0.05	5.0± 0.05	17.6± 0.05

On the other hand, Table 1 also shows that the amplitudes of the Gaussian curves linearly increased and are nearly proportional to the weight ratio concentration of the QDs. The HWHM of the Gaussian curves are almost the same which indicates that the three samples nearly have the same extent of size variation.

Since Figure 4.2.2 shows strong exciton features in the absorption spectrum when the wavelength is around 400 nm to 700 nm, it could be interesting to see the optical properties at shorter wavelength in the near UV. As shown in Figure 4.2.6, the transmittance spectrum extending to wavelengths of 256 nm was measured by a commercial spectroscope. In Figure 4.2.7, the reflectance spectrum of 16.6 % QDs reveals a drop in the envelope of the interference fringes at 545 nm because of the first absorption peak being located at this wavelength. From the transmittance and reflectance spectra, the absorption spectrum was obtained as shown in Figure 4.2.8.

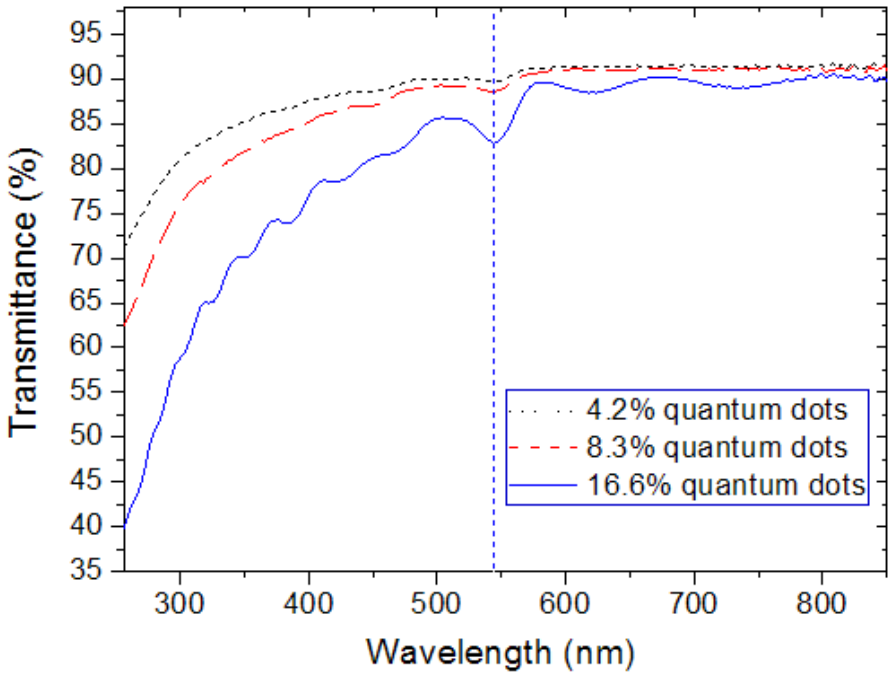

Figure 4.2.6: Transmittance spectrum of CdSe/ZnS QDs measured at wavelengths ranging from 256 nm to 700 nm.

Also, an obvious quantum effect is revealed in the absorption spectra which exhibits the excitonic features superimposed on a continuous background.

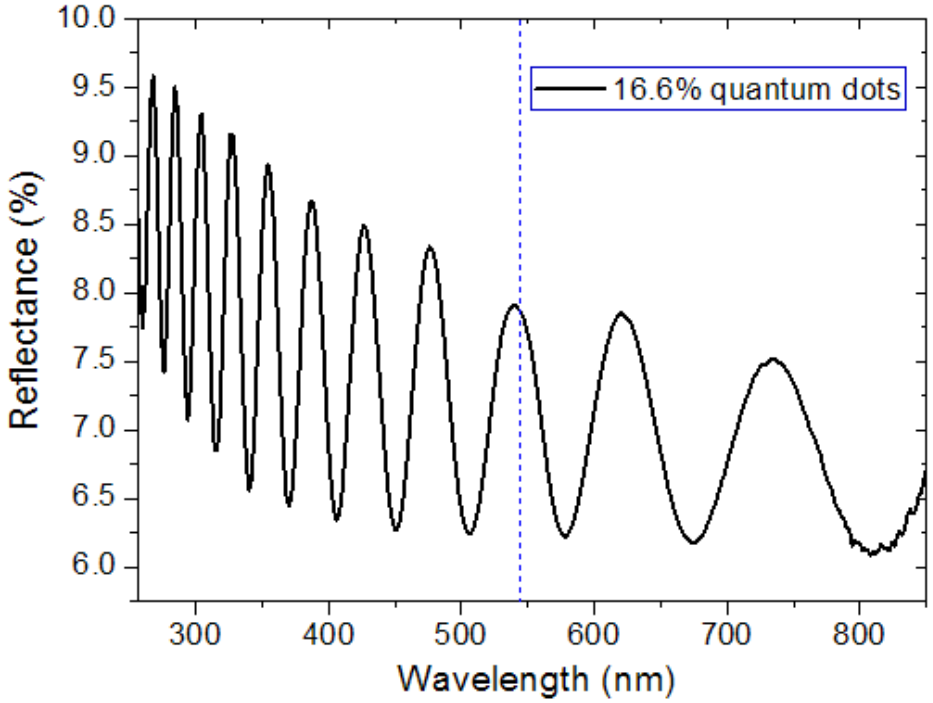

Figure 4.2.7: Reflectance spectrum of 16.6 % CdSe/ZnS QDs measured at wavelengths ranging from 256 nm to 700 nm.

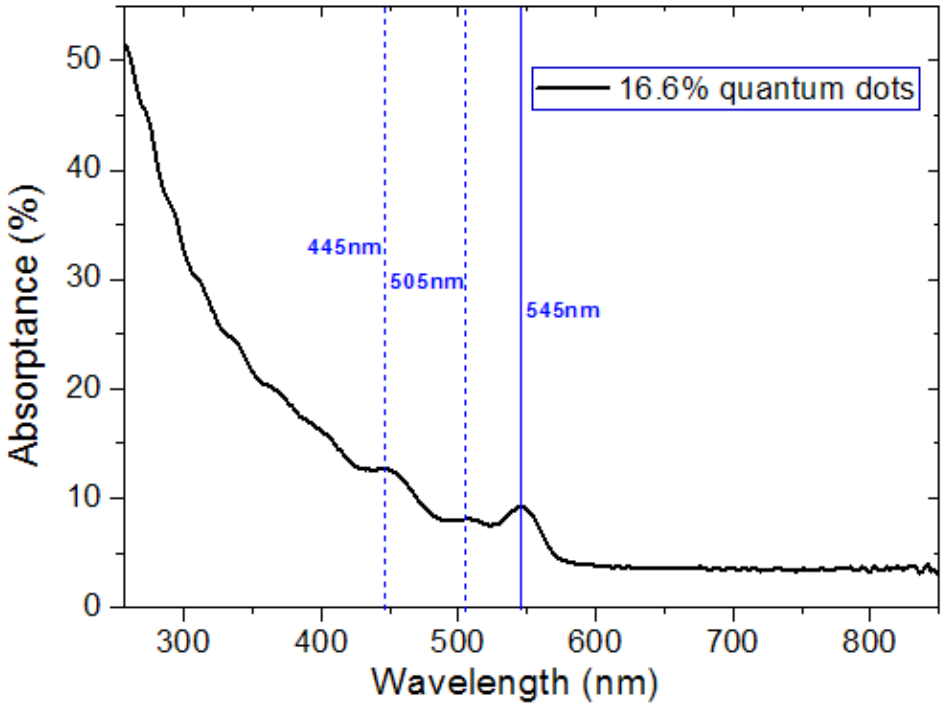

Figure 4.2.8: Absorption spectrum of 16.6 % CdSe/ZnS QDs measured at wavelengths ranging from 256 nm to 700 nm.

4.2.2 Photoluminescence versus wavelengths measurement:

In order to compare the absorption peaks with the emission peaks, luminescence measurements were performed on PMMA films with the three weight ratio percentages of CdSe/ZnS QDs (4.2 %, 8.3 % and 16.6 %). Since the ZnS shell can eliminate the dangling bonds at the CdSe core surface, this shell strongly reduces non-radiative recombination and thereby increases the luminescence efficiency of the QDs [27].

The light source for the luminescence measurements was an Ar^+ laser emitting at 514.53 nm. Measurements were performed using a Horiba Labram HR800 spectrometer with backscattering geometry. The laser beam (typical laser power: 0.3 μW) was focused on the sample through a 50X objective. The locations of the emission peaks for all weight ratio percentages of QDs were grouped closely around the wavelength of 560 nm. In particular these emissions also agree with what is expected when the QDs were first dissolved in solvent as shown in Figure 4.2.9. This indicates that the PMMA is quite stable without changing the optical properties of QDs. The photoluminescence spectrum was found to be Stokes-shifted from the first exciton [95] absorption peak at 545 nm by around 15 nm. As for the absorption spectra a weak red-shift of the luminescence peak is observed with increasing QDs percentage as shown in the following discussions. In addition, the emission intensity increases almost linearly with respect to the weight ratio percentage of the QDs.

All of the emission curves in these samples can fit well with Gaussian curves but not with Lorentzian curves, indicating inhomogeneous band broadening phenomena. This can be seen in Figure 4.2.10 to Figure 4.2.12 corresponding to weight ratio percentages 4.2 % to 16.6 % of CdSe/ZnS QDs. Such band broadenings can certainly be attributed to a size dispersion effect. The full width

at half maximum (FWHM) of the luminescent bands is around 23 nm for all samples, indicating that the QDs size variations are less than 5 % and that we have almost the same extent of size variation for each sample. At first we can observe two phenomena. In the emission curve a small modulation near the center peak is a measurement artifact. The emission spectrum is slightly asymmetrical, especially for the highest QDs weight ratio percentage of 16.6 %.

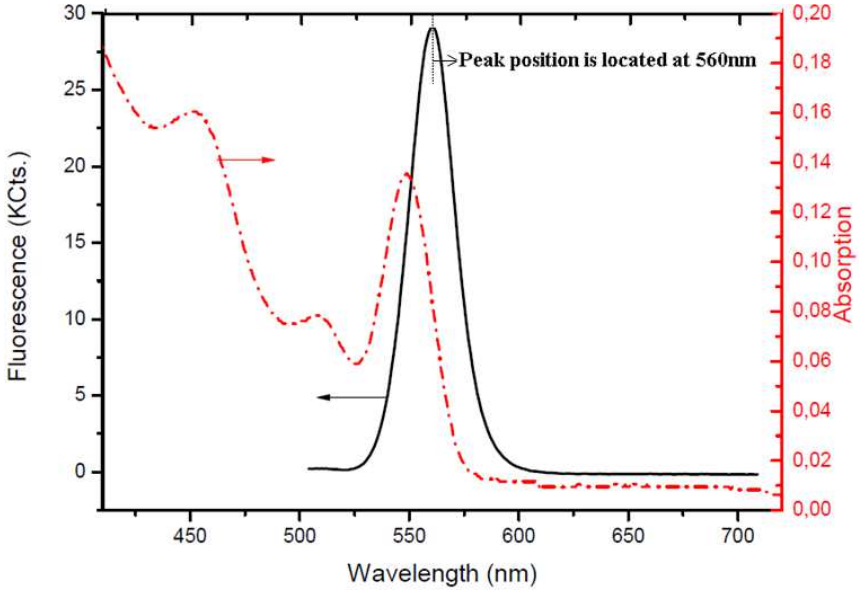

Figure 4.2.9: Photoluminescence (solid) and absorption (dotted) spectra of CdSe/ZnS QD in chloroform provided from PlasmaChem GmbH.

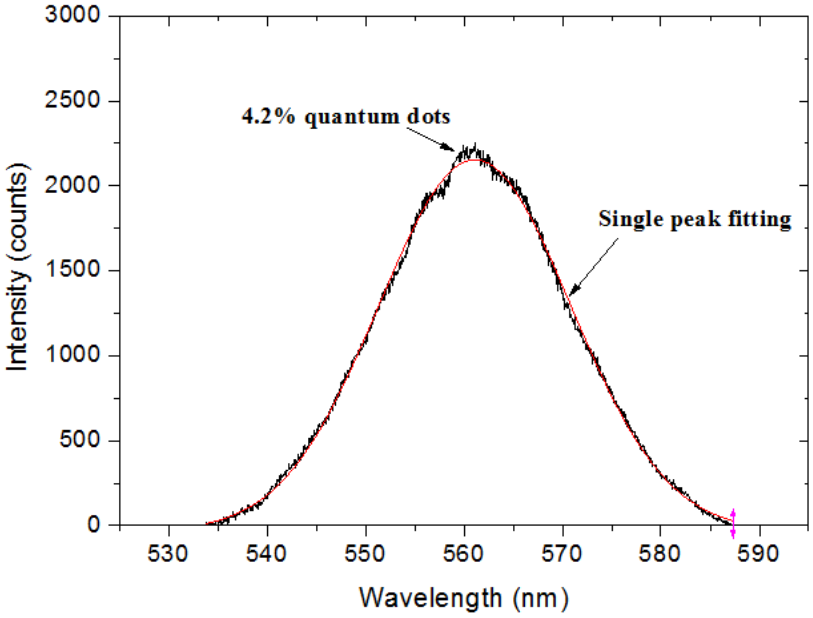

Figure 4.2.10: Luminescence of weight ratio percentage 4.2 % CdSe/ZnS QDs.

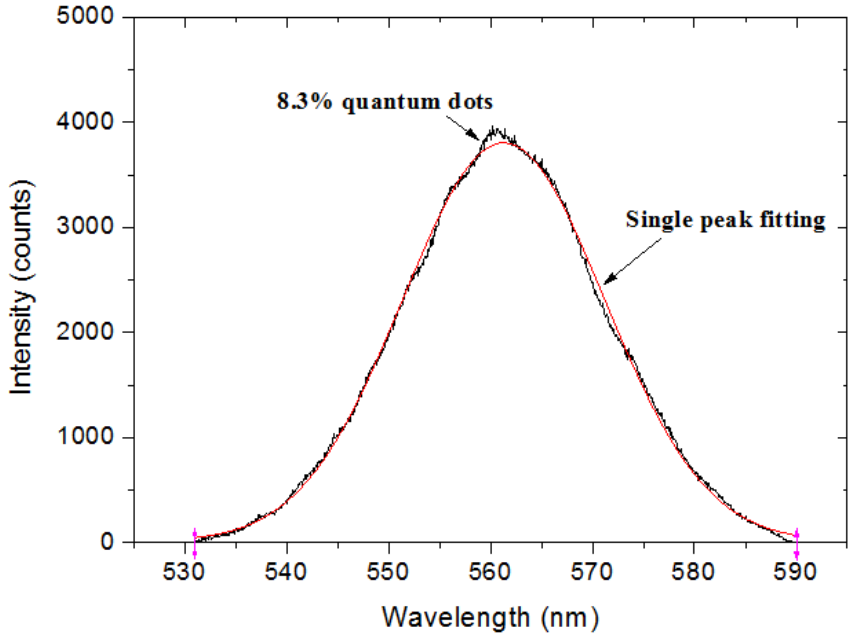

Figure 4.2.11: Luminescence of weight ratio percentage 8.3 % CdSe/ZnS QDs.

As shown in Figure 4.2.12, the emission intensity is slightly raised at longer wavelengths, while decreasing slightly at shorter wavelengths of around 540 nm. Regarding the origination of the asymmetry photoluminescence spectrum, two explanations could be considered. One could be the overlapping area between the PL and absorption spectra, which results in self-absorption phenomena, i.e., part of the emission was absorbed by itself, which thus decreases the PL intensity at short wavelengths [96]. Another possible explanation could be caused by the excitation energy transfer from small QDs to large ones through tunneling effects, and as a result, the PL intensity at long wavelengths is higher than that of shorter wavelengths [97].

All the results from Gaussian curve fitting, such as the centering wavelength of the emission peak, the wavelength shift and the FWHM of the peak, are listed in Table 2. When comparing all emission curves corresponding to different QDs weight ratio percentages, the red-shift of the emission peaks were increased with increasing percentages, as shown in Figure 4.2.13 and Table 2. This could be attributed to a QDs coupling phenomenon.

Finally, we conclude that the PMMA polymer can be utilized as a good hosting material, which is transparent in the whole visible spectrum, to study the intrinsic absorption and luminescence of QDs embedded in a thin film.

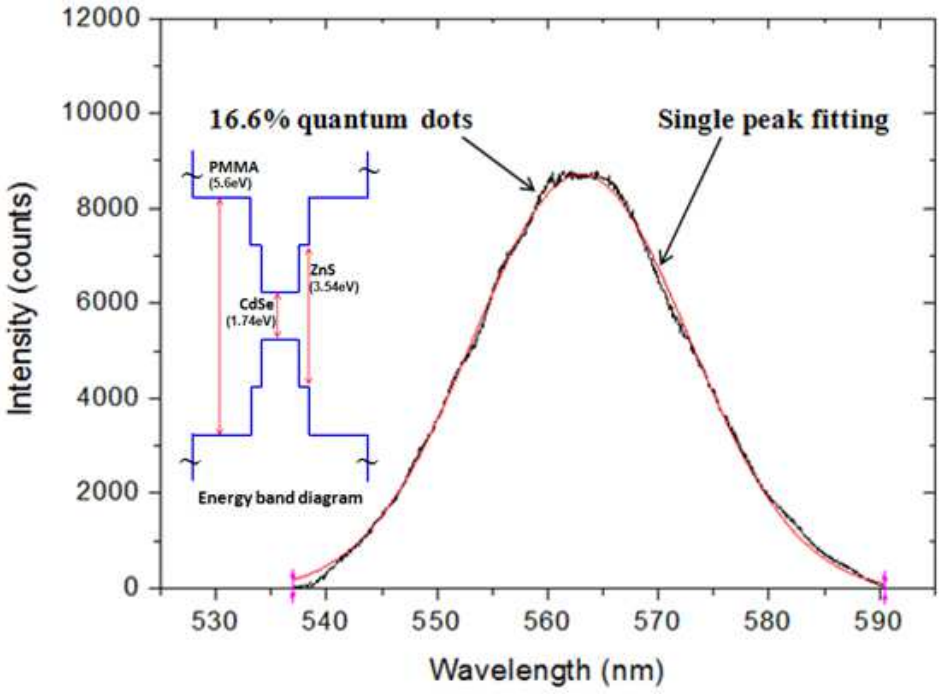

Figure 4.2.12: Luminescence of weight ratio percentage 16.6 % CdSe/ZnS QDs.

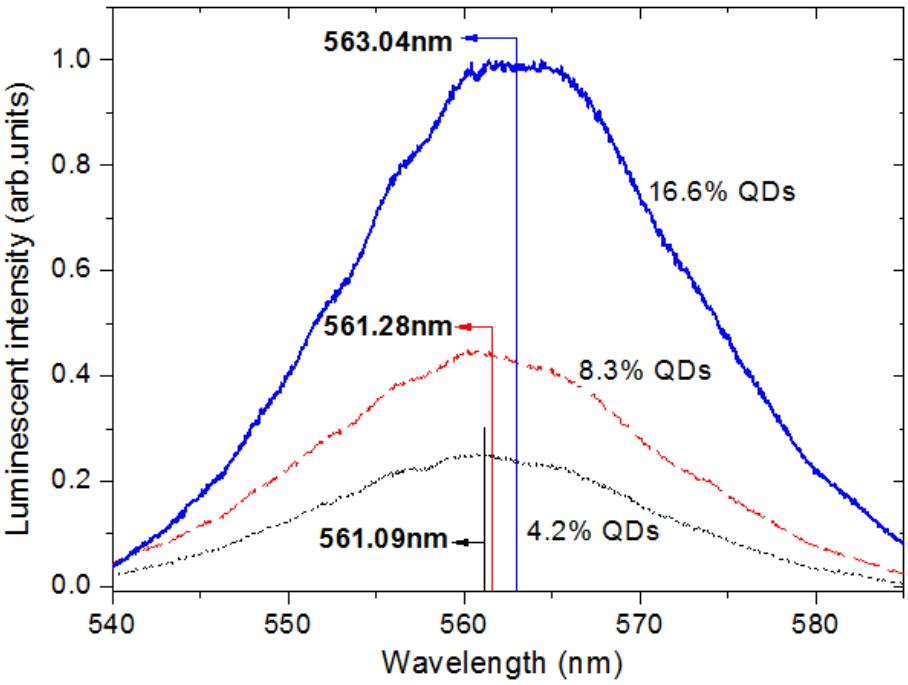

Figure 4.2.13: Luminescence measurements of PMMA layers with different weight ratio percentage CdSe/ZnS QDs: 4.2 %, 8.3 % and 16.6 %.

Table 2. Center wavelengths, shifting of the wavelength from 560 nm and FWHM of the photoluminescence spectra obtained with PMMA layers containing w.r.4.2%, w.r. 8.3% and w.r. 16.6% QDs.

Samples	Centering wavelength (nm)	Shifting wavelength from the 560nm (nm)	FWHM (nm)
4.2% QDs	561.1± 0.04	1.1± 0.04	23.0± 0.3
8.3% QDs	561.3± 0.04	1.3± 0.04	23.0± 0.3
16.6% QDs	563.0± 0.04	3.0± 0.04	23.0± 0.3

4.2.3 Photoluminescence intensity versus time measurement:

In order to verify the coupling effect between quantum dots, we extended the laser illumination process and also recorded the variation of photoluminescence with time with a second (sec) resolution. In our hypothesis, we expected there to be a stronger coupling effect with higher QDs concentration when applying continuous laser pumping. Hence, the coupling induced red-shift (r.s.) emission peaks should remain as 16.6 % QDs $_{(r.s.)}$ > 8.3 % QDs $_{(r.s.)}$> 4.2 % QDs $_{(r.s.)}$.

In our experiments we used an Ar^{+} laser emitting at 514.5 nm with a laser power of 0.3 μW. Other equipment and conditions were all the same as the previous experiment in section of 4.2.3. As shown in Figure 4.2.14, the spectrometer started to record the average intensity of photoluminescence after ~5 sec of laser pre-illumination. An interesting continuous enhancement of emission intensity (int.) from the QDs with time was discovered.

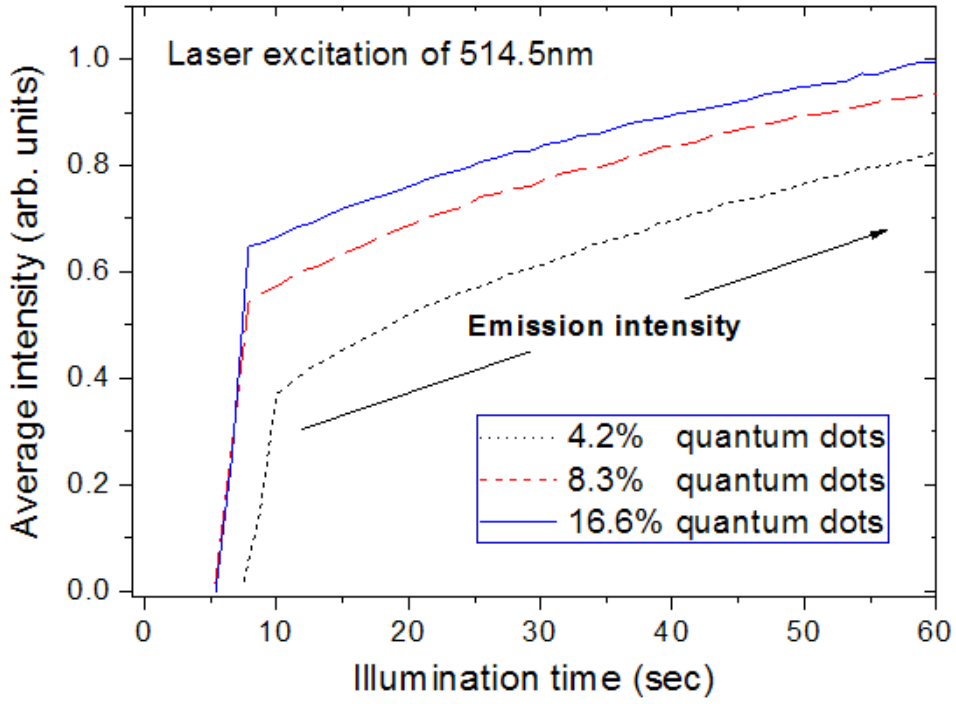

Figure 4.2.14: Different weight ratio percentage QDs continuously excited by laser for 60 seconds showing an enhancement of emission intensity.

In Figure 4.2.14, the stronger emission intensity was provided by higher QDs concentrations. Even though the laser illumination time was extended to 60 sec, this relationship was still maintained in a similar state as the initial situation where 16.6 % QDs $_{(int.)}$ > 8.3 % QDs $_{(int.)}$ > 4.2 % QDs $_{(int.)}$.

In the next step, the laser illumination time was prolonged by more than 60 sec in order to verify whether the intensity could be saturated or not. After a long illumination time, the emission intensity of the QDs was surprisingly still enhanced even when the laser illumination time was already as long as 1910 sec (> 30 minutes). Such emission enhancements occurred for all samples including different weight ratio percentages of 4.2 %, 8.3 % and 16.6 % QDs as shown in Figure 4.2.15, Figure 4.2.16 and Figure 4.2.17 respectively. For comparison, all of the photoluminescence intensities were normalized. These figures indicated that the emission intensity at 1910 sec could even be increased four-fold over the emission intensity at 5 sec.

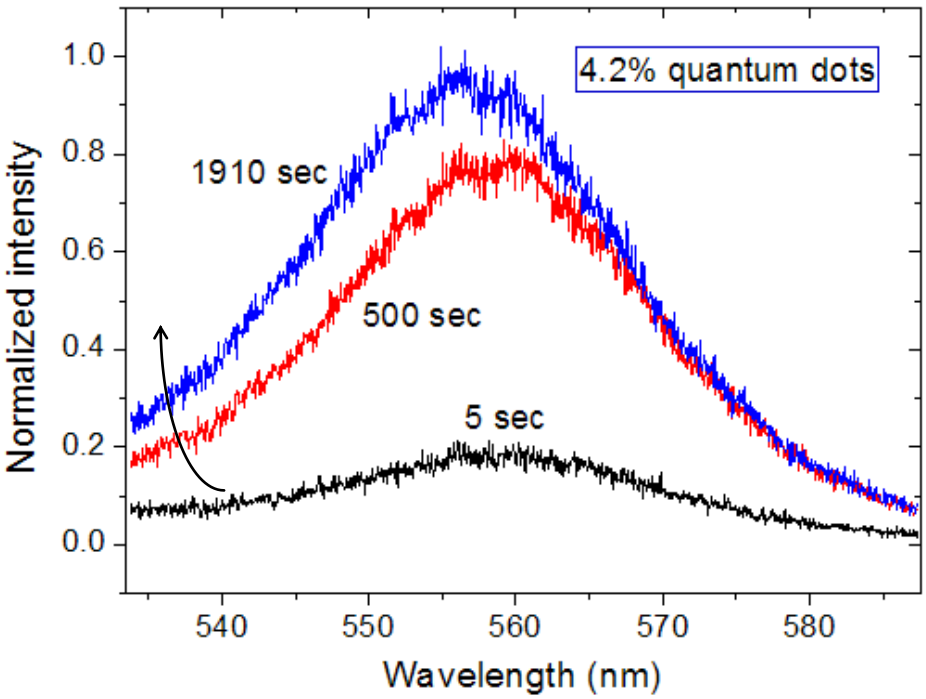

Figure 4.2.15: Weight ratio percentage 4.2% QDs continuously excited by a laser for 1910 seconds (sec) showing an enhancement of emission intensity.

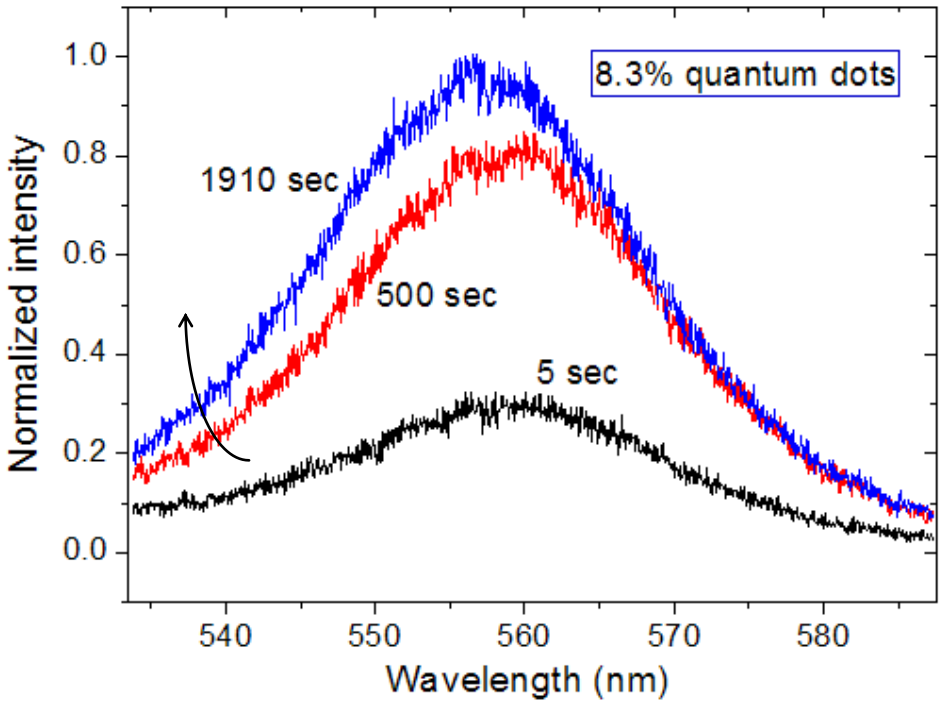

Figure 4.2.16: Weight ratio percentage 8.3% QDs continuously excited by a laser for 1910 seconds showing an enhancement of emission intensity.

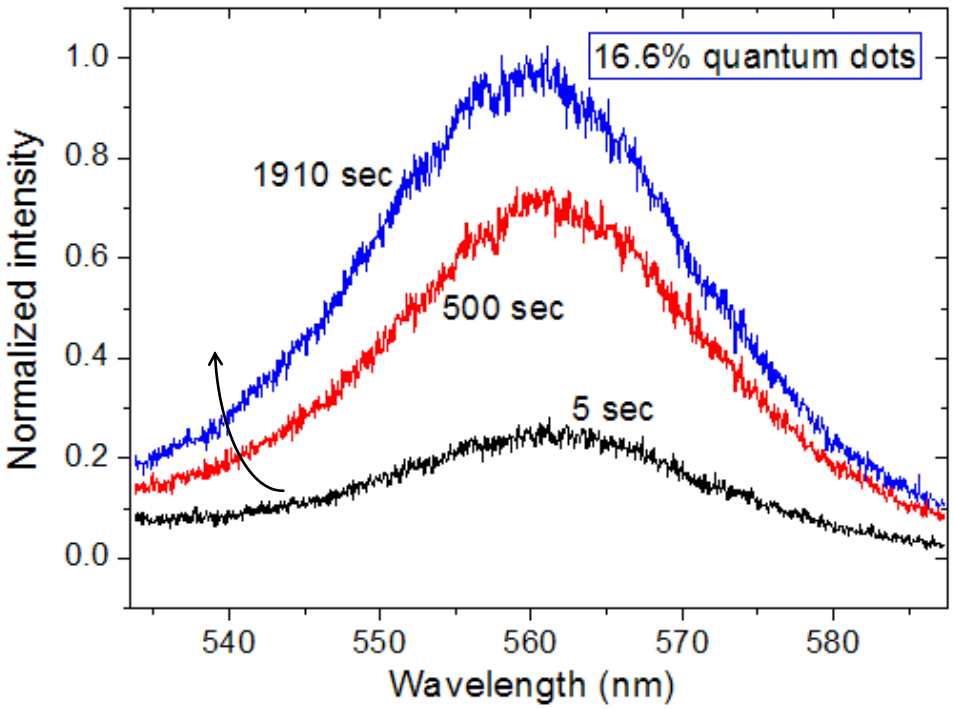

Figure 4.2.17: Weight ratio percentage (w.r.) 16.6% QDs continuously excited by a laser for 1910 seconds showing an enhancement of emission intensity.

A similar phenomenon of photo-induced photoluminescence enhancement was mentioned in the close-packed films of CdSe QDs covered with ZnS film [98]. Another group proposed and verified that the QDs photoluminescence (PL) enhancement could be attributed to a light induced increase of the potential barrier for electron–hole escaping from QD levels [99]. Therefore, the carrier trappings may lead to the appearance or neutralization of the local electric field or exhibit Auger recombination leading to PL reduction [98]. The trap recharging may cause an increase of the potential barrier height for carriers to be released from the QD levels, which would enhance PL output [99]. However, they gave interpretations for the enhanced PL output, but they did not find the blue-shift in the PL peaks or FWHM variations as in our study.

We investigated the PL characteristics via laser illumination. These emission curves were found to fit the Gaussian distribution well, as mentioned in the previous section. Hence the central peak position and the FWHM of all emission curves could be analyzed. All information was compared as discussed below.

As shown in Figure 4.2.18, emission peaks clearly revealed a blue-shift which became larger and larger with progressively longer laser excitation times. Look at the 4.2 % QDs for example. The emission peak blue shifting was found to be 0.75 nm when compared to illumination at 500 sec and the initial illumination situation at 5 sec. There was a significant increase in the amount of blue-shifting to 2.72 nm when the laser illumination was maintained for 1910 sec. As in Ref [99], it was proposed that a light-induced increase of the potential barrier could confine more carriers in order to accumulate to a higher energy level and generate radiative recombination. Thus this is possible cause of the blue-shift. On the other hand, the decreased blue-shifting means that the red-shifting was revealed when compared to higher w.r. QDs. The results verified our original

hypothesis that the coupling effect can be enhanced by increasing w.r. QDs. As shown in Figure 4.2.19, the FWHM with increased curves showed the same trend as the initial FWHM of 23 nm. These will be discussed in next experiment.

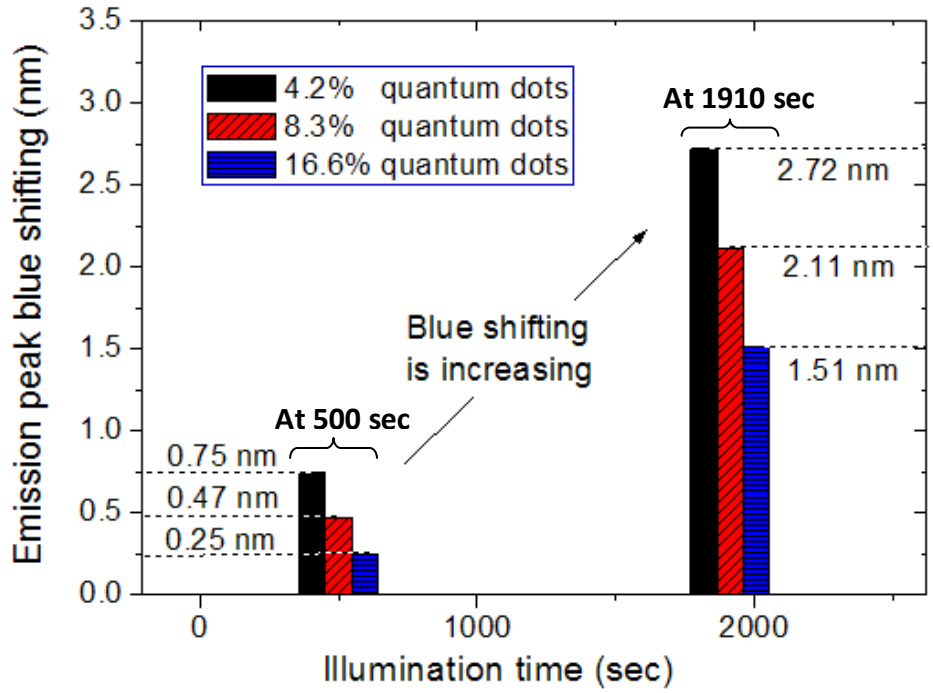

Figure 4.2.18: Emission peaks blue shifted from the first time emission peak caused by continuous laser excitation.

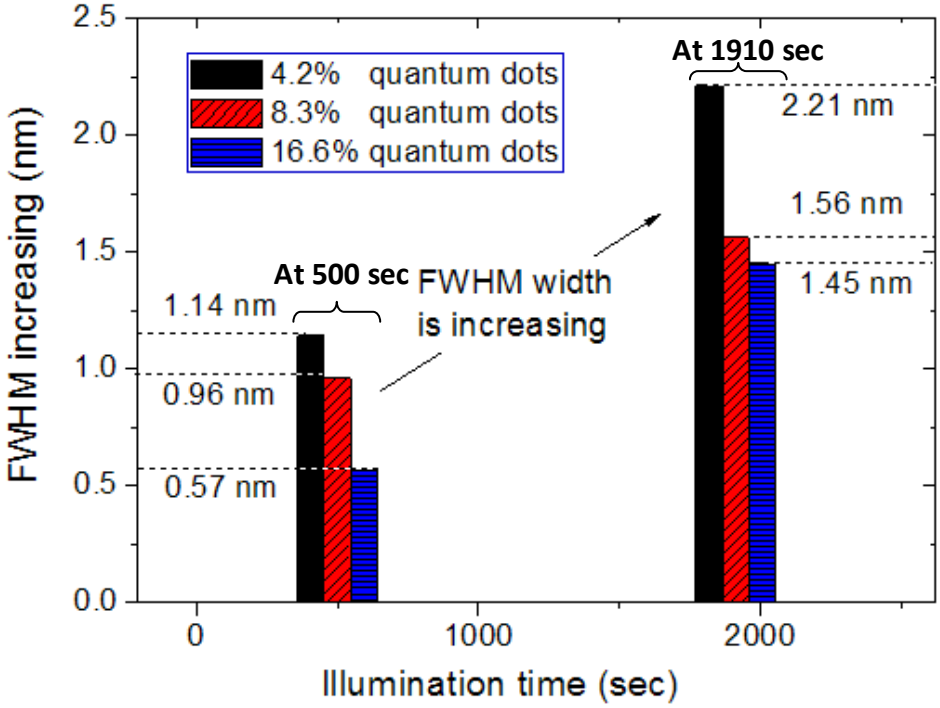

Figure 4.2.19: Emission peaks FWHM increasing from the first time emission peak caused by continuous laser excitation.

To understand the coupling between QDs, an illustration is discussed. If there is a small enough distance between the QDs, their electron/hole wave functions will overlap and the QDs will be coupled together, as shown in Figure 4.2.20. Hence, the higher energy excitation (Eg_2) could possibly be transferred to the neighboring dot (Eg_1). When considering a denser QDs group, as shown in Figure 4.2.21, this coupling induced energy transfers to the surrounding dots with lower energy gaps. In this figure, the original high energy carrier (1) would transfer to (2) and then transfer to (3) until reaching the lowest energy gap (4) for radiative recombination. This could be the mechanism for the red-shift phenomenon observed in our study.

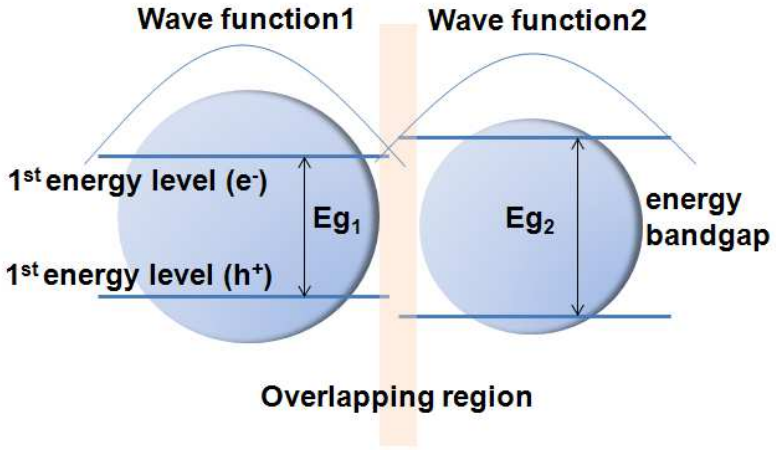

Figure 4.2.20: A coupling effect occurring between quantum dots.

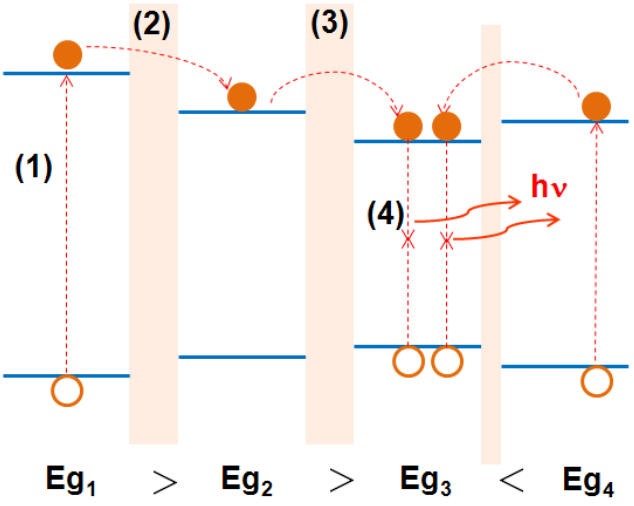

Figure 4.2.21: The energy transference induced by the coupling effect.

To verify the luminescent enhancement, the laser output power was modulated to a higher power of 3 mW, which was 4 orders of magnitude larger than that in the previous experiment. The laser excitation wavelength was applied at 514 nm and the total illumination time was kept the same, at 1910 sec. In Figure 4.2.22, the PL average intensity of w.r. 4.2 % QDs was studied as a function of illumination time via continuous laser excitation. As shown in this figure, the emission intensity saturated quickly and then decayed until reaching the 1910 sec mark when continuously supporting the high power laser. In order to characterize these luminescence spectrum variations, the emission curves of w.r. 4.2 % QDs at 5 sec, 200 sec (turning point), 1000 sec and 1910 sec illumination times were recorded and compared in Figure 4.2.23 separately. As can be seen, the luminescent peak intensity at 200 sec was 3~4 times larger than the first intensity at 5 sec. The decreased trend drives the luminescent peak intensity at 1910 sec to be ~0.7 times smaller than the intensity at 200 sec. In regards to this phenomenon, we propose that it could be mainly caused by thermally induced luminescence quenching [100] because luminescence efficiencies are strongly temperature-dependent [101]. Even though enormous high energy in the photons from the laser could induce a strong luminescence from QDs, however, a thermal effect also accompanies the process. This thermal effect accumulates with time and could bring out an increased exciton-phonon coupling effect [100], which resulted in quenching PL intensity.

A similar phenomenon for PL intensity variation can be observed in Figure 4.2.24 while using a higher weight ratio percentage of 8.3 % QDs. A comparison of PL emission peaks for four different illumination times of 5 sec, 500 sec (turning point), 1250 sec and 1910 sec is shown in Figure 4.2.25. The results show a similar quenching PL intensity due to overexposure by laser. In addition,

the PL intensity decay rate of w.r. 4.2 % was faster than the w.r. 8.3 % possibly caused by the increased trapping centers when the exciton-phonon coupling effect occurred.

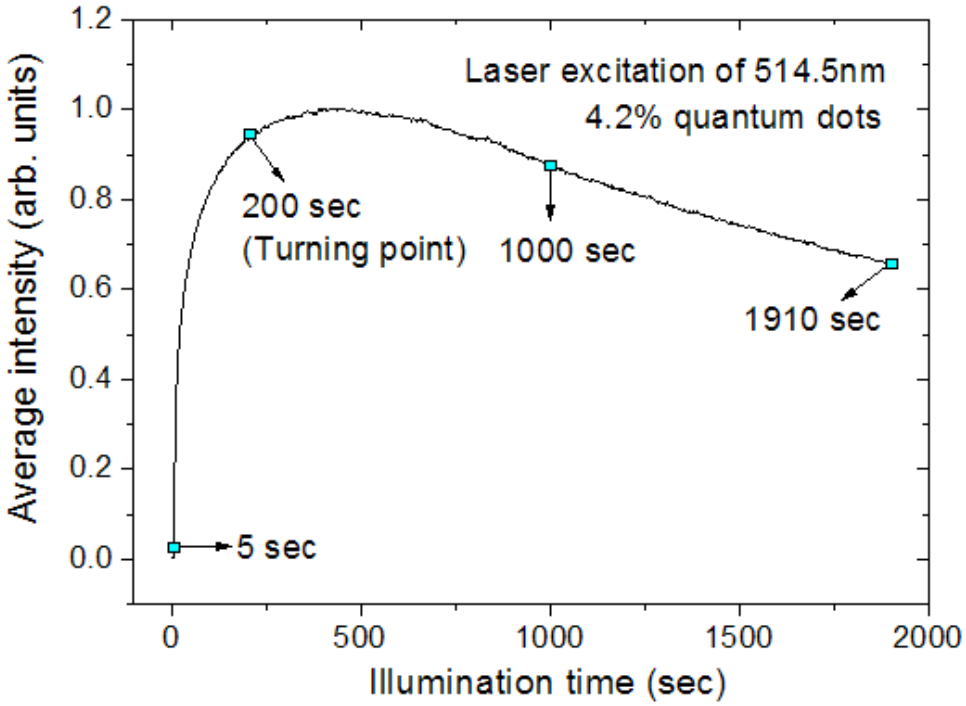

Figure 4.2.22: A 3 mW power laser excitation on w.r. 4.2% QDs induced a quick saturation and even a decay of emission intensity for 1910 seconds.

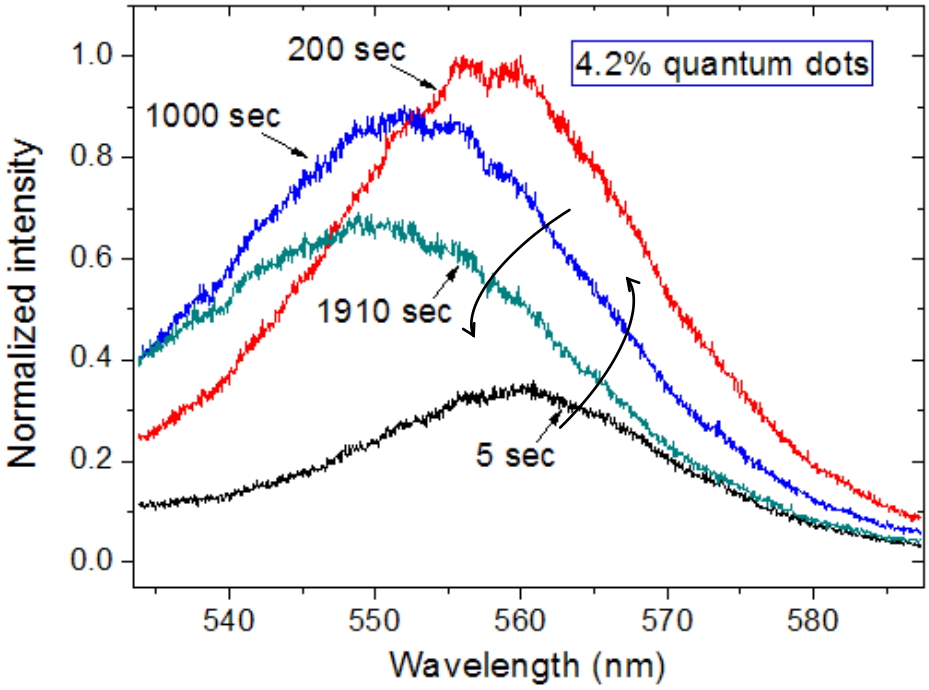

Figure 4.2.23: A 3 mW power laser excitation on w.r. 4.2% QDs showing a quick increase and a decay of emission intensity.

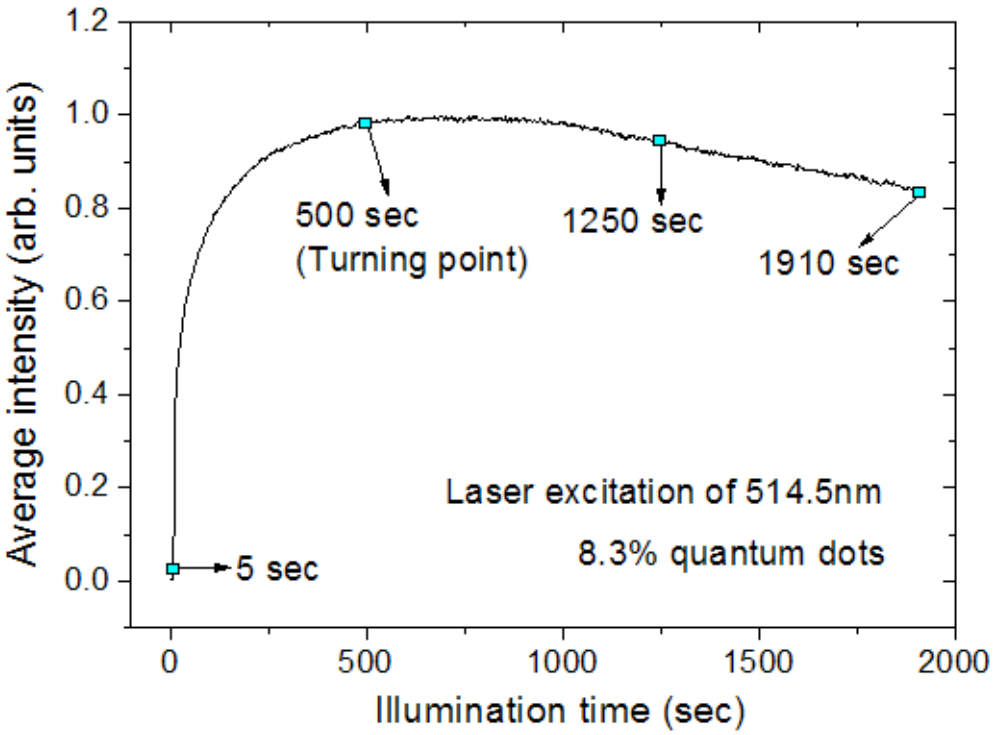

Figure 4.2.24: A 3 mW power laser excitation on w.r. 8.3% QDs induced a quick satu- ration and even a decay of emission intensity for 1910 seconds.

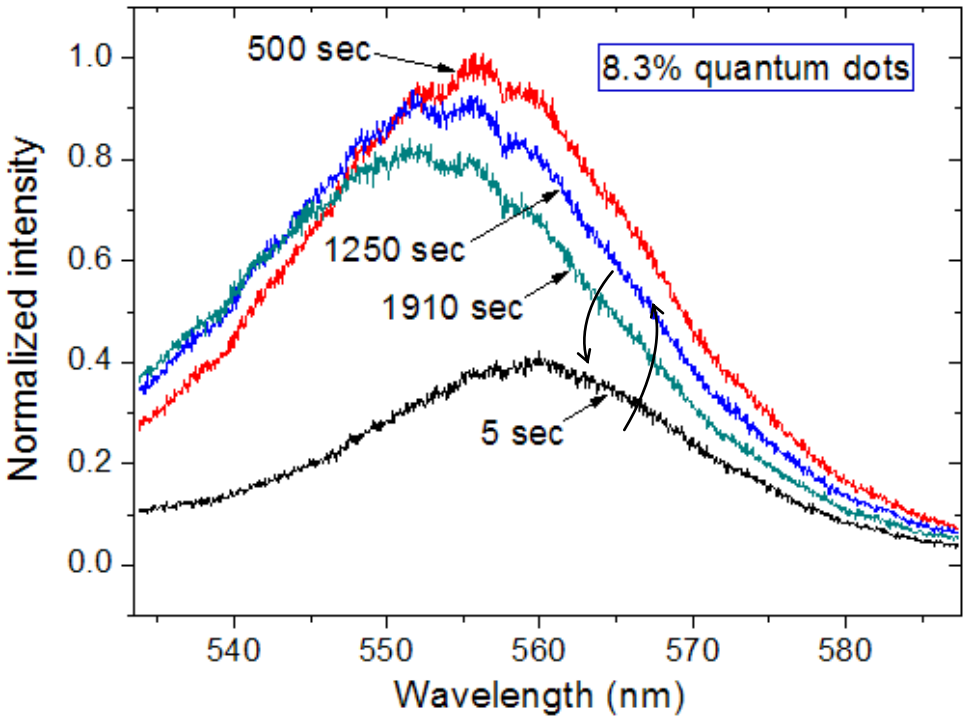

Figure 4.2.25: A 3 mW power laser excitation on w.r. 8.3% QDs showing the quick increase and the decay of emission intensity.

By applying Gaussian curve fitting to the luminescence spectrum, the central peak positions and FWHM could be determined. As can be seen in Figure 4.2.26, both the phenomena of blue shifting and FWHM expansion still happened to w.r. 4.2 % QDs, but the effect was found to be dramatically enhanced. A comparison of Figure 4.2.18 and Figure 4.2.19, with w.r. 4.2 % QDs at illumination time of 1910 sec, shows that the emission peak blue shifted and the FWHM increased by only 2.72 nm and 2.21 nm, respectively. However, both increased strongly when undergoing higher power laser illumination with a blue shift of ~9 nm and an increased FWHM of ~5.5 nm, as shown in Figure 4.2.26. Concerning the w.r. 8.3 % QDs, similar results were also discovered. In addition, both the reduced blue shift and FWHM increase still happened with the higher w.r. QDs, even when using higher power laser, as shown in Figure 4.2.26 and 4.2.27. The blue shift with the w.r. 8.3 % QDs (~7.2 nm) was smaller than that of the w.r. 4.2 % QDs (~9 nm) at the illumination time of 1910 sec, indicating that the red shift occurred while increasing the w.r. QDs. The FWHM increase for the w.r. 8.3 % QDs was also smaller than that for the w.r. 4.2 % QDs at the same illumination time of 1910 sec. Another interesting discovery was that the increasing blue shift could be well fitted by an exponential function and the FWHM variation as well. This may be linked with the carrier lifetime in QDs and carrier generation rates which are still under investigation.

As mentioned, the PL intensity decay rate in Figure 4.2.22 and Figure 4.2.24, the lifetime of w.r. 8.3 % QDs was longer than w.r. 4.2 % QDs, indicating that a reduced phonon effect happened with higher w.r. QDs. We propose that this phenomenon could be caused by phonon release from the condensed QDs. Another proof of this hypothesis is that the FWHM widened, related to the exciton-phonon coupling effect. For both lower (0.3 μW) and higher power (3

mW) laser excitations, the FWHMs were all found to trend towards reducing expansion when increasing the w.r. QDs. This could be interpreted as due to the fact that the higher w.r. QDs could have reduced exciton-phonon coupling effect. This might be another proof for phonon release between dense QDs.

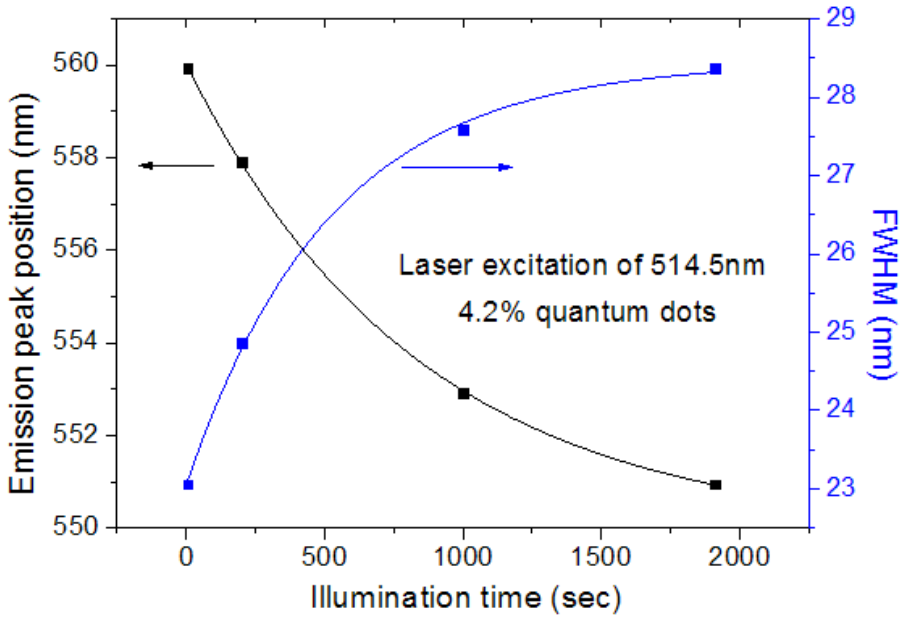

Figure 4.2.26: The emission peak is blue shifted and FWHM is widened with laser illumination time for w.r. 4.2% QDs.

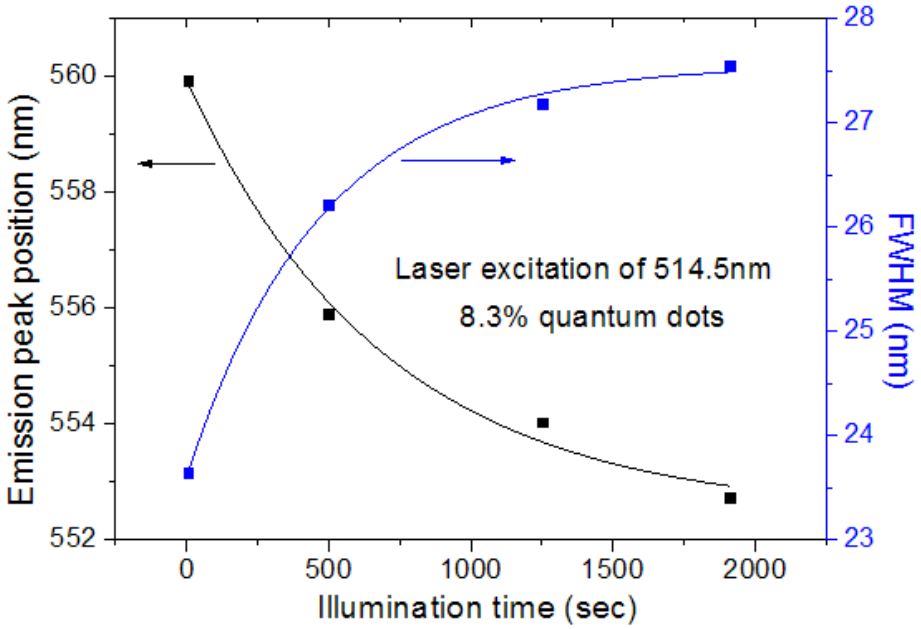

Figure 4.2.27: Emission peak is blue shifted and FWHM is widened with laser illumination times for w.r. 8.3% QDs.

4.3 Frequency conversion of CdSe/ZnS QDs: Its application to solar cells

4.3.1 Using PMMA /QDs films as down-conversion frequency layer:

Before applying hybrid QDs layers, it is important to understand that the response of photovoltaic solar cells depends on the efficient collection in the solar spectrum. Generally a large part of the solar spectrum is lost both in the infrared and in the UV range. It is estimated that the efficiency of bulk silicon solar cells could be increased by 32 % if the UV spectrum was used to create carriers [102]. In solar cell materials, UV photons generate hot electrons which would be thermalized by phonon coupling and most of them do not provide a photocurrent. More than that, they induce a temperature increase that will decrease the solar cell efficiency. In the case of organic materials, UV light can even break the molecular bonds and reduce the carrier lifetime in solar cells. A lot of studies have been focused on up-conversion and down-conversion processes to change IR and UV photons to have energy in the useful spectrum range [103]. Particular attention has been given to lanthanides materials [104] and, more recently, to quantum dots (QDs).

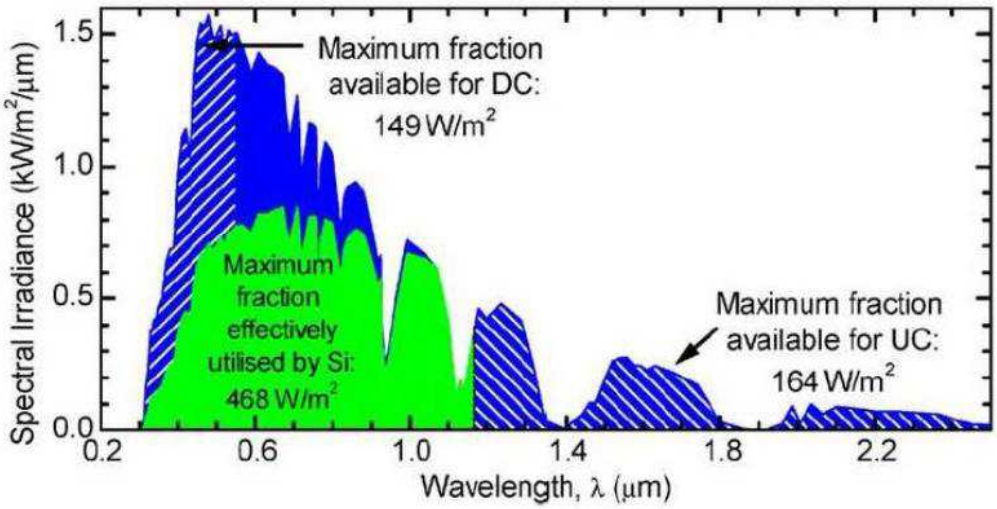

Figure 4.3.1: AM1.5G spectrum showing the fraction that is currently absorbed by a thick silicon device and the additional regions of the spectrum that can contribute towards up- and down-conversion [102].

The optical properties of the quantum dots naturally depend on their electronic properties [105]. Their absorption spectrum is therefore modulated by quantum confinement effects and, generally, they exhibit luminescence which can be excited by a wide range of wavelengths in their absorption spectrum. Consequently, the UV range of solar spectrum from wavelengths of around 300 nm is generally an efficient excitation source, as shown in Figure 4.3.1. It is estimated that an additional 1/3 of the conventionally used solar energy spectrum may be collected if the UV fraction is totally utilized through a frequency down-conversion process [102].

In our study, we focused on the possibility of converting UV photons into visible photons by using hybrid PMMA layers with CdSe/ZnS QDs, and performing calculations regarding the electromagnetic field distribution in the active layer of organic solar cell when they contain QDs.

To obtain homogeneous hybrid layers with functions of the down-conversion frequency effect, the spin coating method [106] is applied. The fabrication process is performed as described in section of 4.1.1. In order to achieve a stronger luminescence, we deposited a w.r. 16.6 % CdSe/ZnS QDs/PMMA hybrid layer and increased the thickness to around 2.49 μm. Its absorption and luminescent spectra are shown in Figure 4.3.2. The difference between the maximum of the first main absorption peak (located at ~545 nm) and the maximum of the luminescent peak (located at ~560 nm) is around 15 nm. This clearly shows that a down-conversion frequency effect can be obtained with such a layer. The frequency shift might be attributed to the Stokes effect [107] or induced by dark excitons [108].

In actual applications, we consider a frequency conversion component made of a transparent hybrid PMMA thin film containing QDs deposited on a silica

substrate located in front of a solar cell as illustrated in Figure 4.3.3. The aim is to collect the waste energy in the UV range which generally generates hot carriers [109]. The conversion layer collects the UV energy and converts it into a wavelength range where the active layer of the solar cell has higher absorption efficiency.

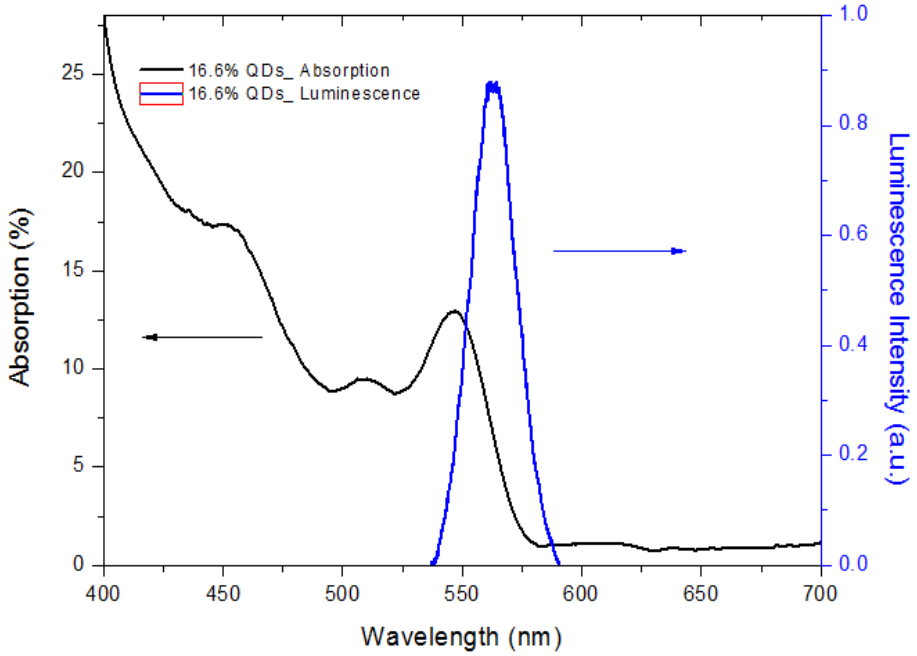

Figure 4.3.2: Absorption and photoluminescence spectra of a PMMA layer containing CdSe/ZnS QDs.

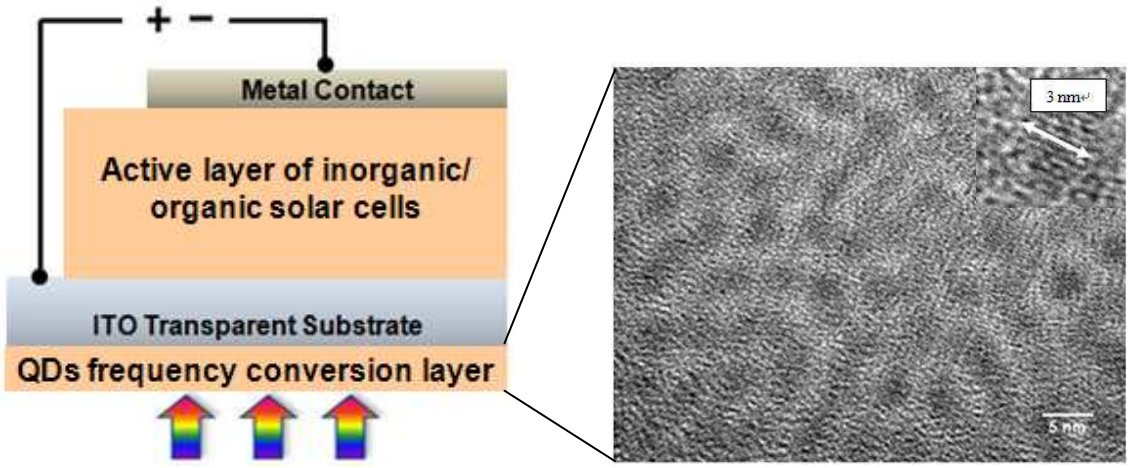

Figure 4.3.3: Illustration of solar cell device composed of CdSe/ZnS QDs frequency conversion layer (left figure) and TEM image of CdSe/ZnS QDs distribution (right figure).

To verify the frequency conversion effect, a silicon solar cell was used. We put a substrate coated with the hybrid QDs layer in front of it as seen in Figure 4.3.3 and measured the external quantum efficiencies (EQE) of the silicon solar cell. EQE is defined as the number of electrons generated divided by the incident photon number.

In order to calculate EQE correctly, we should consider how much light is transmitted though the QDs frequency conversion layer. Therefore, the measured EQE of the solar cell with the PMMA layer containing QDs should be divided by the transmission, T(λ), of the QDs conversion layer. This means that the light spectrum collected by the silicon solar cell is only from the extra photons generated by the luminescence of QDs conversion layer. As can be seen in Figure 4.3.4, luminescence increased EQE in the wavelength ranges shorter than 560 nm. This verifies an important fact where the new photons from the luminescence of QDs excited by wavelength range under 560 nm can be utilized by solar cells for creating new charges.

Figure 4.3.5 shows the EQE difference between the original solar cell and solar cell covered with this CdSe/ZnS QDs layer. It shows an interesting exciton feature as the modulation peaks from the EQE improvement are corresponding to different QDs absorption peaks at the first absorption peak (at 545 nm), the second absorption peak (at 508 nm) and the third absorption peak (at 450 nm). The first peak is stronger than the other two peaks because of the strong absorption from the QDs layer corresponds to the increased luminescence photons, thereby enhancing the EQE by the absorption peak at 545 nm. Meanwhile, this peak position is also quite close to the maximum optoelectronic response of the solar cell device. This can also contribute to the EQE spectrum.

In order to acquire a global improvement on Figure 4.3.5, we integrated the amount of EQE difference which gives a 21.5 % improvement in total. This indicates that the original short circuit current (Isc) of 2 mA might be raised to 2.43 mA in the final performance of the solar cell device.

However, the measured power conversion efficiency did not increase. This is because the absorption is stronger than the luminescence. This gives us an idea where efficiency could be increased if the absorption band was shifted to near UV. That could be achieved in a future work by using QDs with smaller sizes or other compositions.

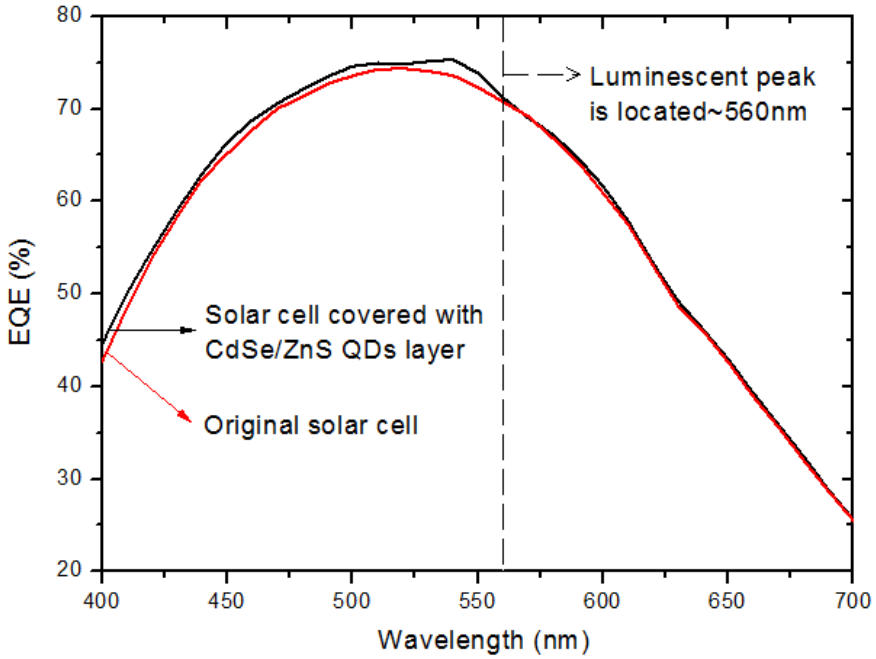

Figure 4.3.4: Measured external quantum efficiencies of silicon solar cells with and without a glass coated with a PMMA layer contained CdSe/ZnS QDs. In this last case, the EQE has been divided by T(λ) of the QDs layer.

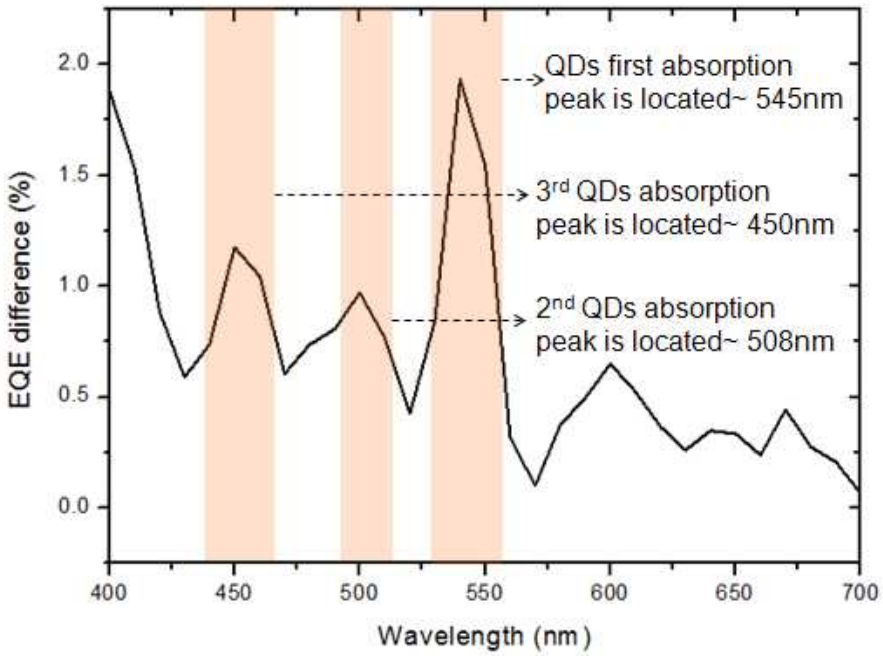

Figure 4.3.5: EQE difference between original solar cell and that covered by the QDs layer showing the exciton features are related to different QDs absorption peaks.

4.3.2. QDs embedded in the active layer of organic solar cells:

Another interesting configuration is to embed the QDs directly in the active layer of the solar cell device so that the down-conversion takes place inside the cell (Figure 4.3.6(b)). It is well known that the inclusion of metallic nanoparticles in the active layer has a strong effect on the electromagnetic field distribution [110]. It is thus interesting to calculate the electromagnetic field distribution when the QDs are embedded in the active layer to check if the photons from luminescence are better captured. For example, we consider CdSe QDs in an active layer, P3HT/PCBM, of an organic solar cell (OSC) [111].

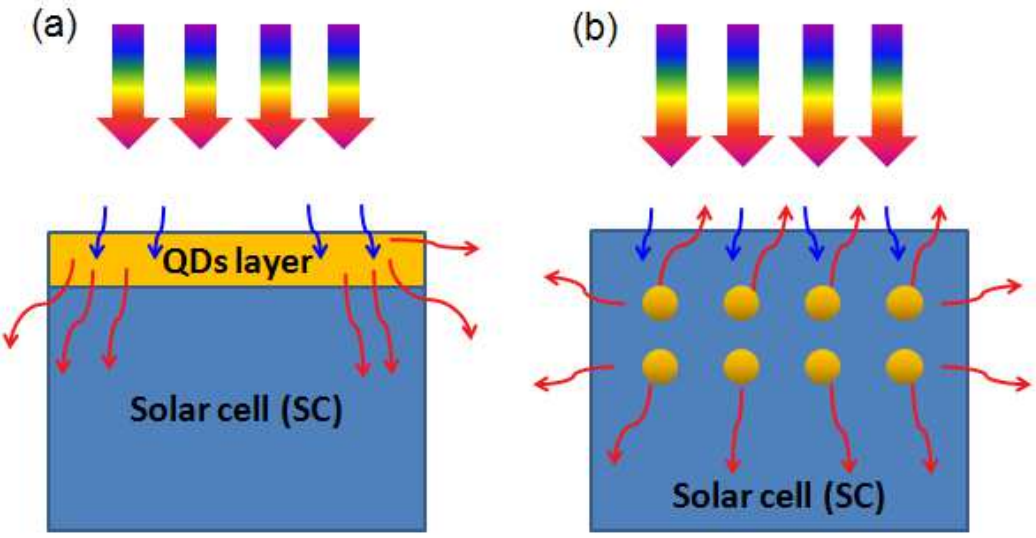

Figure 4.3.6(a): Solar cell has a covered QDs layer for down-conversion frequency.
(b): Solar cell has QDs inclusion in its active layer

The Finite Difference Time Domain (FDTD) method [112] was applied to calculate the electromagnetic field distribution in the P3HT/PCBM active layer of an OSC. We assumed the 3 nm CdSe nanoparticles (NPs) to have a periodic distribution. Figure 4.3.7 shows the nanoparticle distributions considered and the corresponding electric field distribution in the layer. The incident light is a polychromatic plane wave polarized along the x-axis. The distance between the NPs is of 1 nm or of 3 nm. As the thickness of the shell layer in CdSe/ZnS QDs is only of a few angstroms, it has been ignored in this calculation.

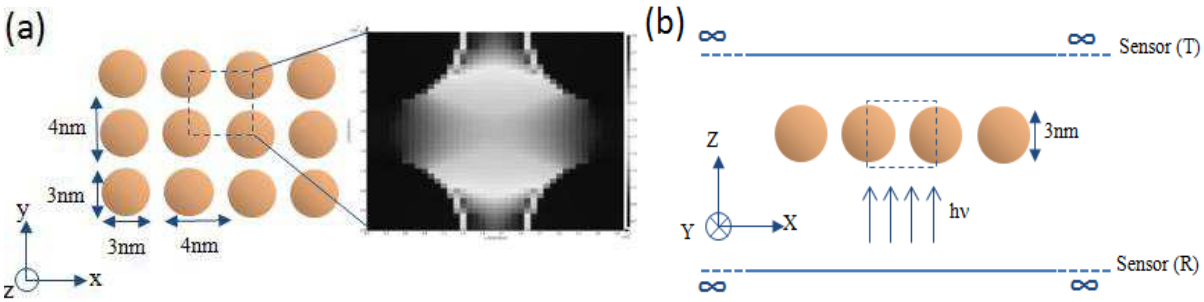

Figure 4.3.7: Model used for FDTD calculations. CdSe nanoparticles of 3 nm in diameter are embedded into a P3HT/PCBM layer: (a) top view and (b) side view.

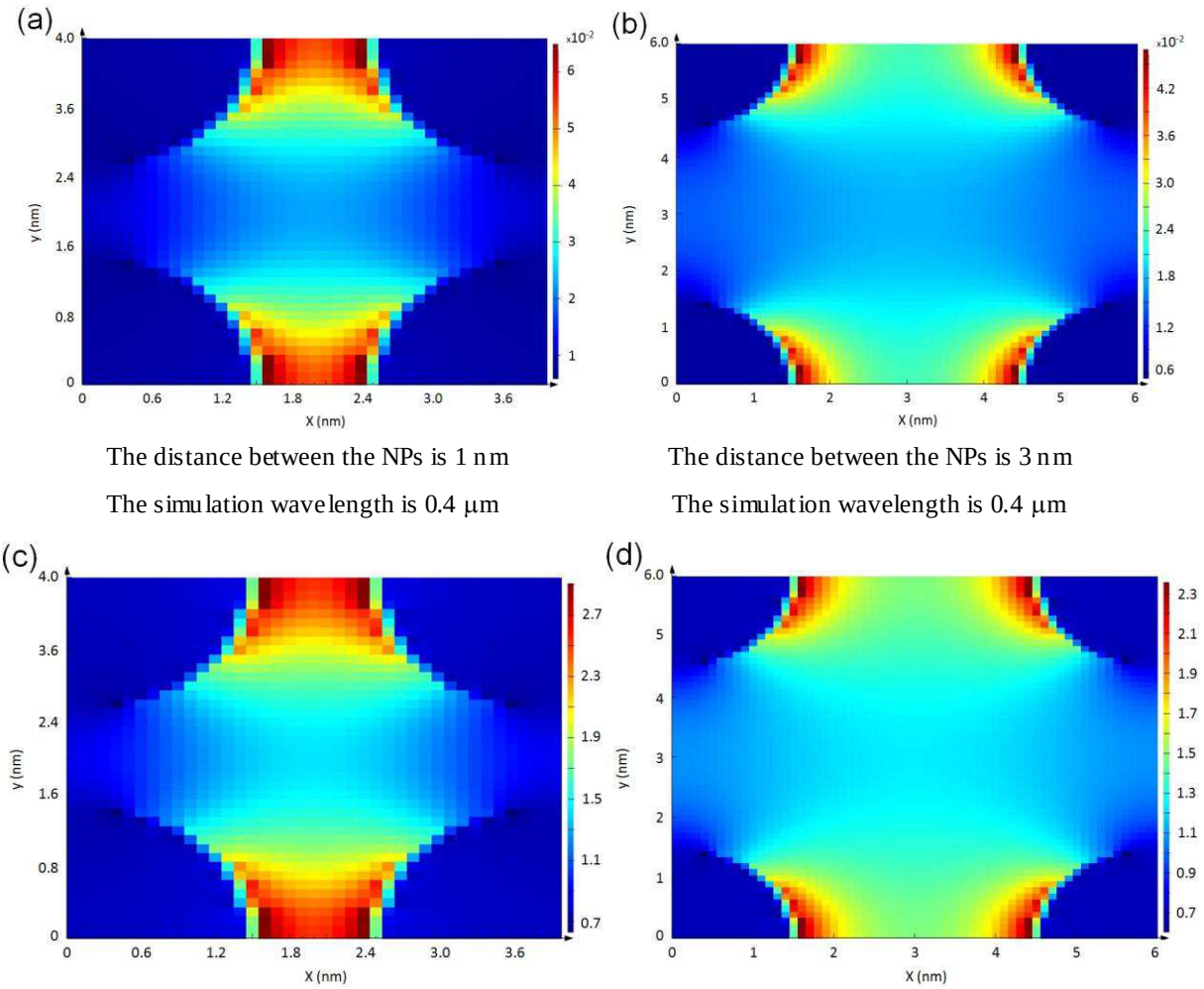

The distance between the NPs is 1 nm
The simulation wavelength is 0.4 µm

The distance between the NPs is 3 nm
The simulation wavelength is 0.4 µm

The distance between the NPs is 1 nm
The simulation wavelength is 1 µm

The distance between the NPs is 3 nm
The simulation wavelength is 1 µm

Figure 4.3.8: Electric field distributions in the X-Y plane for two incident wavelengths and two different distances between the nanoparticles (NPs).

A comparison of the electric field distributions in the X–Y plane is shown in Figure 4.3.8 considering two incident wavelengths, 0.4 µm and 1 µm, and two different distances, 1 nm and 3 nm, between the NPs. We found the field enhancement surrounding the NPs is stronger when they are closer to each other. This means that the enhancement is stronger for a distance of 1 nm than that for 3 nm (~1.4 times at a wavelength of 400 nm). Furthermore, the electric field is stronger for the incident wavelength of 1 µm than of 0.4 µm. The electric field distributions in the X–Z plane were also calculated for the two different incident

wavelengths with the same distance of 1 nm between the NPs as shown in Figure 4.3.9. From the electric field profile in X-direction for the two incident wavelengths, the electric field is found to be 45 times greater for 1 µm than for 0.4 µm as shown in Figure 4.3.10. It is important to note that the geometrical dimensions considered here are much smaller than the calculation wavelengths and also much smaller than in [113] and [114]. Even so, strong field enhancements are obtained. These could be combined with the effect of down-conversion and applied to OPVs containing QDs.

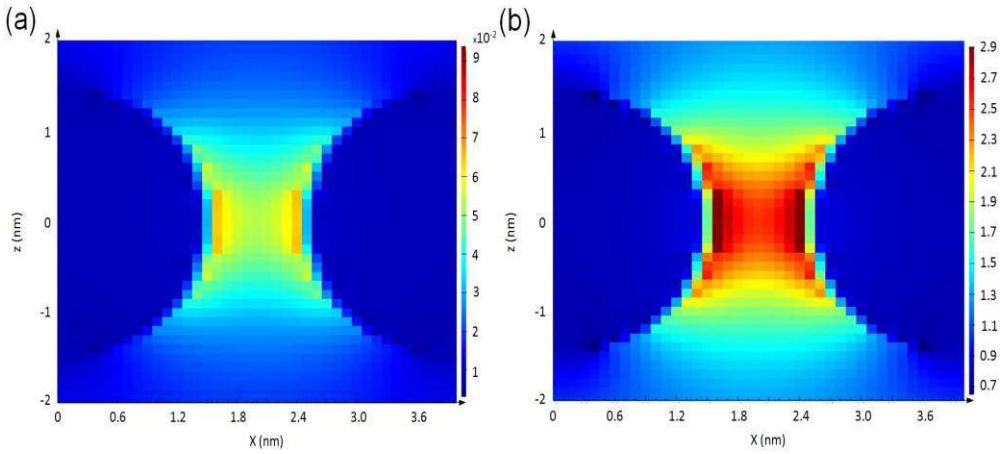

Figure 4.3.9: Electric field distributions are in the X-Z plane for distance of 1 nm between the NPs for two incident wavelengths: (a) 0.4 µm (b) 1 µm.

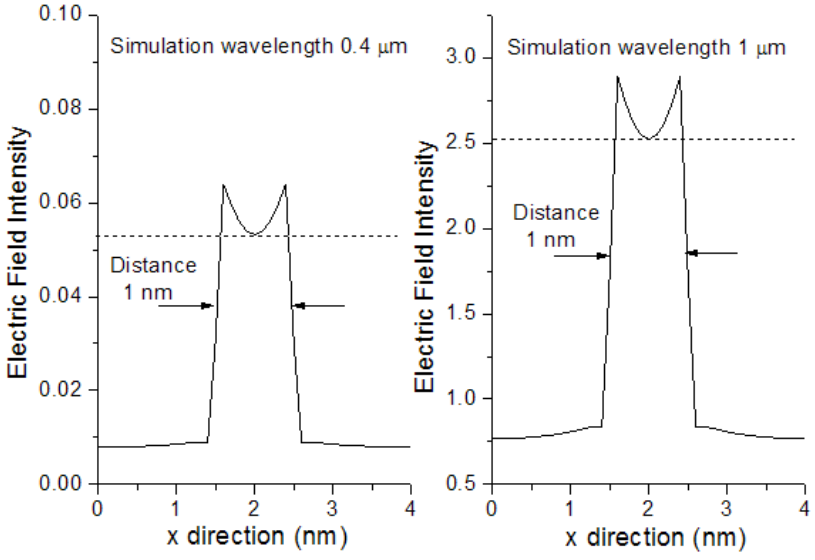

Figure 4.3.10: Electric field profiles in X-direction for a distance of 1 nm between the NPs and for two incident wavelengths: (a) 0.4 µm (b) 1 µm.

Chapter 5: Nanostructured hybrid organic thin films/ QDs

5.1 Introduction of thermal nanoimprint organic layers

The optical properties of hybrid PMMA thin films with CdSe/ZnS QDs were discussed in Chapter 4. It would be interesting if QDs luminescence could be further controllable. The modification of the emission wavelength can be achieved by changing the size of QDs and this has been researched extensively in recent years [47, 115, 116], but there have been rare studies related to the spatial distribution of luminescence. Most of these have been focused on the spatial distribution of QDs site positions such as when they are embedded into an ordered micro-cavity [117, 118]. Such control of luminescent light emission would be useful for important applications such as biological tags or solar cells.

In order to make emitted luminescent light directional, a bi-periodic grating structure combined in the hybrid thin film was considered. The formation of said periodic structure could be achieved through nanoimprint lithography (NIL) techniques. This is because the transition property with temperatures of most polymers allows us to make the same polymer switch from a solid to soft and even a fluid state. To "soften" the organic polymer for imprinting, it is important to make the polymer reach its glass transition temperature (T_g) first. Above the critical temperature of T_g, the polymer starts to change its behavior from glassy to rubbery. When the polymer is below T_g, the large-scale molecular motion does not happen due to being essentially a frozen state of the polymer. In this state it is hard and brittle, just like glass. While heating above T_g, the molecular of polymer can gradually increase their motion in a large scale. These moving molecular states result in a soft type of polymer, just like rubber.

The transition process of a polymer is illustrated in Figure 5.1.1. With increasing temperature, the polymer is heated up and its stiffness starts to be reduced when exceeding the glass transition temperature (T_g). Before it reaches a total rubbery state it will undergo the transition region from glassy to rubbery as can be seen in Figure 5.1.1. Above the critical temperature of T_g the polymer can be readily deformed into the shape of the mold. Other physical properties could be also changed, for example, the volume. Above T_g, the polymer gradually increases its volume due to the molecular motion in a large scale. If the polymer undergoes too much thermal expansion, it could result in a failure when transferring a structural pattern. Thanks to a small thermal expansion coefficient of ~ 5×10^{-5} per °C, PMMA shows excellent properties for applying nanoimprint lithography [48].

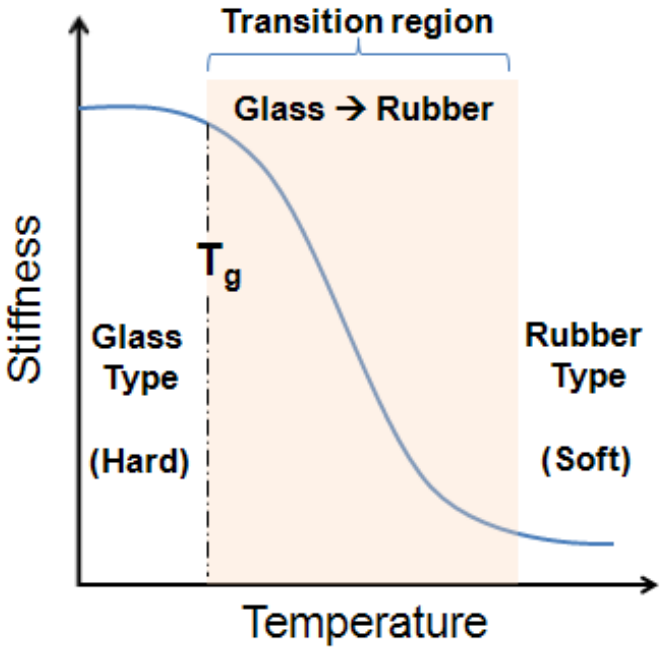

Figure 5.1.1: A polymer transition from glass to rubber type.

5.1.1 Heating experiment for transition temperature of organic layers:

Typically, the commercial PMMA polymer has a transition temperature of around 100~110°C [56, 119], but this value might change when processing different polymer concentrations. For example, 50 mg of PMMA in 1 ml solvent would have a dilution ratio larger than 100 mg PMMA in the same volume of solvent. In addition, a proper pressure is also a key, depending on the heating temperature. Therefore, the thermal imprint condition was first studied in experiential tests.

In order to have a thick enough material for imprinting, we dropped the PMMA solution onto a glass substrate (2.5 cm × 2.5 cm). It fully covered the substrate until it formed a surface tension state. Due to the surface tension state, the sample could be treated as an approximate planar surface around the central position for later imprinting. Once the solvent evaporated, a thick enough PMMA layer was obtained. As shown in Figure 5.1.2, the pressure for the imprint was fixed at around 50 psi in all samples, and the heating temperature was varied from 110°C to 160°C in steps of 10°C.

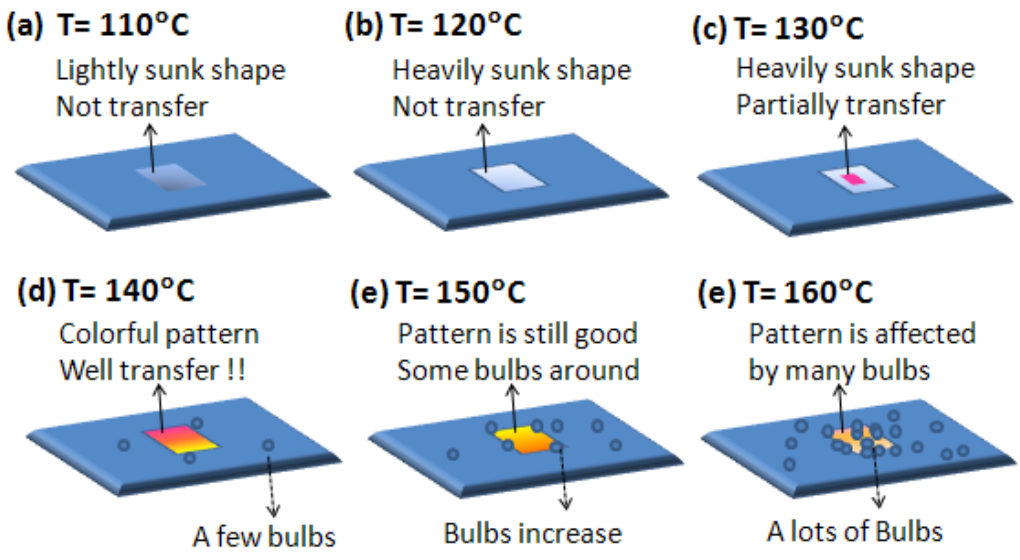

Figure 5.1.2: Heating temperature (T) effects on imprinted pattern: A tested on a PMMA layer.

In the temperature range of 110-120°C, the PMMA surface revealed only a sunk shape and did not exhibit clear transfer patterns. This could be caused by the applied pressure being lighter than in other cases [53]. When the temperature reached 130°C, partially colorful areas indicated a partially transferred pattern. Until the temperature of 140°C, the obviously bright rainbow colors could be observed from the flexible PMMA layer. This was evidence of a strong light diffraction from the imprinted grating structures on its surface. If we kept on heating the sample to a temperature of 150°C, the colorful pattern still remained but some interior air bubbles were generated, because overheating a sample would cause a rapid and huge release of interior air. The phenomenon was worse when heating to 160°C where the pattern contained a large amount of air bubbles. These bubbles could be reduced when the process was done in a vacuum space. In summary, it was found that the most suitable imprinting temperature in normal atmospheres was 140°C and the fewest amounts of defects were obtained when the pressure was 50 psi.

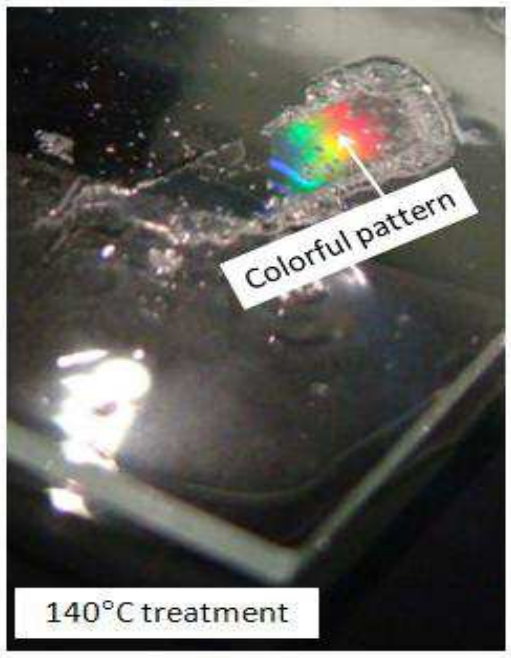

Figure 5.1.3: Transferred pattern showed a colorful appearance on a PMMA layer.

5.1.2 Periodic structure of imprinted pure organic layers:

To determine the quality of the transferred pattern and its periodic property, a tunable Helium-Neon (He-Ne) laser was used. The laser can provide five selectable wavelengths, 543 nm, 594 nm, 604 nm, 612 nm, and 633 nm. In our experiment, the wavelengths of 543 nm, 594 nm and 633 nm were applied.

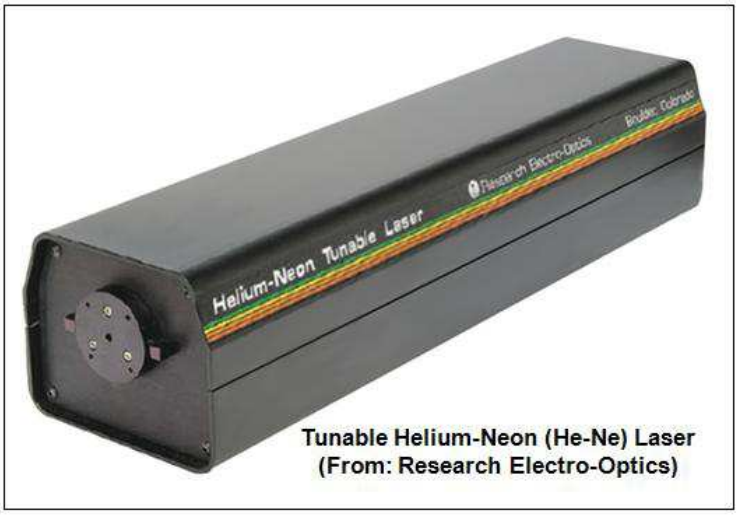

Figure 5.1.4: Tunable He-Ne laser.

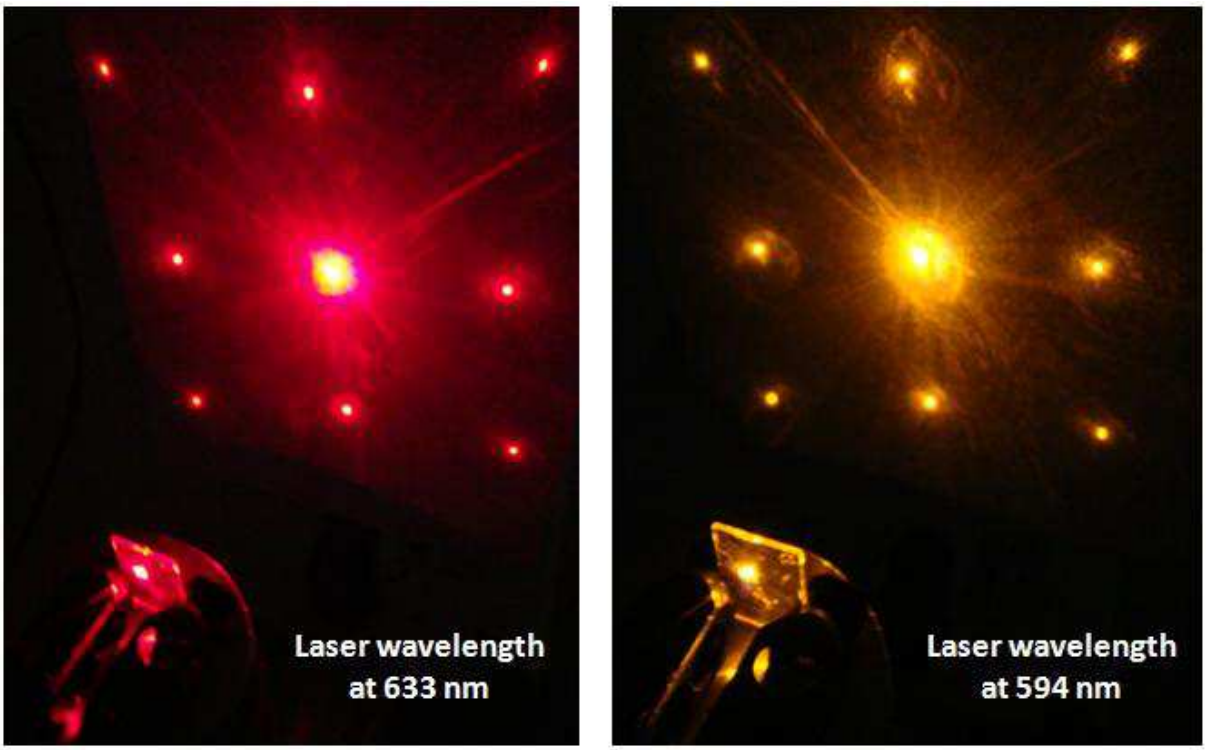

Figure 5.1.5: Periodic structure with good transfer. Left: Tunable laser at emission wavelength of 633 nm. Right: Tunable laser at emission wavelength of 594 nm.

The tunable He-Ne laser is shown in Figure 5.1.4. The laser power levels were 0.3 mW (at a wavelength of 543 nm), 0.6 mW (at a wavelength of 594 nm) and 4.0 mW (at a wavelength of 633 nm), separately. The grating induces diffraction patterns at different angles which have been measured for the three laser wavelengths and compared with the classical diffraction theory. As shown in Figure 5.1.5., significant diffraction patterns were obtained for 633 nm (left part) and 594 nm (right part). The first order diffraction angles were determined at around 23° (at a wavelength of 633 nm) and 21° (at a wavelength of 594 nm). These diffraction angles from different laser wavelength pointed out the same periodic properties of the grating imprinted in PMMA. The related grating period is ~1.6 μm. A random roughness is revealed by a weak spatial dispersion in the zero order diffraction patterns. In comparison, the dispersed zero order diffraction pattern in Figure 5.1.6. indicated a damaged transfer structure.

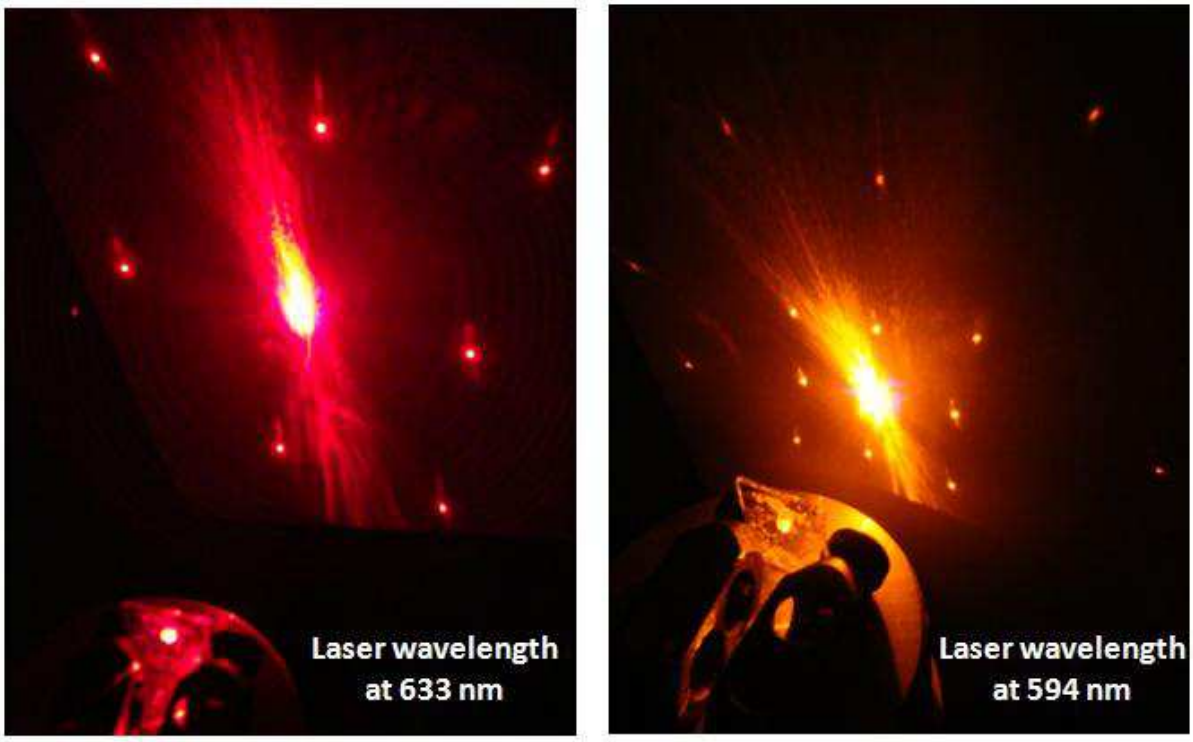

Figure 5.1.6: Periodic structure with bad transfer. Left: Tunable laser at emission wavelength of 633 nm. Right: Tunable laser at emission wavelength of 594 nm.

Since the structural period was estimated from the diffraction angle of the laser beam, an optical probe mapping technique by the STIL system was applied for visualizing these periodic structures based on a chromatic confocal method. Chromatic confocal sensing (STIL patent) was invented in 1995 and is utilized as an accurate and reliable technique for non-contact distance and surface mapping measurements. Furthermore, this non-physical contact technique is important and benefits for a very sticky or soft material surface such as the PMMA polymer used in our study. In Figure 5.1.7 from the STIL SA an illustration of the chromatic confocal system is shown. The microtopography of a sample consists of measuring the altitude (z coordinate) of each point of the surface on the sample. From this proposed technique, the measurement would be achieved by moving the mechanical part along the z axis based on dynamic focusing. In the STIL system a white light source is imaged by an objective lens with extended axial chromatism on a series of monochromatic point images in the measurement region. Due to the confocal configuration, only the focused wavelength will pass through the spatial filter with high efficiency, and all other wavelengths will be out of focus.

Among different STIL commercial systems, the STIL Micromeasure2 was utilized in our measurement. The system provides a minimum laterally scanning step of 0.078 μm. The available probing depth was within the large range of 65 μm which is quite good enough for our layers with thickness around 2 μm. The mapping of a 5 μm × 5 μm is shown in Figure 5.1.8. The periodic property of around 1.6 μm is in good agreement with the estimated result from the laser diffraction angle.

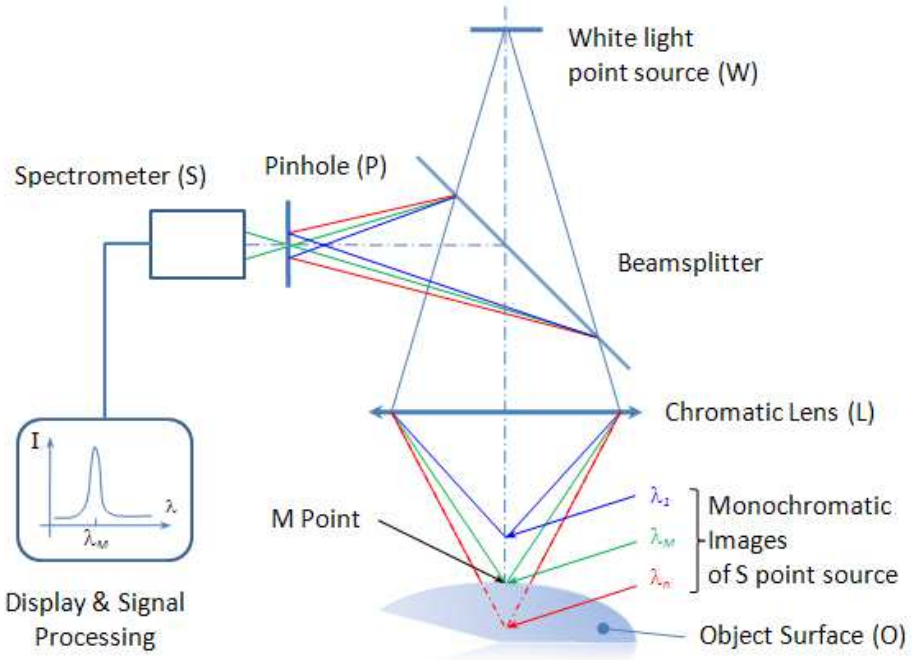

Figure 5.1.7: An illustration of the chromatic confocal system (From the STIL SA).

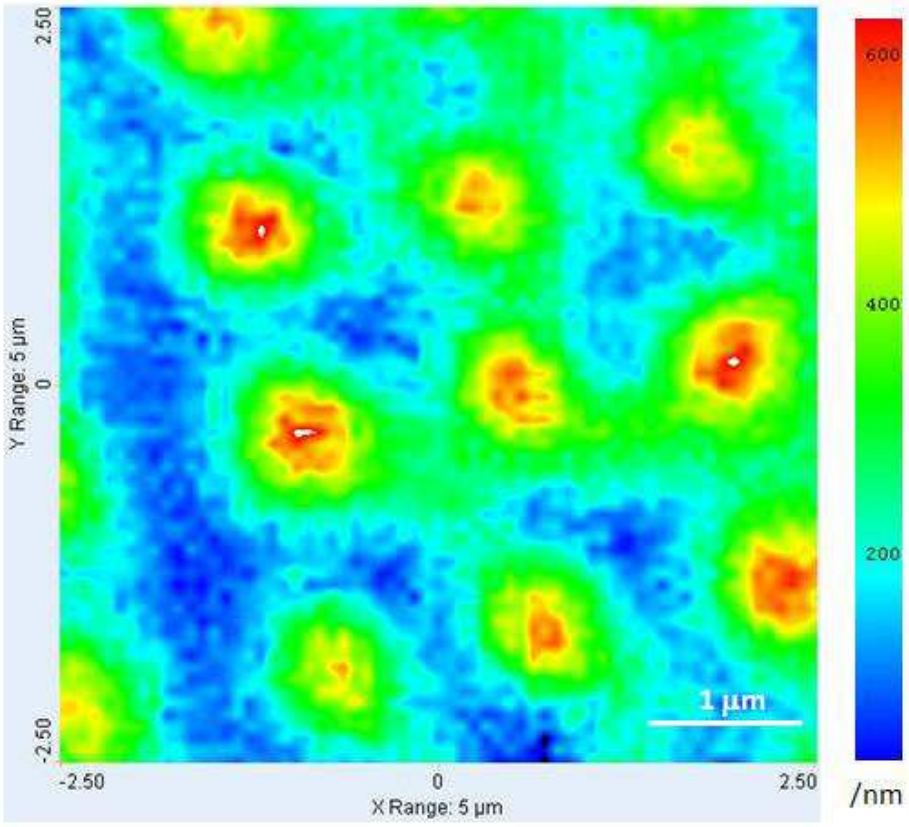

Figure 5.1.8: A 2-D mapping of the periodically imprinted structure of PMMA.

5.2 Imprinted nanostructure in hybrid organic layer with quantum dots

In order to have the emitted luminescent light be directional, a bi-periodic grating structure was constructed into the hybrid thin film layers. In section 5-1 we demonstrated that the imprinted nanostructure can be made efficiently in pure PMMA layers. In this chapter we present our results for the imprinting technique in layers made of hybrid PMMA containing QDs. A direct method to make nanostructure is through electron beam lithography. However, the electron beams with very high energy could strongly degrade the luminescence efficiency of QDs [120]. Hence an indirect structure transferring method is necessary. This is the reason why the nanoimprint method was applied in this research. The nanoimprint technique has many other advantages such as fast-production and repeatable fabrication in order to lower the cost [53].

5.2.1 Fabrication process of imprinted hybrid layers via optimized heating:

The silicon mold patterned by electron beam lithography is shown in Figure 5.2.1(a). Its cross section image is shown in Figure 5.2.1(d) showing a period of ~1.6 ±0.05 μm. This mold is the same as the one used to imprint PMMA. The preparation of hybrid thin film layers of PMMA/ core-shell CdSe/ZnS QDs on a glass substrate was the same as described in Chapter 4. Due to the transition temperature of PMMA [56, 121] and testing results in the last section, the patterned silicon mold should be homogeneously pre-heated at 140°C on a metal-top hot plate for 5 min before imprinting. During the imprinting process, a pressure above 50 psi was homogeneously applied on the samples for 15 min, meanwhile, the heat treatment was kept on the silicon mold as shown in Figure 5.2.1(b) and Figure 5.2.1(e). After imprinting, the temperature was cooled down

to room temperature in order to demold the attached sample. A good transfer of the structure to the hybrid thin film can be finally achieved as illustrated in Figure 5.2.1(c) with the cross section in Figure 5.2.1(f).

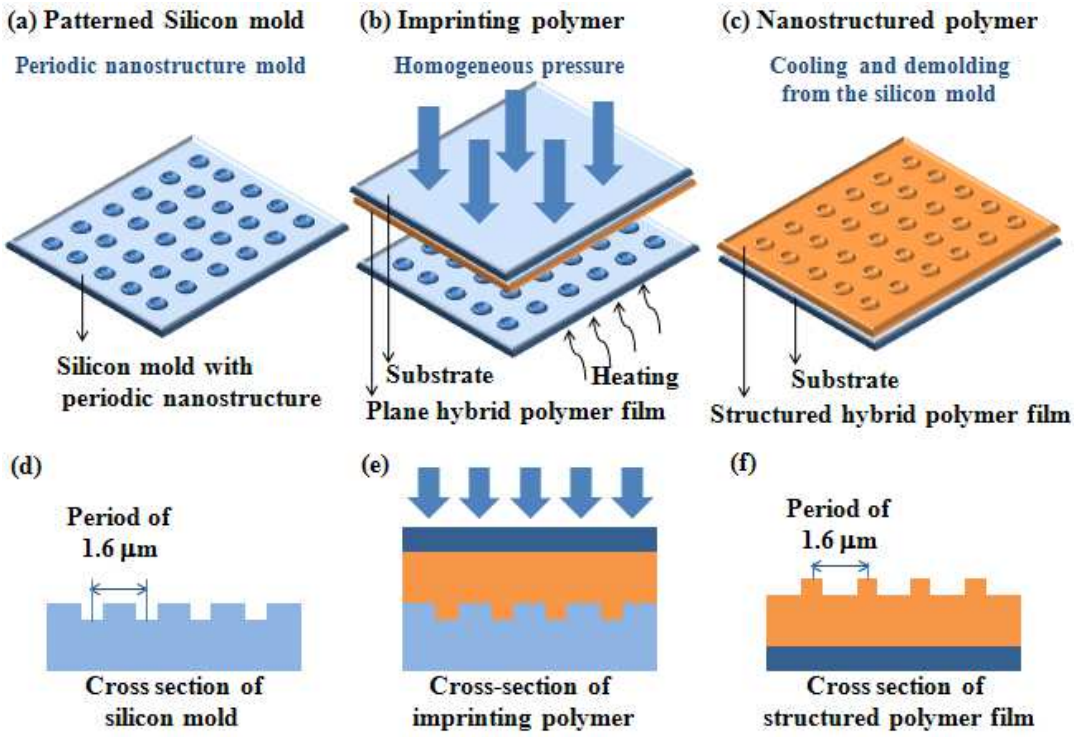

Figure 5.2.1: Nanoimprinting method applied in order to obtain nanostructured polymer films: (a) sketch of a silicon mold with a periodic structure and (d) is its cross section; (b) principle of the imprinting process via thermal imprinting lithography (NIL) and (e) in cross section; (c) shows the expected nanostructured hybrid polymer with its cross section (f).

5.2.2 Periodic structure of imprinted hybrid layers:

Through an optical probe mapping technique (STIL Micromeasure2), the imprinted samples including the silicon mold were all characterized. In the morphology analysis the originally patterned silicon mold has a period of around 1.6 µm and a hole diameter of around 1.2 µm, as shown in Figure 5.2.2. In this figure, the upper image shows the morphology mapping result, and the lower one is its cross sectional profile. As can be seen, the depth of each hole was

around 1 μm. These holes have a homogeneous distribution with a fixed constant period and a constant depth.

In this figure, there were several holes with shallower characteristics. We found this was because multiple usages of the same mold caused degradation after too many uses (over 15 times). Even though the mold was cleaned using chloroform, acetone and isopropyl alcohol (each step with 5 min ultrasonic vibration) before and after each imprint process, some sticky PMMA were still residual in some places. This could be improved by a surface treatment [48].

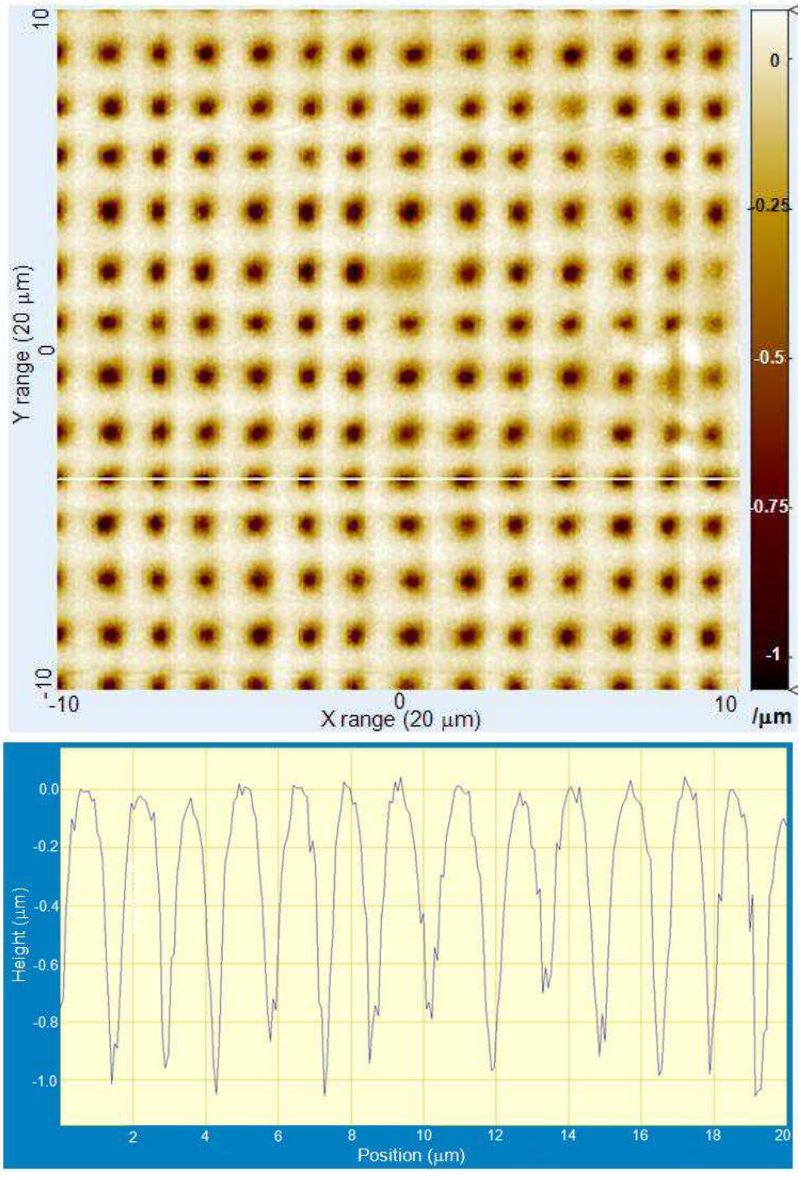

Figure 5.2.2: Patterned silicon mold with its periodic structure.

After imprinting, the hybrid QDs-polymer layers exhibited the same periodic structure (around 1.6 ± 0.05 μm) which was well transferred from the original silicon mold as shown in Figure 5.2.3. In this figure, the upper image gives a morphology mapping result, and the lower one shows its cross sectional profile selected from the dashed line of the upper image. As it can been seen in the profile, the transferred height of each cylindrical-like structure was around 0.6 ± 0.05 μm. Compared to the original depth of the silicon mold the structure height transferred into the hybrid layers was about 0.6 times of it. Regarding the whole thickness of the hybrid thin film layer (~2 μm), the structured part (~0.6 μm) could be enough for directing the emission. The capacity to control the emission direction was estimated by optical field simulations described in later sections.

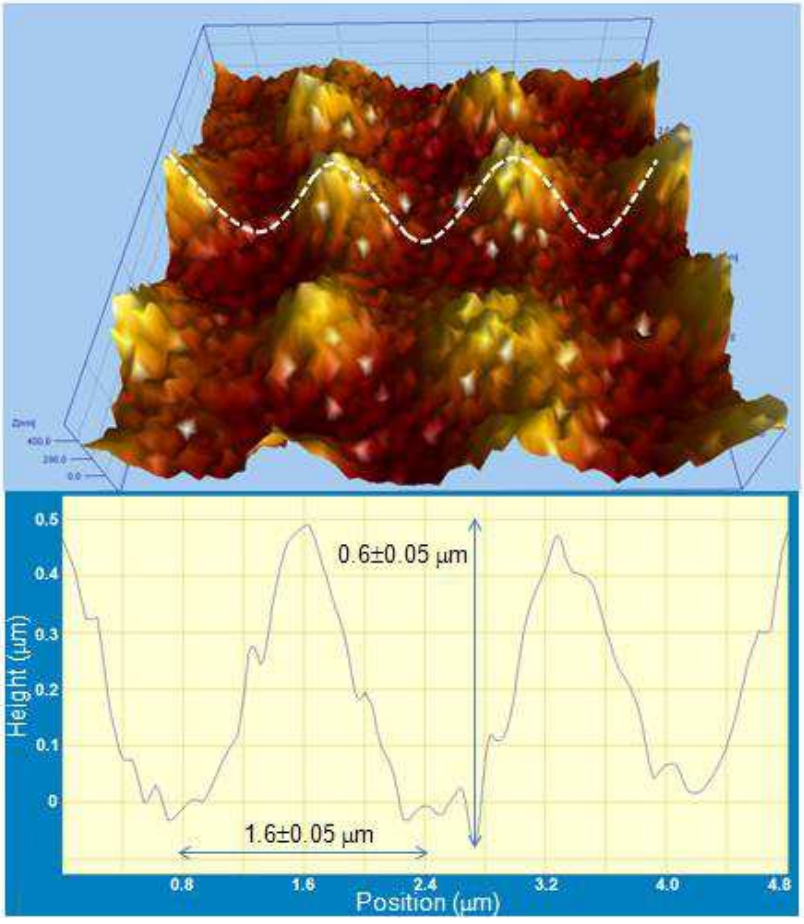

Figure 5.2.3: Nanostructured hybrid thin film with QDs via nanoimprint using a mold made by e-beam lithography.

5.3 Optical field emission simulation for the periodic nanostructure

As seen in previous sections the period of structured hybrid thin film and its emission spectrum have been characterized. The diffraction angles can be estimated by the classical diffraction theory. The diffraction angle, θ_m, from a periodic grating of period d can be expressed by Eq. (1) for the wavelength λ. The diffracted order is represented by m.

$$\theta_m = \sin^{-1}\left(\frac{m\lambda}{d}\right) \tag{1}$$

Figure 5.3.1 shows the first order diffraction angles (m=1) versus different propagation wavelengths from 300 nm to 700 nm determined for a period grating of 1.6 μm. The period error of around ± 3 % in the transferred structure was taken into account. Since the QDs emission wavelength is 560 nm, the first order diffraction angle is predicted at 20.5 ± 0.67°.

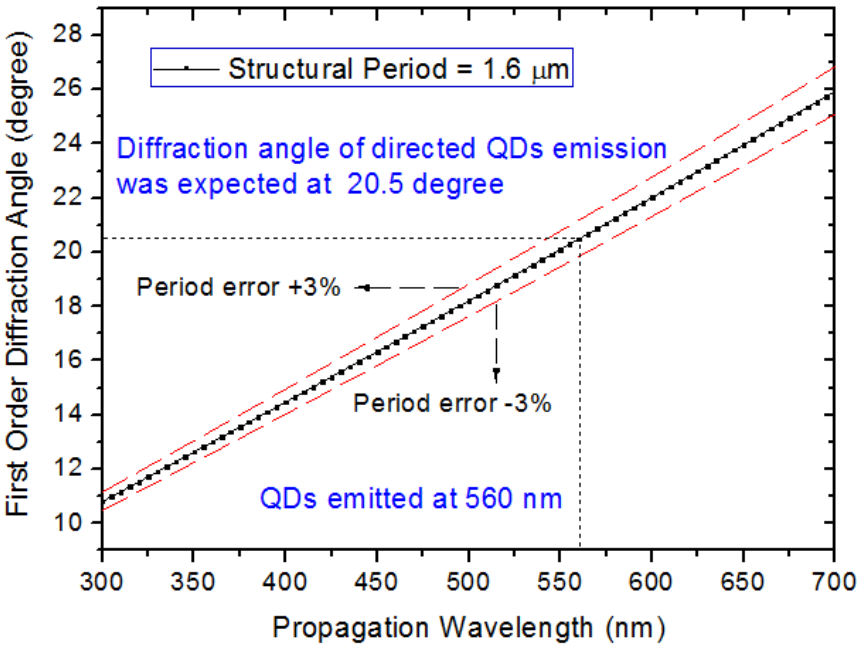

Figure 5.3.1: Calculated first order diffraction angle vs. wavelength for a grating period of 1.6 μm. As the emission wavelength of the QDs of 560 nm, the diffraction angle is expected to be 20.5°.

5.3.1 Plane wave light emission in the nanostructure:

In order to further investigate the electric field distribution in the periodic nanostructure thin film, the finite difference time domain (FDTD) simulation was applied. The cross section of the structure considered in the simulation is illustrated in Figure 5.3.2(a). The period is 1.6 µm. The height of each cylinder is 0.6 µm and the diameter of each is 1.2 µm, as shown by the morphology measurement. Figure 5.3.2(b) shows an illustration of the top view of the model used. The region surrounded by a square dashed line is the repeatable unit cell considered.

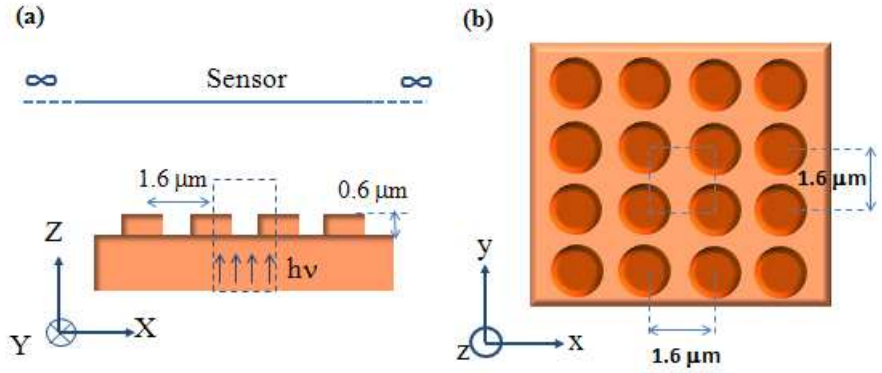

Figure 5.3.2(a) Cross section of simulation structure; (b) top view of simulation structure.

5.3.1(a) Emission light simulation in near field:

The light emitted from QDs under laser illumination was assumed to be beneath the periodic structure and homogeneously distributed. The emitting non-structured film was decomposed in thin slices. All the slices were assumed to be the same. In these assumed slices, the QDs had a dense distribution as observed from the TEM measurement. These emitting dots could be seen as continuous wave packages. Thus, each of the slices could be further treated as a plane wave emission source emitting in the k_z direction. The considered emission wavelength was of 560 nm. As can be seen with the field distribution

in the cross section structure of Figure 5.3.3, the QDs emission source is significantly redirected while propagating out of the periodic structure.

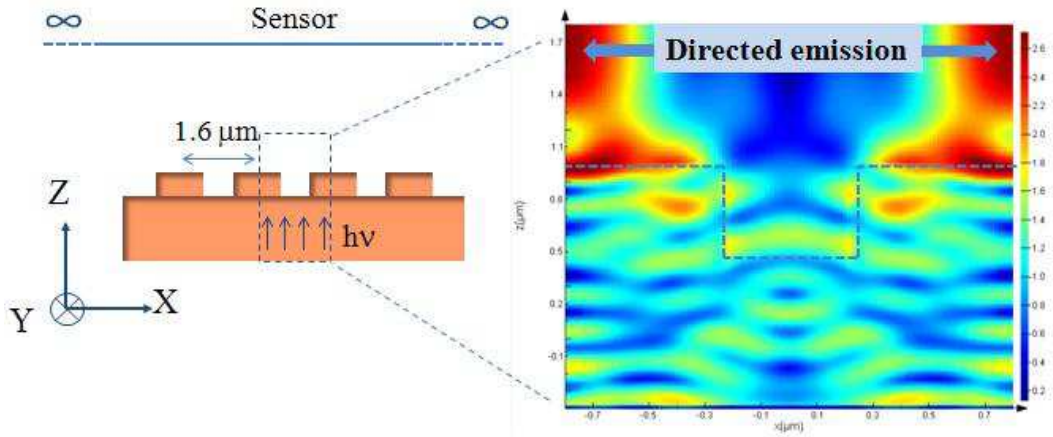

Figure 5.3.3 Left: Cross section of the structure. Right: Electric field simulation at 560 nm.

The electric field distribution at the top of the bi-periodic structure surface has also been calculated, (right part of Figure 5.3.4). The calculations were performed for a localized square region limited by the dashed line shown in the left part of Figure 5.3.4 repeated periodically in the X- and Y-dimensions. In the dashed line region, the electric field distribution was calculated for a detecting sensor in front of the structure. It can be seen in the right part of the figure that the electric field is strongly concentrated in the four corners corresponding to the cylinder position.

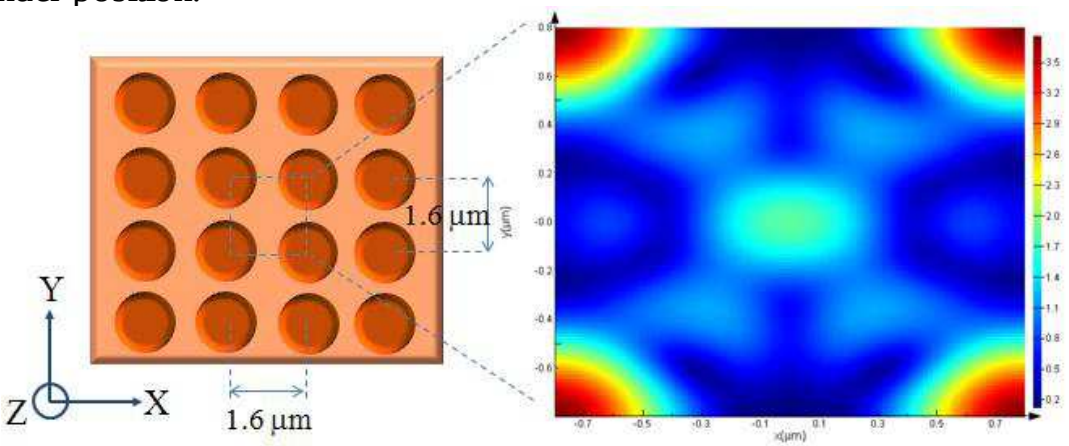

Figure 5.3.4 Left: Top view of the structure. Right: Electric field simulation from the dashed region.

5.3.1(b) Emission light simulation in far field:

From the above calculations, we see that the FDTD method could solve the electric field distribution throughout the periodic structure. In practice, it would also be interesting if the field could be predicted far away from our modeled region. Since the recorded information in the electric field distribution was known on the local field detecting sensor, the field can then propagate to any position in the half-space above the surface of the detecting sensor. From the local field to the far field, the transformation technique is based on the equivalence principle for near-to-far-field transformations [122-124]. According to this equivalence principle, the electromagnetic field distribution outside an imaginary closed surface (a virtual surface) surrounding the object of interest can be obtained if the equivalent sources on the closed surface are known [122]. In the propagation space, it was assumed that the medium (air) is homogeneous and isotropic. Therefore, the field could be projected as a function of the angle into the far field space above the detecting surface. In our FDTD far field calculation, a visually hemispherical curve with 1 meter radius fully covered the upper space of the sample as shown in Figure 5.3.5. The sample was centered in the hemispherical curve. Upon the sample, the near field sensor was set for acquiring the electric field distribution as shown in Figure 5.3.4 calculated with the near-to-far-field transformation. The field profile projected on a plane surface is shown in Figure 5.3.6. As can be seen in the figure, the emission light was then mostly distributed in the first order diffraction patterns at angles located at around 20°, in agreement with the previous calculation of diffraction by a grating (Figure 5.3.1). On the other hand, it is not only this first order but also the second order diffraction angle of around 44.5° which is well matched with the angles calculated with the classical diffraction theory. Even though the

intensity of second order diffraction patterns was much weaker than the first order diffraction, it can still be observed as marked in Figure 5.3.6.

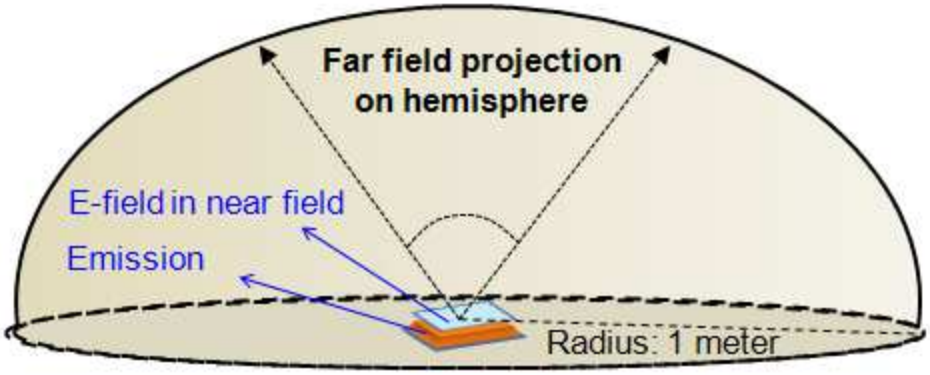

Figure 5.3.5: An illustration of far field projection on hemisphere curve.

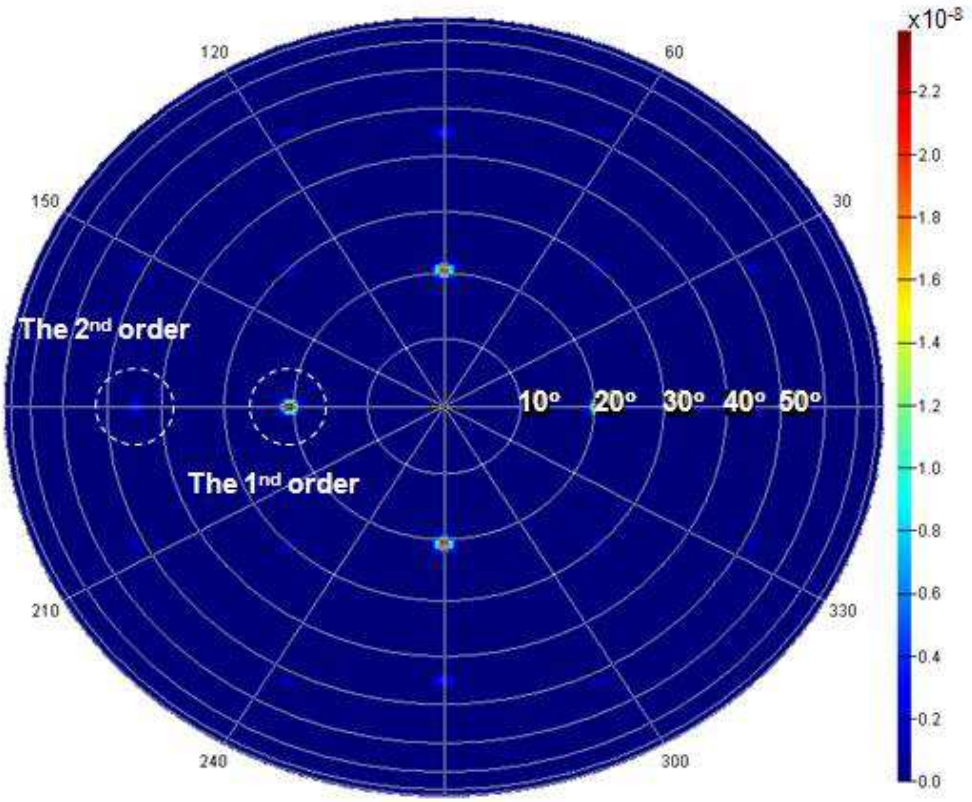

Figure 5.3.6: Far field simulation of diffraction pattern distribution with emission wavelength of 560 nm.

5.3.2 Dipole source emission light in the nanostructure:

From the above section, the k_z direction plane wave emission source has been applied due to the assumption of a dense QDs distribution. In this section, we discuss another situation of a random dipole emission from QDs instead of a plane wave emission. Such an assumption is made because QDs distribution can sometimes be imperfect and separated. Hence the hybrid film could be treated as containing random emission sources. In this study, these random sources were analogized to random dipole emissions. These random dipoles with same amplitude but random emission direction were set in the X-Y plane where the emitted plane wave was considered previously as shown in Figure 5.3.7. The other parameters such as structural geometries and surroundings were set to be the same. The simulation results will be discussed in the following section.

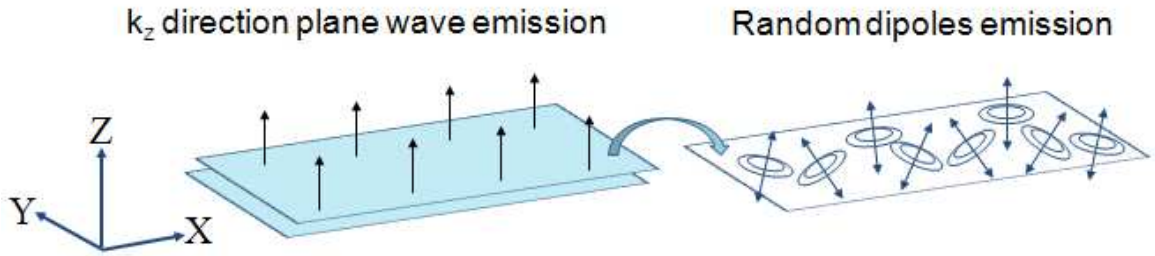

Figure 5.3.7 Left: k_z direction plane wave emission source. Right: Random dipoles emission sources at wavelength of 560 nm.

5.3.2(a) Emission light simulation in near field:

In this section, the light emitted from QDs under laser illumination is assumed to come from random direction and homogeneously distributed dipole sources. The left image in Figure 5.3.8 is an illustration of the periodic structure containing random dipole emitting sources and the right image is the cross section of electric field distribution. Due to the random emission direction from

dipole sources, the emission light would be more readily trapped in the structured film. As shown in the right part of Figure 5.3.8, the electric field was mainly confined inside the structure and only a small amount of light is transmitted out of the structure. In order to investigate how the electric field is getting out of the structure, the calculation was focused on the region just above the top of the cylindrical structure. The electric field distribution above the structure is shown in Figure 5.3.9, after rescaling the field.

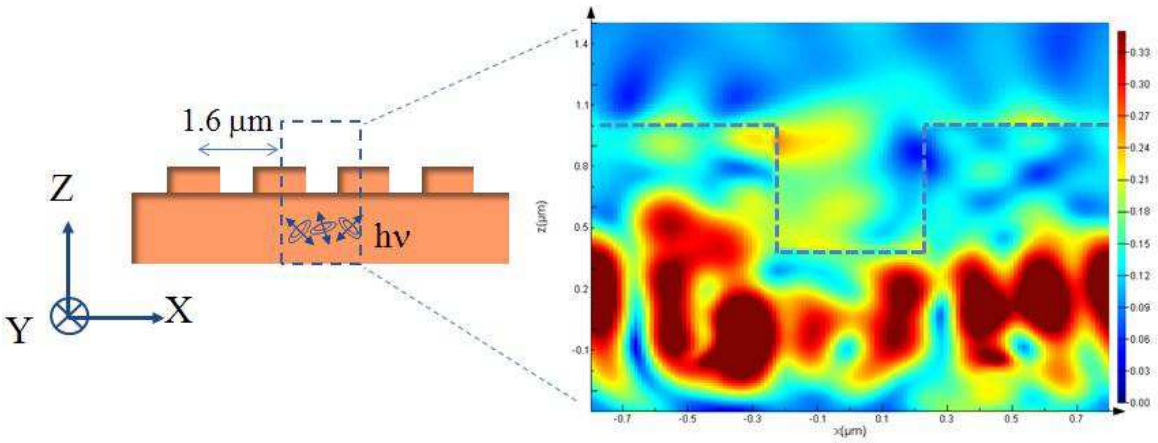

Figure 5.3.8 Left: Cross section of the structure. Right: Electric field simulation with random dipoles emission at wavelength of 560 nm.

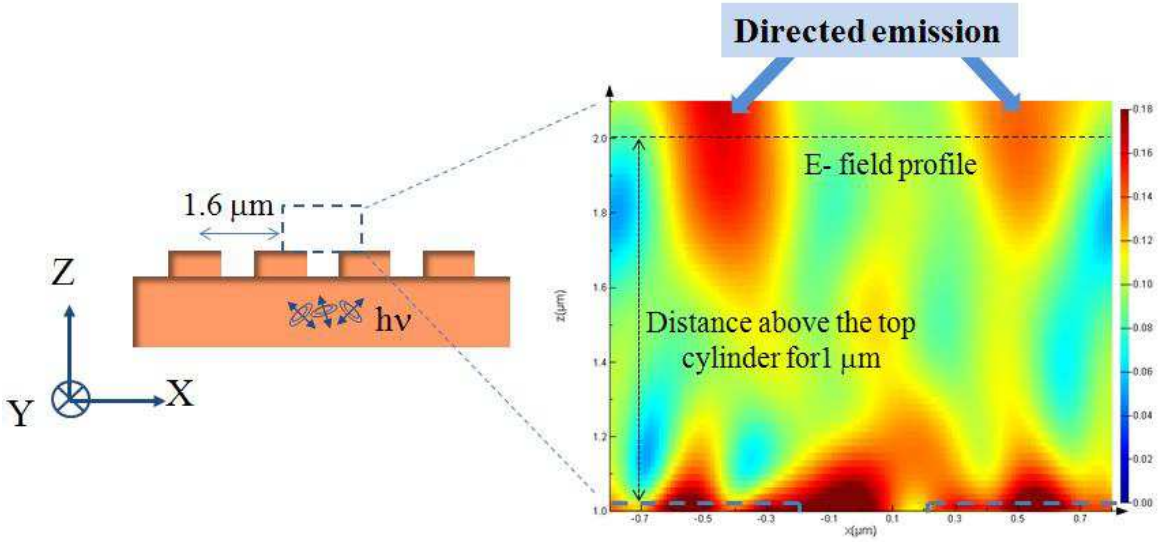

Figure 5.3.9: Left: Simulation region located just above the structure. Right: Electric field simulation from random dipoles emission.

In Figure 5.3.9, the simulation zone is indicated by the dashed line. The bottom of this zone is positioned at the top of the cylinders. We understand that the light emitted by electric dipoles was randomly transmitted out of the structure according to the electric field distribution. Surrounding the structures, the electric field was quite strong and was about to propagate. Above the structure around 0.5 μm, we found that the originally random emission light started to propagate in specific directions. This directional propagation means the emissions could be directed. To investigate the propagating emission, the electric profile was taken at the distance of 1 μm above the top cylinder as shown in Figure 5.3.9. Along the dash line the electric field profile was recorded and plotted as it can be seen in Figure 5.3.10. Due to the emissions from the random electric dipoles, the field distribution inside the structure essentially had a difference. This resulted in the distinct electric field intensities of these emissions. However, in our investigation, these output emissions, could still be directed in their spatial propagation.

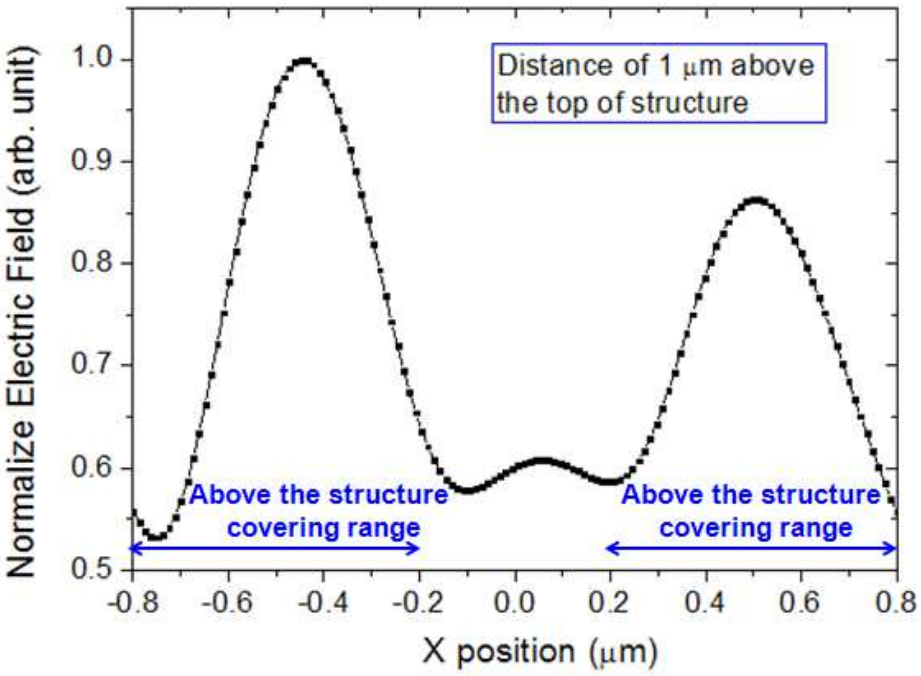

Figure 5.3.10: Electric field profile from distance 1 μm above the top cylinder structure.

The electric field distribution at the top of the bi-periodic structure surface is shown in the right part of Figure 5.3.11. The calculations were focused on a localized square region, limited by the dashed line in the left part of Figure 5.3.11, because of the periodicity in the X- and Y-dimensions. Before considering the structure, these random direction dipoles with homogeneous distribution were nearly the same and a slight difference in electric field caused from their random directions. But after considering the structure, it was found that the calculated electric field was strongly concentrated in the four corners corresponding to the cylindrical positioning as shown in the right part of Figure 5.3.11. Compared to previous plane wave emissions, random dipole emissions had random directions but still maintained a localized local field distribution.

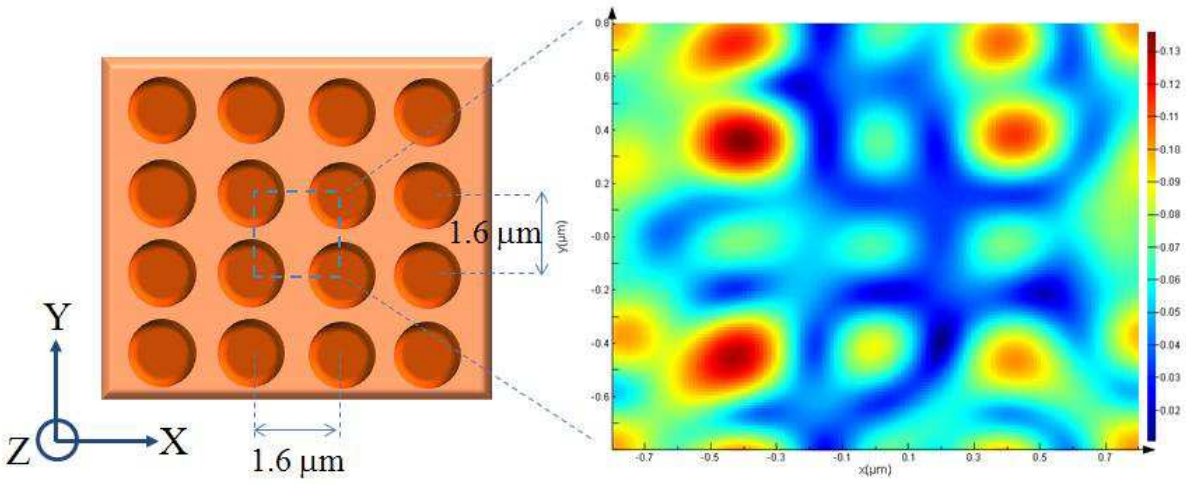

Figure 5.3.11 Left: Top view of the structure. Right: Electric field simulation with random dipoles emission from the selected region.

5.3.2(b) Emission light simulation in far field:

To study the far field behavior, we took these random dipole emissions in order to calculate the far field simulation using the same method discussed in section 5.3.1(b). The calculation shows that the diffraction pattern is located around particular directions in the far field projection as shown in Figure 5.3.12.

In comparison with the plane wave emission, these random dipole emissions give larger spots in the far field projection. This behavior can be attributed to the dipole emissions with random direction. Considering the center of the spots the first order diffraction angle is still shown and located at similar angles around 20°. So this periodic structure has the ability to direct the QDs emission light. This concept is expected to be applicable in optoelectronic devices and biological tags.

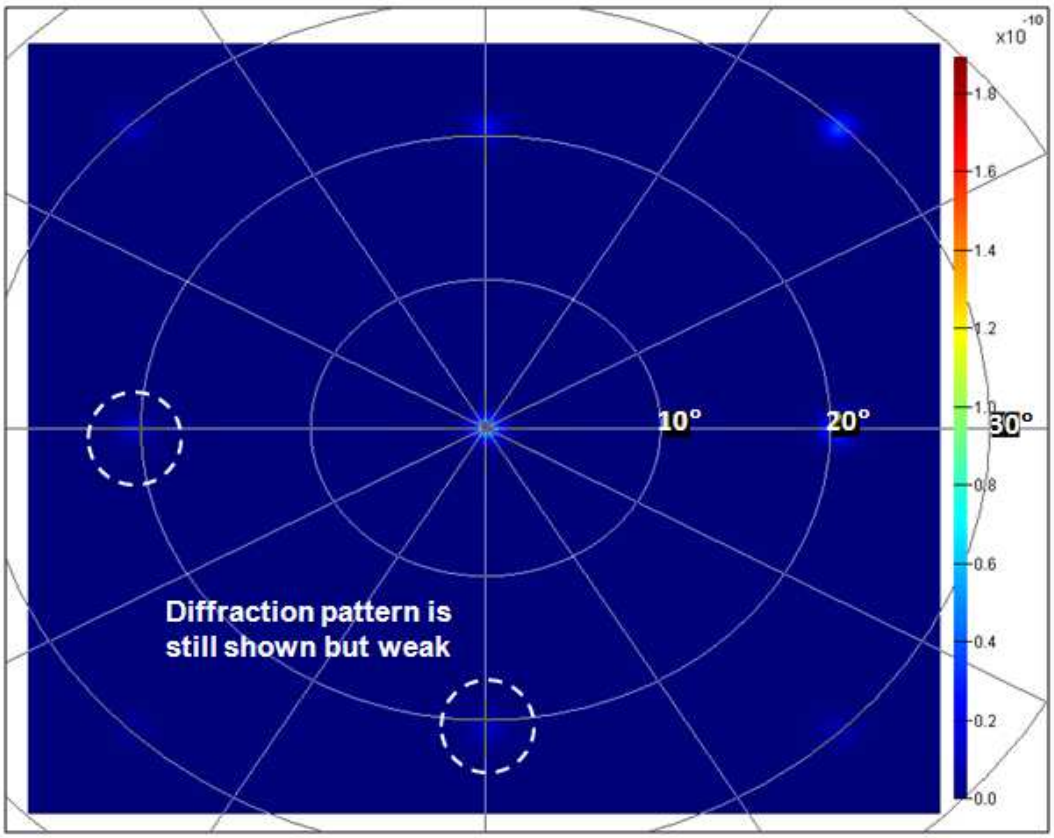

Figure 5.3.12: Far field simulation of diffraction pattern distribution from random dipoles emission at wavelength of 560 nm.

Chapitre 6: Conclusions et perspectives

Des films minces de PMMA contenant des boites quantiques de CdSe/ ZnS ont été fabriqués avec succès. L'effet de confinement quantique a des conséquences évidentes sur l'absorption et la luminescence de ces couches. Il a été constaté que le spectre d'absorption est principalement défini par les boites quantiques dans le domaine visible, grâce à la grande transparence de PMMA dans cette gamme de longueur d'onde. À la suite du fort confinement quantique dans ce type de structure cœur-coquille, un pic de luminescence a également été obtenu à une longueur d'onde d'environ 560 nm. Par rapport au pic d'absorption principal situé aux alentours de 545 nm, on note une conversion de fréquence. En prenant cette propriété de conversion de fréquence en considération pour des applications, nous avons démontré expérimentalement l'intérêt de l'insertion d'une couche de boites quantiques hybrides devant des cellules solaires pour convertir le spectre solaire UV dans le spectre visible. Les photons luminescents supplémentaires peuvent ensuite être absorbés par les cellules solaires. Grâce à la mesure de rendement quantique externe d'une cellule solaire en silicium, nous nous sommes assurés d'avoir effectivement une augmentation de la production de charge. Il a ainsi été montré que le courant initial de court-circuit (Isc) de 2 mA de la cellule solaire peut être porté à 2.43 mA. En outre, nous avons montré par simulation numérique qu'une autre amélioration peut provenir d'une augmentation du champ électrique optique entre chacune des boites quantiques incorporées dans la couche active de cellules solaires. On peut remarquer que ces résultats sont obtenus pour des structures beaucoup plus petites que la longueur d'onde.

Grâce à des mesures de photoluminescence en fonction du temps, nous avons montré que l'effet de couplage entre les boites quantiques apparaît pour des concentrations croissantes de QDs. Avec des pourcentages plus élevés de boites quantiques, les plus denses d'entre elles ont plus de chance d'être couplées les unes aux autres et les transferts d'électrons sont augmentés. Des décalages vers le rouge du spectre d'absorption et du spectre de luminescence sont observés lorsque l'on augmente ainsi la proportion de boites quantiques. En outre, lorsque l'on augmente la puissance de pompage par laser, un décalage vers le bleu apparaît avec une augmentation de l'intensité de luminescence qui pourrait être due à une augmentation de la barrière de potentiel induite par la lumière. Cette barrière accrue pourrait piéger des porteurs de charge menant ainsi à une accumulation dans les niveaux élevés d'énergie, résultant en un tel décalage vers le bleu. Cependant, il a également été constaté que l'intensité de la luminescence commence à se réduire après des temps d'illumination laser plus longs. Après une analyse approfondie, nous avons constaté que la réduction du couplage exciton-phonon a plus facilement lieu avec les boites quantiques denses. Nous avons proposé que ce puisse être causé par un phonon liant les boites quantiques voisines.

Pour d'autres applications de couches hybrides incluant des QDs de forte luminescence, il est important de montrer que la direction de la lumière émise peut être contrôlée. A cet effet, nous avons démontré que ceci est rendu possible en structurant le film hybride par des techniques de nanoimpression. Nous avons montré qu'un bon transfert d'un motif bi-périodique de 1.6 µm et d'un motif de trous de 1.2 µm de diamètre réalisés par lithographie par faisceau d'électrons sur un moule en silicium dans des couches hybrides en PMMA/ QD peut être obtenue. Afin d'étudier les émissions directionnelles de couches, deux

types de simulations ont été utilisés pour calculer les distributions du champ électrique : par FDTD et par la théorie de la diffraction classique. Les distributions de lumière calculées à 1 mètre de distance de l'échantillon sont en bon accord entre les deux méthodes. Cela montre qu'il est possible de contrôler la propagation de la luminescence des boîtes quantiques inclues dans des couches minces, ce qui peut trouver de nombreuses applications telles que les cellules solaires, les voyants ou encore les étiquettes biologiques.

Perspectives

Ce travail ouvre la voie à un grand nombre de recherches futures:

- Nous n'avons considéré que le cas de matériaux hybrides organiques/ inorganiques semi-conducteurs réalisés sous forme de films minces de PMMA incluant des boites quantiques de CdSe/ ZnS. Des travaux futurs pourraient être effectués pour étendre ces études à d'autres composés hybrides utilisant, par exemple des boites quantiques de TiO_2. Il serait en effet utile de comprendre les caractéristiques de ce matériau à l'échelle nanométriques.
- Nous avons présenté un moyen d'augmenter l'efficacité des cellules solaires en plaçant une couche hybrides contenant des boites quantiques devant les cellules pour convertir la partie UV du spectre solaire en lumière visible. Toutefois, dans notre cas, la gamme d'absorption des couches étudiées couvre un large spectre en-dessous des 560 nm correspondant au pic de luminescence des boites quantiques. En conséquence, l'efficacité totale de conversion des cellules solaires pourrait être encore améliorée en utilisant d'autres boites quantiques toujours pour collecter le plus possible les UV proches mais sans absorber dans le visible.

- Les travaux futurs pourraient également se concentrer sur les boites quantiques directement incorporées dans les cellules solaires photovoltaïques pendant leur fabrication, pour une meilleure utilisation des photons luminescents. D'autre part, les couches hybrides organiques/ QD peuvent également être structurées sous forme de cristaux photoniques faites par nanoimpression de façon à améliorer le piégeage de la lumière et obtenir une autre voie pour augmenter l'absorption optique.
- Le contrôle de la distribution spatiale de l'émission de boites quantiques a été proposé en utilisant une structure bi-périodique réalisée par nanoimprint. Cependant, il n'a pas été possible de mesurer la répartition conique de la lumière luminescente émise. Ceci peut être effectué en utilisant un détecteur sensible à la lumière se déplaçant autour de l'échantillon. En outre la distribution spatiale précise de lumière est perturbée par la dispersion de la lumière provoquée par la rugosité de la surface. Par conséquent, les travaux futurs pourraient se concentrer sur une technique de lissage de surface afin de réduire la partie diffusée de la lumière. En outre, les considérations ci-dessus peuvent être également prises en compte dans la simulation, en incluant d'autres facteurs tels que l'effet du substrat ou d'autres structures différentes.

L'étude générales des propriétés de couches hybrides organiques/ inorganiques boites quantiques semi-conducteurs a été menée montrant de nouvelles propriétés et applications. Mais il y a encore beaucoup de place pour d'autres champs de recherche et avec de la créativité et de nouvelles idées. Dans les années qui suivent, nous prévoyons d'être en mesure de contribuer de façon continue à de nouvelles idées et concepts, toujours en utilisant les propriétés des

boîtes quantiques et pour les utiliser dans des applications. Plus généralement, des progrès portant sur l'énergie, avec la prochaine génération de cellules solaires photovoltaïques, ainsi que de nombreuses autres applications de ces nanomatériaux complexes combinés avec des nanostructures sont attendus dans un proche avenir.

Bibliography

1. F. Flory, L. Escoubas, and G. Berginc, "Optical properties of nanostructured materials: a review," Journal of Nanophotonics **5**, 052502 (2011).
2. G. Morello, *Optical Properties of Spherical Colloidal Nanocrystals, Fingerprints in the Optical and Transport Properties of Quantum Dots* (InTech, 2012).
3. R. Krahne, G. Morello, A. Figuerola, C. George, S. Deka, and L. Manna, "Physical properties of elongated inorganic nanoparticles," Physics Reports **501**, 75-221 (2011).
4. Y. Yang, Y.-Q. Li, S.-Y. Fu, and H.-M. Xiao, "Transparent and light-emitting epoxy nanocomposites containing ZnO quantum dots as encapsulating materials for solid state lighting," The Journal of Physical Chemistry C **112**, 10553-10558 (2008).
5. J. Albero, E. Martinez-Ferrero, J. Ajuria, C. Waldauf, R. Pacios, and E. Palomares, "Photo-induced electron recombination dynamics in CdSe/P3HT hybrid heterojunctions," Physical chemistry chemical physics : PCCP **11**, 9644-9647 (2009).
6. R. E. Bailey, A. M. Smith, and S. Nie, "Quantum dots in biology and medicine," Physica E: Low-dimensional Systems and Nanostructures **25**, 1-12 (2004).
7. J. Drbohlavova, V. Adam, R. Kizek, and J. Hubalek, "Quantum dots - characterization, preparation and usage in biological systems," International journal of molecular sciences **10**, 656-673 (2009).
8. T. Tani, H. Horiuchi, M. Oda, E. Usukura, H. Sakai, A. Ohtaki, and M. Yohda, "Energy transfer in hybrid CdSe quantum dots vs. labelled molecular chaperone systems by imaging microscopy," physica status solidi (c) **6**, 912-915 (2009).
9. M. Molnar, Y. Fu, P. Friberg, and Y. Chen, "Optical characterization of colloidal CdSe quantum dots in endothelial progenitor cells," Journal of nanobiotechnology **8**, 2 (2010).
10. E. Stratakis, V. Zorba, M. Barberoglou, E. Spanakis, S. Rhizopoulou, P. Tzanetakis, S. Anastasiadis, and C. Fotakis, "Laser structuring of water-repellent biomimetic surfaces," SPIE Newsroom **10**, 1441 (2009).
11. G. Tayeb, B. Gralak, and S. Enoch, "Structural Colors in Nature and Butterfly-Wing Modeling," Optics and Photonics News **14**, 38-43 (2003).
12. T. Saison, C. Peroz, V. Chauveau, S. Berthier, E. Sondergard, and H. Arribart, "Replication of butterfly wing and natural lotus leaf structures by nanoimprint on silica sol-gel films," Bioinspiration & biomimetics **3**, 046004 (2008).
13. A. L. Ekimov, and A. A. Onushchenko, "Quantum size effect in three-dimensional microscopic semiconductor crystals," Journal of Experimental and Theoretical Physics Letters **34**, 345-349 (1982).
14. M. A. Reed, J. N. Randall, R. J. Aggarwal, R. J. Matyi, T. M. Moore, and A. E. Wetsel, "Observation of discrete electronic states in a zero-dimensional semiconductor nanostructure," Physical Review Letters **60**, 535-537 (1988).

15. C. B. Murray, C. Kagan, and M. Bawendi, "Synthesis and characterization of monodisperse nanocrystals and close-packed nanocrystal assemblies," Annual Review of Materials Science **30**, 545-610 (2000).
16. V. K. L. Mer, "Nucleation in Phase Transitions," Industrial & Engineering Chemistry **44**, 1270-1277 (1952).
17. J. Shiang, A. Kadavanich, R. Grubbs, and A. Alivisatos, "Symmetry of annealed wurtzite CdSe nanocrystals: assignment to the C3v point group," The Journal of Physical Chemistry **99**, 17417-17422 (1995).
18. G. D. Scholes, "Controlling the Optical Properties of Inorganic Nanoparticles," Advanced Functional Materials **18**, 1157-1172 (2008).
19. M. A. Hines, and G. D. Scholes, "Colloidal PbS Nanocrystals with Size-Tunable Near-Infrared Emission: Observation of Post-Synthesis Self-Narrowing of the Particle Size Distribution," Advanced Materials **15**, 1844-1849 (2003).
20. A. Yoffe, "Semiconductor quantum dots and related systems: electronic, optical, luminescence and related properties of low dimensional systems," Advances in Physics **50**, 1-208 (2001).
21. S. Baskoutas, and A. F. Terzis, "Size-dependent band gap of colloidal quantum dots," Journal of Applied Physics **99**, 013708 (2006).
22. E. M. Boatman, G. C. Lisensky, and K. J. Nordell, "A Safer, Easier, Faster Synthesis for CdSe Quantum Dot Nanocrystals," Journal of Chemical Education **82**, 1697-1699 (2005).
23. P. D. Cozzoli, T. Pellegrino, and L. Manna, "Synthesis, properties and perspectives of hybrid nanocrystal structures," Chemical Society Reviews **35**, 1195-1208 (2006).
24. A. M. Smith, and S. Nie, "Semiconductor Nanocrystals: Structure, Properties, and Band Gap Engineering," Accounts of Chemical Research **43**, 190-200 (2012).
25. M. Jones, S. S. Lo, and G. D. Scholes, "Quantitative modeling of the role of surface traps in CdSe/CdS/ZnS nanocrystal photoluminescence decay dynamics," Proceedings of the National Academy of Sciences **106**, 3011-3016 (2009).
26. S.-H. Wei, and A. Zunger, "Calculated natural band offsets of all II–VI and III–V semiconductors: Chemical trends and the role of cation *d* orbitals," Applied Physics Letters **72**, 2011-2013 (1998).
27. B. O. Dabbousi, J. Rodriguez-Viejo, F. V. Mikulec, J. R. Heine, H. Mattoussi, R. Ober, K. F. Jensen, and M. G. Bawendi, "(CdSe)ZnS Core-Shell Quantum Dots: Synthesis and Characterization of a Size Series of Highly Luminescent Nanocrystallites," Journal of Physical Chemistry B **101**, 9463-9475 (1997).
28. S. Kudera, L. Maus, M. Zanella, and W. Parak, "Core-Shell Nanocrystals," in *Comprehensive Nanoscience and Technology*, D. L. Andrews, G. D. Scholes, and G. P. Wiederrecht, eds. (2011), p. 271.
29. S. Kim, B. Fisher, H.-J. Eisler, and M. Bawendi, "Type-II quantum dots: CdTe/CdSe

(core/shell) and CdSe/ZnTe (core/shell) heterostructures," Journal of the American Chemical Society **125**, 11466-11467 (2003).
30. H. Zhong, T. Mirkovic, and G. D. Scholes, "Nanocrystal Synthesis," in *Comprehensive Nanoscience and Technology*, D. L. Andrews, G. D. Scholes, and G. P. Wiederrecht, eds. (2011), p. 153.
31. D. J. Milliron, S. M. Hughes, Y. Cui, L. Manna, J. Li, L.-W. Wang, and A. P. Alivisatos, "Colloidal nanocrystal heterostructures with linear and branched topology," Nature **430**, 190-195 (2004).
32. R. Cammarata, "Mechanical properties of nanocomposite thin films," Thin Solid Films **240**, 82-87 (1994).
33. S. Chakrabarti, D. Das, D. Ganguli, and S. Chaudhuri, "Tailoring of room temperature excitonic luminescence in sol–gel zinc oxide–silica nanocomposite films," Thin Solid Films **441**, 228-237 (2003).
34. H. Katz, G. Scheller, T. Putvinski, M. Schilling, W. Wilson, and C. Chidsey, "Polar orientation of dyes in robust multilayers by zirconium phosphate-phosphonate interlayers," Science **254**, 1485-1487 (1991).
35. Y. Hamanaka, A. Nakamura, S. Omi, N. Del Fatti, F. Vallée, and C. Flytzanis, "Ultrafast response of nonlinear refractive index of silver nanocrystals embedded in glass," Applied Physics Letters **75**, 1712 (1999).
36. S. Mandal, R. Roy, and A. Pal, "Effect of particle shape distribution on the surface plasmon resonance of Ag–SiO_2 nanocomposite thin films," Journal of Physics D: Applied Physics **36**, 261 (2003).
37. U. Kreibig, and L. Genzel, "Optical absorption of small metallic particles," Surface Science **156**, 678-700 (1985).
38. V. Musat, E. Fortunato, S. Petrescu, and A. Botelho do Rego, "ZnO/SiO_2 nanocomposite thin films by sol–gel method," physica status solidi (a) **205**, 2075-2079 (2008).
39. Y.-Y. Peng, T.-E. Hsieh, and C.-H. Hsu, "White-light emitting ZnO–SiO_2 nanocomposite thin films prepared by the target-attached sputtering method," Nanotechnology **17**, 174 (2006).
40. L. Guo, S. Yang, C. Yang, P. Yu, J. Wang, W. Ge, and G. K. Wong, "Highly monodisperse polymer-capped ZnO nanoparticles: Preparation and optical properties," Applied Physics Letters **76**, 2901-2903 (2000).
41. U. Schürmann, W. Hartung, H. Takele, V. Zaporojtchenko, and F. Faupel, "Controlled syntheses of Ag–polytetrafluoroethylene nanocomposite thin films by co-sputtering from two magnetron sources," Nanotechnology **16**, 1078 (2005).
42. J. L. H. Chau, Y.-M. Lin, A.-K. Li, W.-F. Su, K.-S. Chang, S. L.-C. Hsu, and T.-L. Li, "Transparent high refractive index nanocomposite thin films," Materials Letters **61**, 2908-2910 (2007).

43. T. Kyprianidou-Leodidou, W. Caseri, and U. W. Suter, "Size variation of PbS particles in high-refractive-index nanocomposites," The Journal of Physical Chemistry **98**, 8992-8997 (1994).
44. L. Zimmermann, M. Weibel, W. Caseri, and U. W. Suter, "High refractive index films of polymer nanocomposites," Journal of Materials Research **8**, 1742-1748 (1993).
45. D. A. Steigerwald, J. C. Bhat, D. Collins, R. M. Fletcher, M. O. Holcomb, M. J. Ludowise, P. S. Martin, and S. L. Rudaz, "Illumination with solid state lighting technology," Selected Topics in Quantum Electronics, IEEE Journal of **8**, 310-320 (2002).
46. A. H. Yuwono, B. Liu, J. Xue, J. Wang, H. I. Elim, W. Ji, Y. Li, and T. J. White, "Controlling the crystallinity and nonlinear optical properties of transparent TiO_2-PMMA nanohybrids," Journal of Materials Chemistry **14**, 2978 (2004).
47. K.-F. Lin, H.-M. Cheng, H.-C. Hsu, L.-J. Lin, and W.-F. Hsieh, "Band gap variation of size-controlled ZnO quantum dots synthesized by sol–gel method," Chemical Physics Letters **409**, 208-211 (2005).
48. Stephen Y. Chou, P. R. Krauss, and P. J. Renstrom, "Nanoimprint lithography," Journal of Vacuum Science and Technology B **14**, 4129-4133 (1996).
49. H. Lan, and Y. Ding, *Nanoimprint lithography* (INTECH, Croatia, 2010).
50. P. B. Fischer, and S. Y. Chou, "10 nm electron beam lithography and sub-50 nm overlay using a modified scanning electron microscope," Applied Physics Letters **62**, 2989-2991 (1993).
51. Stephen Y. Chou, P. R. Krauss, and P. J. Renstrom, "Imprint of sub-25 nm vias and trenches in polymers," Applied Physics Letters **67**, 3114-3116 (1995).
52. K. Early, M. L. Schattenburg, and H. I. Smith, "Absence of resolution degradation in X-ray lithography for x from 4.5nm to 0.83nm," Microelectronic Engineering **11**, 317-321 (1990).
53. J. D. Hoff, L.-J. Cheng, E. Meyhofer, L. J. Guo, and A. J. Hunt, "Nanoscale Protein Patterning by Imprint Lithography," Nano letters **4**, 853-857 (2004).
54. L. J. Guo, "Nanoimprint Lithography: Methods and Material Requirements," Advanced Materials **19**, 495-513 (2007).
55. Y. Hirai, T. Yoshikawa, N. Takagi, and S. Yoshida, "Mechanical properties of Poly-methyl methacrylate (PMMA) for nanoimprint lithography," Journal of Photopolymer Science and Technology **16**, 615-620 (2003).
56. C. Martin, L. Ressier, and J. P. Peyrade, "Study of PMMA recoveries on micrometric patterns replicated by nano-imprint lithography," Physica E: Low-dimensional Systems and Nanostructures **17**, 523-525 (2003).
57. J. Haisma, M. Verheijen, K. Van Den Heuvel, and J. Van Den Berg, "Mold-assisted nanolithography: A process for reliable pattern replication," Journal of Vacuum Science & Technology B: Microelectronics and Nanometer Structures **14**, 4124-4128 (1996).

58. M. Vogler, S. Wiedenberg, M. Mühlberger, I. Bergmair, T. Glinsner, H. Schmidt, E.-B. Kley, and G. Grützner, "Development of a novel, low-viscosity UV-curable polymer system for UV-nanoimprint lithography," Microelectronic engineering **84**, 984-988 (2007).
59. M. Bender, M. Otto, B. Hadam, B. Spangenberg, and H. Kurz, "Multiple imprinting in UV-based nanoimprint lithography: related material issues," Microelectronic engineering **61**, 407-413 (2002).
60. M. Bender, A. Fuchs, U. Plachetka, and H. Kurz, "Status and prospects of UV-nanoimprint technology," Microelectronic Engineering **83**, 827-830 (2006).
61. W. M. Choi, and O. O. Park, "A soft-imprint technique for direct fabrication of submicron scale patterns using a surface-modified PDMS mold," Microelectronic Engineering **70**, 131-136 (2003).
62. E. Roy, Y. Kanamori, M. Belotti, and Y. Chen, "Enhanced UV imprint ability with a tri-layer stamp configuration," Microelectronic Engineering **78-79**, 689-694 (2005).
63. J. Tong, C. A. Simmons, and Y. Sun, "Precision patterning of PDMS membranes and applications," Journal of Micromechanics and Microengineering **18**, 037004 (2008).
64. N. Koo, M. Bender, U. Plachetka, A. Fuchs, T. Wahlbrink, J. Bolten, and H. Kurz, "Improved mold fabrication for the definition of high quality nanopatterns by Soft UV-Nanoimprint lithography using diluted PDMS material," Microelectronic Engineering **84**, 904-908 (2007).
65. B. D. Gates, "Nanofabrication with molds & stamps," Materials Today **8**, 44-49 (2005).
66. S. L. Hellstrom, "Basic models of spin coating," (Submitted as coursework for Physics 210, Stanford University, 2007).
67. J. H. Burroughes, D. D. C. Bradley, A. E. Brown, R. N. Marks, K. Mackay, R. H. Friend, P. L. Burns, and A. B. Holmes, "Light-emitting diodes based on conjugated polymers," Nature **347**, 539-541 (1990).
68. A. Mihi, M. Ocaña, and H. Míguez, "Oriented Colloidal-Crystal Thin Films by Spin-Coating Microspheres Dispersed in Volatile Media," Advanced Materials **18**, 2244-2249 (2006).
69. J. H. Lai, "An investigation of spin coating of electron resists," Polymer Engineering and Science **19**, 1117-1121 (1979).
70. B. Chen, "Investigation of the solvent-evaporation effect on spin coating of thin films," Polymer Engineering and Science **23**, 399-403 (1983).
71. W. Daughton, and F. Givens, "An Investigation of the Thickness Variation of Spun-on Thin Films Commonly Associated with the Semiconductor Industry," Journal of The Electrochemical Society **129**, 173-179 (1982).
72. S. Dhoble, H. Swart, and K. Park, *Phosphate Phosphors for Solid-state Lighting* (Springer, 2012).
73. R. S. Meltzer, and S. P. Feofilov, "Spectral hole burning in the 4f–5d transition of $Ce3^{+}$ in

$LuPO_4$ and YPO_4," Journal of Luminescence **102–103**, 151-155 (2003).
74. G. Blasse, and B. Grabmaier, *Luminescent materials* (Springer-Verlag Berlin, 1994).
75. A. Forouhi, and I. Bloomer, "Optical dispersion relations for amorphous semiconductors and amorphous dielectrics," Physical Review B **34**, 7018 (1986).
76. S. Bosch, J. Ferré-Borrull, N. Leinfellner, and A. Canillas, "Effective dielectric function of mixtures of three or more materials: a numerical procedure for computations," Surface science **453**, 9-17 (2000).
77. D. B. Williams, and C. B. Carter, *The Transmission Electron Microscope* (Springer, 1996).
78. B. Fultz, and J. M. Howe, *Transmission electron microscopy and diffractometry of materials* (Springer, 2012).
79. Z. Wang, "Transmission electron microscopy of shape-controlled nanocrystals and their assemblies," The Journal of Physical Chemistry B **104**, 1153-1175 (2000).
80. M. A. Hayat, *Principles and techniques of scanning electron microscopy. Biological applications. Volume 1* (Van Nostrand Reinhold Company., 1974).
81. J. Goldstein, D. E. Newbury, D. C. Joy, C. E. Lyman, P. Echlin, E. Lifshin, L. Sawyer, and J. R. Michael, *Scanning electron microscopy and X-ray microanalysis* (Springer, 2003).
82. G. Binnig, C. F. Quate, and C. Gerber, "Atomic force microscope," Physical review letters **56**, 930 (1986).
83. N. C. Santos, and M. A. Castanho, "An overview of the biophysical applications of atomic force microscopy," Biophysical chemistry **107**, 133-149 (2004).
84. K. Khulbe, and T. Matsuura, "Characterization of synthetic membranes by Raman spectroscopy, electron spin resonance, and atomic force microscopy; a review," Polymer **41**, 1917-1935 (2000).
85. T. Gumı, M. Valiente, K. Khulbe, C. Palet, and T. Matsuura, "Characterization of activated composite membranes by solute transport, contact angle measurement, AFM and ESR," Journal of membrane science **212**, 123-134 (2003).
86. M. Vilaseca, E. Mateo, L. Palacio, P. Prádanos, A. Hernández, A. Paniagua, J. n. Coronas, and J. Santamaría, "AFM characterization of the growth of MFI-type zeolite films on alumina substrates," Microporous and mesoporous materials **71**, 33-37 (2004).
87. C. Iliescu, J. Jing, F. E. Tay, J. Miao, and T. Sun, "Characterization of masking layers for deep wet etching of glass in an improved HF/HCl solution," Surface and Coatings Technology **198**, 314-318 (2005).
88. K. Boussu, B. Van der Bruggen, A. Volodin, J. Snauwaert, C. Van Haesendonck, and C. Vandecasteele, "Roughness and hydrophobicity studies of nanofiltration membranes using different modes of AFM," Journal of colloid and interface science **286**, 632-638 (2005).
89. R. Loef, A. J. Houtepen, E. Talgorn, J. Schoonman, and A. Goossens, "Study of electronic defects in CdSe quantum dots and their involvement in quantum dot solar cells,"

Nano letters **9**, 856-859 (2009).
90. K. L. Knappenberger, D. B. Wong, Y. E. Romanyuk, and S. R. Leone, "Excitation wavelength dependence of fluorescence intermittency in CdSe/ZnS core/shell quantum dots," Nano letters **7**, 3869-3874 (2007).
91. W. G. van Sark, P. L. Frederix, D. J. Van den Heuvel, H. C. Gerritsen, A. A. Bol, J. N. van Lingen, C. de Mello Donega, and A. Meijerink, "Photooxidation and photobleaching of single CdSe/ZnS quantum dots probed by room-temperature time-resolved spectroscopy," The Journal of Physical Chemistry B **105**, 8281-8284 (2001).
92. M. W. Rowell, M. A. Topinka, M. D. McGehee, H.-J. Prall, G. Dennler, N. S. Sariciftci, L. Hu, and G. Gruner, "Organic solar cells with carbon nanotube network electrodes," Applied Physics Letters **88**, 233506 (2006).
93. M. Karlík, "Lattice imaging in transmission electron microscopy," Materials Structure **8**, 3 (2001).
94. D. I. Son, C. H. You, J. H. Jung, and T. W. Kim, "Carrier transport mechanisms of organic bistable devices fabricated utilizing colloidal ZnO quantum dot-polymethylmethacrylate polymer nanocomposites," Applied Physics Letters **97**, 013304 (2010).
95. Z.-H. Chen, S. Hellström, Z.-J. Ning, Z.-Y. Yu, and Y. Fu, "Exciton polariton contribution to the stokes shift in colloidal quantum dots," The Journal of Physical Chemistry C **115**, 5286-5293 (2011).
96. M. Hong, M. Guo-Hong, W. Wen-Jun, G. Xue-Xi, and M. Hong-Liang, "Size-dependent optical properties and carriers dynamics in CdSe/ZnS quantum dots," Chinese Physics B **17**, 1280 (2008).
97. M. Hopmeier, W. Guss, M. Deussen, E. Göbel, and R. Mahrt, "Enhanced dipole-dipole interaction in a polymer microcavity," Physical review letters **82**, 4118 (1999).
98. H. Mattoussi, J. Heine, M. Kuno, J. Michel, M. Bawendi, and K. Jensen, "Evidence of photo-and electrodarkening of (CdSe) ZnS quantum dot composites," Journal of Applied Physics **87**, 8526-8534 (2000).
99. N. Korsunska, M. Dybiec, L. Zhukov, S. Ostapenko, and T. Zhukov, "Reversible and non-reversible photo-enhanced luminescence in CdSe/ZnS quantum dots," Semiconductor science and technology **20**, 876-881 (2005).
100. Y. Zhao, C. Riemersma, F. Pietra, R. Koole, C. de Mello Donegá, and A. Meijerink, "High-temperature luminescence quenching of colloidal quantum dots," ACS nano **6**, 9058-9067 (2012).
101. D. Valerini, A. Creti, M. Lomascolo, L. Manna, R. Cingolani, and M. Anni, "Temperature dependence of the photoluminescence properties of colloidal CdSe / ZnS core/shell quantum dots embedded in a polystyrene matrix," Physical Review B **71**, 235409 (2005).

102. B. Richards, "Enhancing the performance of silicon solar cells via the application of passive luminescence conversion layers," Solar energy materials and solar cells **90**, 2329-2337 (2006).
103. Z. Cheng, F. Su, L. Pan, M. Cao, and Z. Sun, "CdS quantum dot-embedded silica film as luminescent down-shifting layer for crystalline Si solar cells," Journal of Alloys and Compounds **494**, L7-L10 (2010).
104. B. M. van der Ende, L. Aarts, and A. Meijerink, "Lanthanide ions as spectral converters for solar cells," Physical Chemistry Chemical Physics **11**, 11081-11095 (2009).
105. S. V. Gaponenko, *Optical properties of semiconductor nanocrystals* (Cambridge university press, 1998).
106. M. S. Park, Y. Lee, and J. K. Kim, "One-step preparation of antireflection film by spin-coating of polymer/solvent/nonsolvent ternary system," Chemistry of materials **17**, 3944-3950 (2005).
107. D. O. Demchenko, and L.-W. Wang, "Optical transitions and nature of Stokes shift in spherical CdS quantum dots," Physical Review B **73**, 155326 (2006).
108. M. Nirmal, D. Norris, M. Kuno, M. Bawendi, A. L. Efros, and M. Rosen, "Observation of the" dark exciton" in CdSe quantum dots," Physical review letters **75**, 3728-3731 (1995).
109. A. J. Nozik, "Multiple exciton generation in semiconductor quantum dots," Chemical Physics Letters **457**, 3-11 (2008).
110. S. Vedraine, P. Torchio, D. Duché, F. Flory, J.-J. Simon, J. Le Rouzo, and L. Escoubas, "Intrinsic absorption of plasmonic structures for organic solar cells," Solar energy materials and solar cells **95**, S57-S64 (2011).
111. H. Hoppe, and N. S. Sariciftci, "Organic solar cells: An overview," Journal of Materials Research **19**, 1924-1945 (2004).
112. A. Tavlove, and S. C. Hagness, "Computational electrodynamics: the finite-difference time-domain method," Artech House, Norwood, MA **2062** (1995).
113. D. Duche, P. Torchio, L. Escoubas, F. Monestier, J.-J. Simon, F. Flory, and G. Mathian, "Improving light absorption in organic solar cells by plasmonic contribution," Solar Energy Materials and Solar Cells **93**, 1377-1382 (2009).
114. Y. A. Akimov, W. Koh, S. Sian, and S. Ren, "Nanoparticle-enhanced thin film solar cells: Metallic or dielectric nanoparticles?," Applied Physics Letters **96**, 073111 (2010).
115. W. W. Yu, and X. Peng, "Formation of High - Quality CdS and Other II–VI Semiconductor Nanocrystals in Noncoordinating Solvents: Tunable Reactivity of Monomers," Angewandte Chemie International Edition **41**, 2368-2371 (2002).
116. C. Leatherdale, W.-K. Woo, F. Mikulec, and M. Bawendi, "On the absorption cross section of CdSe nanocrystal quantum dots," The Journal of Physical Chemistry B **106**, 7619-7622 (2002).
117. F. Intonti, S. Vignolini, F. Riboli, A. Vinattieri, D. Wiersma, M. Colocci, M. Gurioli, L.

Balet, C. Monat, and L. Li, "Near-field mapping of quantum dot emission from single-photonic crystal cavity modes," Physica E: Low-dimensional Systems and Nanostructures **40**, 1965-1967 (2008).
118. C. Schneider, T. Heindel, A. Huggenberger, P. Weinmann, C. Kistner, M. Kamp, S. Reitzenstein, S. Höfling, and A. Forchel, "Single photon emission from a site-controlled quantum dot-micropillar cavity system," Applied Physics Letters **94**, 111111 (2009).
119. Guangming Wang, Zuhong Lu, Chunwei Yuan, and Y. Wei, "Influence of the surface pressure of Langmuir-Blodgett films on the efficiency of organic electroluminescence," Thin Solid Films **288**, 334-336 (1996).
120. V. Nandwana, C. Subramani, Y.-C. Yeh, B. Yang, S. Dickert, M. D. Barnes, M. T. Tuominen, and V. M. Rotello, "Direct patterning of quantum dot nanostructures via electron beam lithography," Journal of Materials Chemistry **21**, 16859 (2011).
121. G. Wang, Z. Lu, C. Yuan, and Y. Wei, "Influence of the surface pressure of Langmuir-Blodgett films on the efficiency of organic electroluminescence," Thin solid films **288**, 334-336 (1996).
122. S. Shum, and K. Luk, "An efficient FDTD near-to-far-field transformation for radiation pattern calculation," Microwave and optical technology letters **20**, 129-131 (1999).
123. A. Taflove, and K. Umashankar, "Radar cross section of general three-dimensional scatterers," IEEE Transactions on Electromagnetic Compatibility **EMC-25**, 433-440 (1983).
124. R. J. Luebbers, K. S. Kunz, M. Schneider, and F. Hunsberger, "A finite-difference time-domain near zone to far zone transformation [electromagnetic scattering]," IEEE Transactions on Antennas and Propagation **39**, 429-433 (1991).